Screening, Coulomb Interactions, and Plasmonic Phenomena on the Nanoscale

BY

Min Seok Choi
B.S., University of Colorado at Boulder, 2010

Thesis submitted as partial fulfillment of the requirements
for the degree of Doctor of Philosophy in Electrical and Computer Engineering
in the Graduate College of the
University of Illinois at Chicago, 2016

Chicago, Illinois

Defense Committee:

Michael A. Stroscio, Chair and Advisor
Mitra Dutta
Junxia (Lucy) Shi
Zheng Yang
Jordi Cabana, Chemistry

To my parents,

Mrs. Seung Ho Park and Mr. Jun Seob Choi

ACKNOWLEDGMENTS

First, I would like to thank Dr. Michael A. Stroscio for his enormous support, unfailing guidance, and mentorship through the whole course of my Ph. D. Study, for his patience and motivation, and for providing me with all the necessary facilities for the research. His knowledge and wisdom was the key to my accomplishment in many ways.

I would also like to thank my colleagues, the professors and the staffs at UIC, and everyone in Nanoengineering Research Group. I sincerely appreciate all the support from Dr. Mitra Dutta for her knowledge and helpful advice; Dr. Seyoung An at Nanotechnology Core Facility at UIC for his help with the clean room equipments and great advice both for my research and for my life; Dr. Tad Daniel and Dr. Alan Nicholls for their help with TEM; Dr. Paul Malchow for his guidance and advice with electro-physiology research; Tina Alvarado, Evelyn Reyes, Ala Wroblewski, Mona Hurt, Mihai Bora, and Erica Plys for administration help and correcting my mistakes. I also would like to extend my gratitude to my dissertation committee members, Dr. Lucy Shi, Dr. Zheng Yang, and Dr. Jordi Cabana for valuable discussions and suggestions for completing my thesis.

My sincere appreciation also goes to to the members in our research group, Dr. Xenia Meshik, Dr. Sidra Farid, Souvik Mukherjee, Dr. Yi Lan, Debopam Datta, Ketaki Sarkar, Dr. Shripriya Poduri, Dr. Nanzhu Zhang, for their help and friendship. Especially, Dr. Meshik was another key to successful completion of my research.

ACKNOWLEDGMENTS (Continued)

Finally, I would like to show my sincerest appreciation to my parents, my sister, Yujin Choi, and my fiancé, Hee Jin Kim. I would not be able to complete my research without their enormous support at all time in all way.

MSC

TABLE OF CONTENTS

TABLE OF CONTENTS (Continued)

CHAPTER **PAGE**

LIST OF TABLES

LIST OF FIGURES

LIST OF FIGURES (Continued)

FIGURE **PAGE**

LIST OF FIGURES (Continued)

FIGURE **PAGE**

LIST OF ABBREVIATIONS

1D	One Dimensional
3D	Three Dimensional
AFM	Atomic Force Microscope
CPU	Central Processing Unit
DNA	Deoxyribonucleic Acid
EFM	Electrostatic Force Microscope
FDTD	Finite Difference Time Domain
FET	Field Effect Transistor
FP-LAPW	Full Potential - Linearized Augmented Plane Wave
GULP	General Utility Lattice Program
HEM	Hybrid Electromagnetic
LBL	Layer-by-layer
LDA	Local Density Approximation
LDOS	Local Density of State
NW	Nanowire
PDDA	Poly(diallyldimethlammonium chloride)
PL	Photoluminescence

LIST OF ABBREVIATIONS (Continued)

RPA	Random Phase Approximation
SCS	Scattering Cross Section
SPP	Surface Plasmon Polaritons
TDDFT	Time Dependent Density Functional Theory
TE	Transverse Electric
TEM	Transmission Electron Microscope
TEOS	Tetraethylorthosilicate
TM	Transverse Magnetic
QD	Quantum Dot
UIC	University of Illinois at Chicago

SUMMARY

Nanostructures such as quantum dots, nanowires, nanodisks, etc. are studied using both experimental and theoretical approaches in several areas of the field. To reduce the confusion from the diverse fields of study, this manuscript is divided intof three main parts. The first part is a review of background and related theory is presented in luminescence phenomena and Coulomb interaction in plasmonic nanostructures (Luminescent and Ionic property) and effect of nanostructure on ion current through membrane (Electrolyte property). In the second part, related previous works are discussed. Finally, the manuscript is concluded with the discussion of future research.

The main goal of this dissertation is to demonstrate how various phenomena influence on properties of nanostructures and how to apply them. In order to achieve the goal, the remainder of this manuscript is organized as follows. Chapter 1 introduces the phenomina of interest and overviews the current research in the field that motivates the proposed dissertation. In Chapter 2, theoretical studies of enhancing luminescence from silicon NWs are presented. Chapter 3 illustrates numerical calculations of the scattering cross section of plasmonic nanodisks. Methods of synthesis and characterization of ZnO quantum dots, and the controlling the ionic currents by modifying membrane potential on ion channels with nanostructures are presented in Chapter 4 and 5, respectively. Future works and the conclusion are presented in Chapter 5.

CHAPTER 1

INTRODUCTION

Since Richard Feynman introduced the concept of "small scale"in his famous lecture, "Plenty of room at the bottom", in 1959, nanotechnology has been advanced dramatically. With the development of nanotechnology, it has been providing us enormous benefits in research from everyday consumer products to biomedical applications to sophisticated research equipments. What makes nanotechnology unique is the underlying phenomena that do not appear in the macroscopic world. As time passes, it has become possible to understand why the unique occurrences happen in nanoscale better with the development of theories such as quantum mechanics and computer simulations. However, as Stephen Hawking said in his lecture in 1999, which stated "Einstein was doubly wrong when he said, God does not play dice"[1], it is extremely difficult, if not impossible, to fully understand what is going on in the nanoscale, because a lot of phenomena are occurring simultaneously and some of them are based on probabilities. So, it is important to perceive dominant microscopic phenomena (i.e. the most probable phenomena) to predict how nanostructures would behave in certain situations.

---

[1]Despite Einstein admitted quantum mechanics is a successful theory, he believed there would be a missing factor in the theory. He was opposed to its probabilistic aspect saying "God does not play dice with the universe. "

1.1 Motivation

1.1.1 Luminescent and Ionic Property

Silicon is the second most abundant material in the earth's crust by mass. [2] It is relatively easier to manufacture an extremely pure single crystalline silicon and to grow high quality oxide, SiO_2, by just oxidizing the silicon surface which would form a relatively good interface compared to other combinations of a semiconductor and an oxide layer. As a result, Si-SiO_2 structure became a basis of the current semiconductor manufacturing process. The basis structures are mostly connected by copper to make integrated circuits. However, despite copper is a good conductor, there is a restriction in the electrical communication through the fact that the material due to the resistivity. Also, as the total length of the metal interconnects increases due to the increase of the number of transistors in a single chip, the power consumption level and the heat dissipation starts to be problematic. [3] So, it would be better if it can be replaced by low power consuming, low resistant method, while copper is a desired material to use for contacts and short interconnects and should not be replaced. The optimal candidate is light, which is very fast with low power consumption level. Since the current manufacturing process is optimized to silicon process, it would be cost efficient, convenient, reducing possible problems, if silicon can produce light. Unfortunately, although the electronic and mechanical properties of silicon are great, it is very hard to generate lights from due to the fact that silicon is an indirect band gap material. Agarwal has observed visible hot lunimescence with relatively high efficiency in bulk silicon with a silver nanocavity and 5 nm thick silicon dioxide (SiO_2) interlayer, of which the internal quantum efficiency is very low by silicon itself. [4] In Chapter

2, a proposed mechanism a plasmon-assisted nonlocal absorption and phonon-assisted second-order absorption process will be presented.

1.1.2 Ion Channel

Ion channels are important transmembrane proteins that modulate the flow of ions in and out of cells. With advancement in patch-clamp techniques, it became possible to accurately track down the behavior of ion channel proteins inserted in a part of lipid bilayer immersed in electrolyte. There are different ways of modulating ion channels; voltage gating (e.g. K^+ and Na^+ channels), ligand gating (e.g. Nicotinic acetylcholine receptor), mechanical gating (e.g. Mechano-sensitive channels), pH gating (e.g. Acid-sensing ion channel), etc. In chapter 4, voltage-gated ion channels will be studied with the patch-clamp under influence of an external electric field produced by polarized quantum dots (QDs). Because the ion channels are modulated with the membrane potential, it is expected that the external electric field affects the behavior of the ion current in and out of a neuronal cell. Furthermore, theoretical modeling are to confirm experimentally observed trends. While a number of studies has been done to characterize individual voltage-gated conductances in horizontal cells, theoretical descriptions of ion channel behavior in these cells is limited. Such a theoretical description could help reveal fundamental characteristics of ion channel behavior, especially under circumstances where such channel activity could be modulated by the influence of QDs. Also in Chapter 4, an electrical model of a horizontal cell in the absence and presence of a QD is proposed based on our experimental data. Both experimental results and theoretical modeling show that UV-induced electric fields of TiO_2 QDs can influence the activation of voltage-gated ion channels as long as

the QDs are in close proximity to ion channels. Finally in Chapter 5, a synthesis and characterization methods of permanent electric field producing QDs, ZnO, are presented that can be used as a permanent modifier of ion currents.

CHAPTER 2

PLASMONICALLY ENHANCED LUMINESCENCE FROM SILICON NANOWIRES

Under normal circumstances, it is very difficult for silicon to absorb a photon with energy less than 4.2 eV. It is due to the unique electronic dispersion relation of silicon, which has the minimum of the conduction band is located far from the maximum of the valence band in terms of momentum. [5] In order for an electron in the valence band of silicon to get excited to the conduction band, it requires either high energy (more than 4.2 eV) or energy higher than indirect band gap (1.12 ev) plus a source of momentum to satisfy both the momentum and energy conservation rule. The mismatch in momentum space of the maximum of the valence band and the minimum of the conduction band is referred as non-locality of the electronic band structure. In the present chapter, nonlocal optical absorption mechanisms will be proposed for indirect bandgap silicon in nanoscale assisted by surface plasmon polaritons. (SPP)

SPP in a thin metal film have been studied extensively in recent years due to their unique properties such as a huge increase of intensity [6], non-locality [7], etc. Recently, Trolle et al. [8] suggested a mechanism of optical excitation in silicon with photon energy below the direct bandgap using the non-locality of SPP in a silver thin film embedded in crystalline silicon. With a quantum mechanical point of view, this can be explained by the uncertainty principle,

---

[0]Parts of this thesis were reproduced with permission from ©2015 IEEE

which asserts a wider spread of uncertainty in momentum space with high confinement in spatial space. In this chapter, we examine the nonlocal optical absorption in a silicon nanowire coupled with silver nanocavity.

Another possible process is the second order transition involving phonons to conserve the momentum as well as the energy. That is, an electron in the valence band absorbs its energy and momentum from a photon and several phonons to get excited to the conduction band. However, the second order process requires large number of phonons, where phonons and electrons are in unexcited system. A laser pulse rarely generates optical phonons in non-polar silicon.

A proposed machanism that generates a large number of coherent phonons which eventually makes efficient light emission from bulk silicon possible will be also demonstrated in the present chapter. Number of coherent phonons produced in the second order process can be estimated by the theory of stimulated Raman scattering.

The motivation of this study is the work done by Agarwal [4]. Cho et. al. found that a silicon nanowire that has a diameter of 70 nm with 5 nm thick natural SiO_2 on the surface which has been covered by 150 μm silver, one of the best plasmonic materials, can produce hot luminescence. Figure 1 shows the schematic diagram of the device. Throughout the chapter, the proposed theories will be based on the device. The goal of the present chapter is to propose a theory to explain the phenomena of the device.

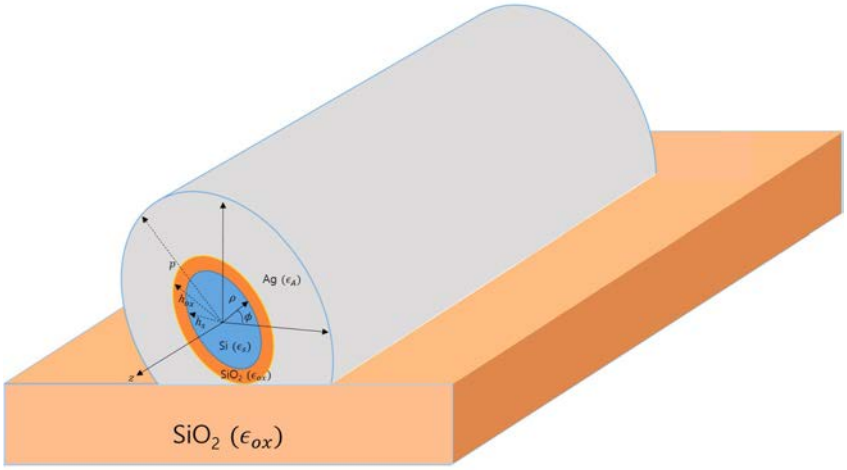

(a) Schematic drawing of the device.

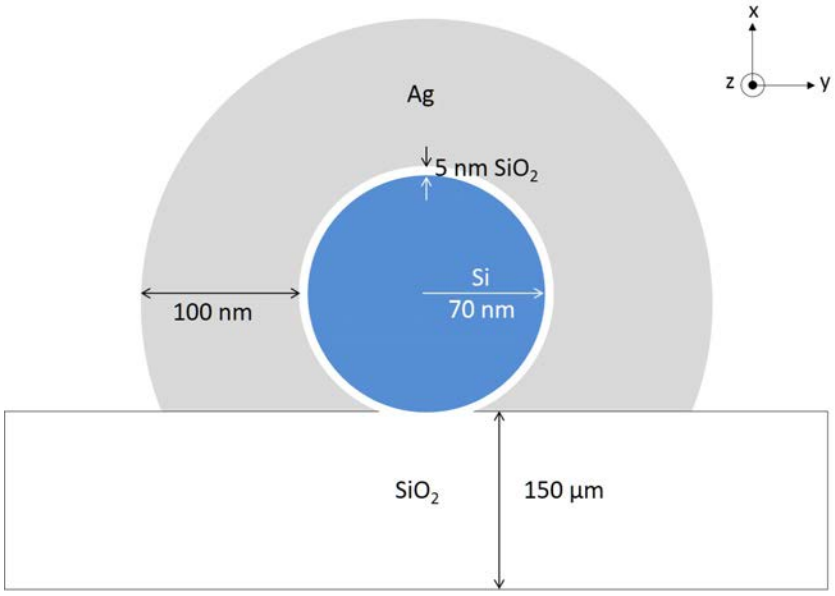

(b) Schematic tomography of the device.

Figure 1: Schematics of the (a) whole structure and (b) tomography of the device.

2.1 Plasmonic Absorption Process

2.1.1 Plasmons

A plasmon is referred as a collective movement of electrons in a material with abundant free electrons such as metals. The collection of electrons with minus charges are oscillating relative to the nucleus with plus charges, acting like an oscillating localized dipole, thus produce an electric field. This phenomena can easily occur at the surface of the metal with an assist from triggering energy source such as photons. A photon can invoke the surface plasmon and couple with them, and this is called surface plasmon polaritons or SPP. [7] SPP can be described both quantum mechanically as a particle and classically as an evanescent wave and obey the Maxwell's equations. [7, 9]

2.1.2 Drude-Lorentz model

For the classical treatment of plasmons, it is important to construct an appropriate dielectric function to describe both the optical and plasmonic behavior of metal. One of the most distinct characteristics of metals from another dielectric materials is the optical response in visible range; metals shine. The high reflectivity of light is due to the abundance of free electrons in metals. The collective movement of these free electrons, *plasmons*, responding to eletromagnetic fields, can be fully described by the dielectric function. [7] Since the free electrons play a role as significant as bound electrons, the dielectric function of metals can be described mathematically by

$$\tilde{\epsilon}(\omega) = \tilde{\epsilon}^{(free)}(\omega) + \tilde{\epsilon}^{(bound)}(\omega), \tag{2.1}$$

where $\tilde{\epsilon}^{(free)}(\omega)$ is the free electron contribution to the dielectric function and $\tilde{\epsilon}^{(bound)}(\omega)$ is the bound-electron contribution. The free electron contribution can be described by Drude model: [1]

$$\tilde{\epsilon}^{(free)}(\omega) = 1 - \frac{f_0\omega_p^2}{\omega(\omega - i\Gamma_f)}, \tag{2.2}$$

where $f_0 = m/m* \equiv$ oscillator strength, $\omega_p \equiv$ plasma frequency, and $\Gamma_f \equiv$ damping constant of free electron part. Since the bound-electron contribution is being considered separately from the free electron part, it can be described by the Lorentz model, which is the sum of n interband transition effect on the dielectric function:

$$\tilde{\epsilon}^{(bound)}(\omega) = -\sum_{j=1}^{n} \frac{f_j\omega_p^2}{\omega^2 - \omega_j^2 + i\Gamma_{b,j}}. \tag{2.3}$$

Now, Equation 2.1 becomes:

$$\tilde{\epsilon}(\omega) = 1 - \frac{f_0\omega_p^2}{\omega(\omega - i\Gamma_f)} - \sum_{j=1}^{n} \frac{f_j\omega_p^2}{\omega^2 - \omega_j^2 + i\Gamma_{b,j}}, \tag{2.4}$$

which is referred as Lorentz-Drude model. The parameters of Ag, Al, Ni, and Cu used in this work are summarized in Table I, and are plotted in Figure 2.

2.1.3 Wavevector- and Frequency-dependent Dielectric Function of Silicon

In order to analyze the optical interaction of plasmonics metals and silicon accurately in classical regime, the dielectric function of silicon should be calculated with accuracy. More

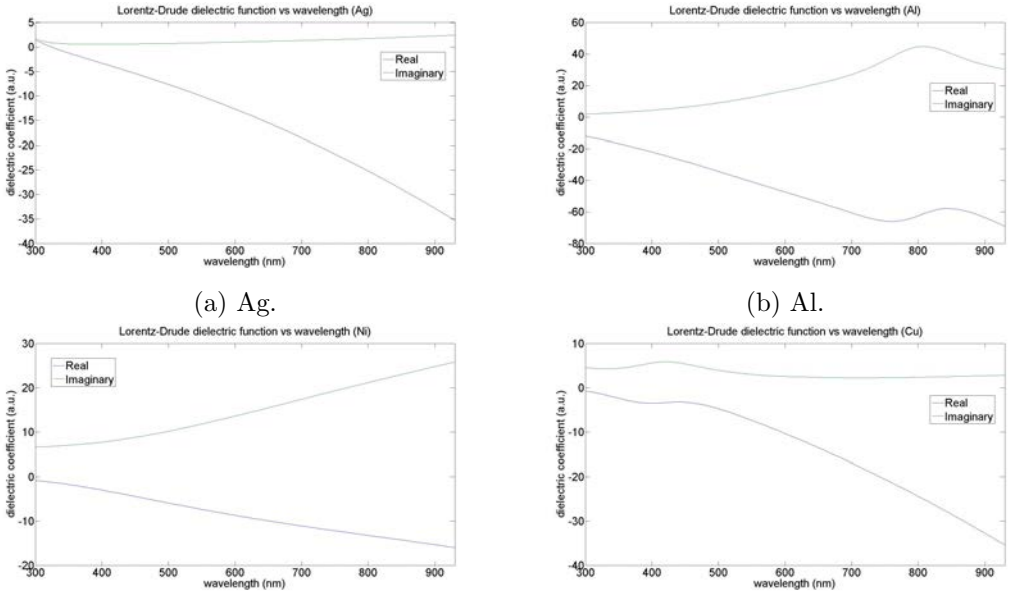

(a) Ag. (b) Al.

(c) Ni. (d) Cu.

Figure 2: Dielectric functions as a function of angular frequency of (a) Ag, (b) Al, (c) Ni, and (d) Cu.

Metal	$\omega_p(eV)$	f_0[a]	$\Gamma_0(eV)$	f_1	Γ_1 (eV)	ω_1 (eV)	f_2	Γ_2 (eV)	ω_2 (eV)
Ag	9.01	0.845	0.048	0.065	3.886	0.816	0.124	0.452	4.481
Al	14.98	0.523	0.048	0.227	0.333	0.162	0.050	0.312	1.544
Ni	15.92	0.096	0.048	0.100	4.511	0.174	0.135	1.334	0.582
Cu	10.83	0.575	0.030	0.061	0.378	0.291	0.104	1.056	2.957
Metal	f_3	Γ_3 (eV)	ω_3 (eV)	f_4	Γ_4 (eV)	ω_4 (eV)	f_5	Γ_5 (eV)	ω_5 (eV)
Ag	0.011	0.065	8.175	0.840	0.916	9.083	5.646	2.419	20.29
Al	0.166	1.351	1.808	0.030	3.382	3.473	-	-	-
Ni	0.106	2.178	1.597	0.729	6.292	6.089	-	-	-
Cu	0.723	3.213	5.300	0.638	4.305	11.18	-	-	-

[a]adimensional.

TABLE I: LORENTZ-DRUDE MODEL PARAMETERS OF SILVER, ALUMINUM, NICKEL, AND COPPER. [1] ©2015 IEEE

importantly, it is necessary to obtain the wavevector- and frequency-dependent dielectric function of silicon to consider the interaction of momentum carrying carriers like SPP. One way to obtain such function is to use quantum mechanical approach such as time dependent density functional theory (TDDFT). The detail of TDDFT can be found in numerous references, [10] so

it will not be discussed here. In summary, the primary purpose of TDDFT is to solve the Kohn-Sham equation, which is similar to Schrödinger's equation. Under Hohenburg-Kohn theorem, a system can be quantum mechanically described using the electron density of the system, approximating the energy of the system as a linear combination of known non-interacting energies and unknown exchange and correlation energies. [11] In the present chapter, an open source, full potential - linearized augmented plane wave code, the Elk FP-LAPW code, will be used. Among various methods to estimate correlation and the exchange coefficient developed, Local Density Approximation (LDA) and Random Phase Approximation (RPA) will be used along with 137 plane wave basis sets and 9 total bands in the first Brillouin zone. Figure 3 shows the real and imaginary part of the wavevector- and frequency-dependent dielectric function of silicon. A typical input file used for the calculation can be found in Appendix B.

2.1.4 Local density of state of plasmons

To better understand this collective electron motion, plasmons, in the structure given in Figure 1, we introduce the concept of the local density of states (LDOS).

Herein, we adopt the conventional definition [12, 13] of the LDOS as measure of how much overlap that is between the dipole source and the harmonic modes of a system. In the structure of our interest, LDOS can be considered as the density of states of localized surface plasmons in the nanocavity from a Gaussian source, since a dipole source can induce localized surface plasmon modes. [14] Furthermore, the electromagnetic enhancement in a nano- and microcavity is direct proportional to the LDOS [15] and is known as purcell effect.

For a normalized eigenfields, LDOS can be defined as [16]

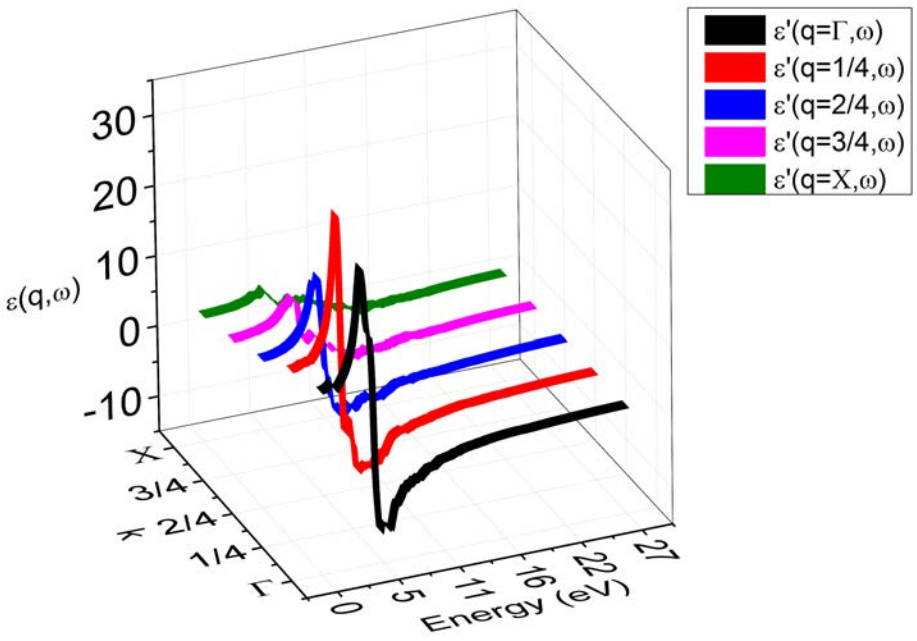

(a) Real part.

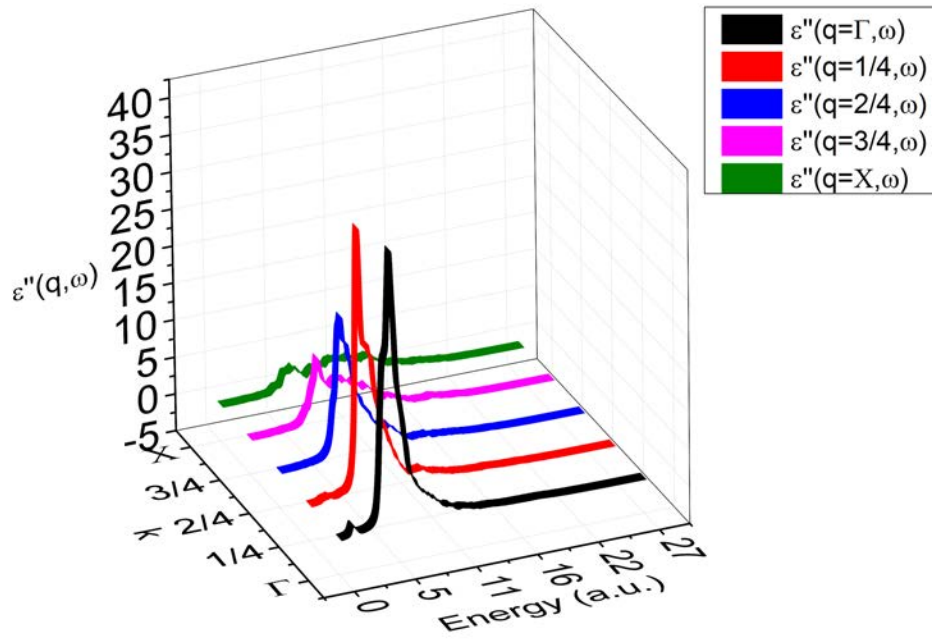

(b) Imaginary part.

Figure 3: Dielectric function of silicon as a function of wavevector and frequency (a) real part (b) imaginary part.

$$LDOS_i(x,\omega) = \sum_n \delta(\omega - \omega^{(n)})\epsilon(x)|E_i^{(n)}(x)|^2 \tag{2.5}$$

Meanwhile, in the lossless limit, using Poynting's theorem and the Lorentzians approach, the radiated power can be obtained:

$$P = \frac{\pi}{4}\left|< \mathbf{E}^{(n)}, \epsilon^{-1}\mathbf{J} >\right|^2 \delta(\omega - \omega^{(n)}) \tag{2.6}$$

By comparing Equation 2.5 and Equation 2.6, we get

$$LDOS_i(x,\omega) = \frac{4}{\pi}\epsilon(x_0)P_i(x_0,\omega) \tag{2.7}$$

Herein, an open source FDTD simulator, MEEP [16], was used. Static dielectric constants are used to specify silicon and silicon dioxide layer, and the Drude-Lorentz model for metal is used to describe the polarizability of silver given by

$$\epsilon_r(\omega) = \sum_{j=1}^{k} \frac{f_j\omega_p^2}{(\omega_j^2 - \omega^2) + i\omega\Gamma_j} \tag{2.8}$$

where ω_p is the plasmon frequency, k is the number of oscillators, ω_j is the frequency of the oscillator, f_j is the strength of the oscillator, and Γ_j is the decay constant. [1]

LDOS of the given sturcture with two polarizations of the dipole source (Gaussian pulse with 140 fs pulse width and central frequency of $6.55 * 10^2$ THz), TM and TE, are used. Comparison

between LDOS of the structure given and a modified structure with no SiO_2 layer is made to observe how the presence of SiO_2 layer makes difference to the LDOS signiture.

The intensity of LDOS was found to be generally greater with transverse magnetic (TM) mode than those with transverse electric (TE) mode Figure 5 depicts the LDOS for the TEz mode and for the TMz mode.

These results regarding polarization of the plasmon provide tools for determining the most suitable laser polarization to maximize the ponderomotive force. Since an electron moves in a circle that is in perpendicular plain to the magnetic field (the field with TEz mode is pointing y axis: in the cylindrical geometry, the electron motion is in the direction of the axis). In addition an electron would move in the same direction as the electric field, so in the cylindrical geometry, it would move in the direction that is perpendicular to the axis. Figure 6 illustrates the motions.

2.2 Optical Absorption in Si-SiO_2-Ag heterostructure

To investigate the plasmon assisted nonlocal optical absorption, one dimensional (1D) approximation is considered first as shown in Figure 7. For the mathematical reasons, TM mode is the only solution exist for 2-interface structures like in this case. [17, 18] Assuming $\mathbf{E}(\mathbf{r}, t) = E(\mathbf{r})e^{i\omega t}$ and starting from Ampere's law in source free region,

$$\nabla \times \mathbf{H} = \epsilon \frac{\partial \mathbf{E}}{\partial t} \tag{2.9}$$

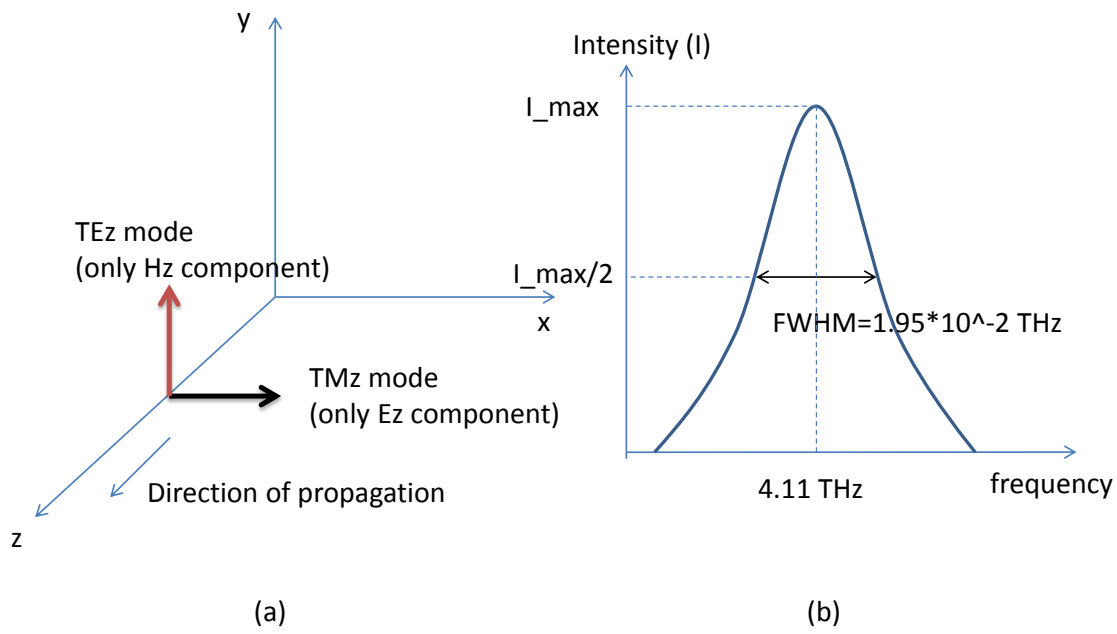

Figure 4: (a) Pulsed TMz and TEz mode of EM fields in position space. The field shapes are delta function in both cases propagating in Z-direction. (b) Gaussian pulse in frequency space. Full-width at half-maximum (FWHM) is $1.95 * 10^{-2}$ Thz and the center frequency is 4.11 THz.

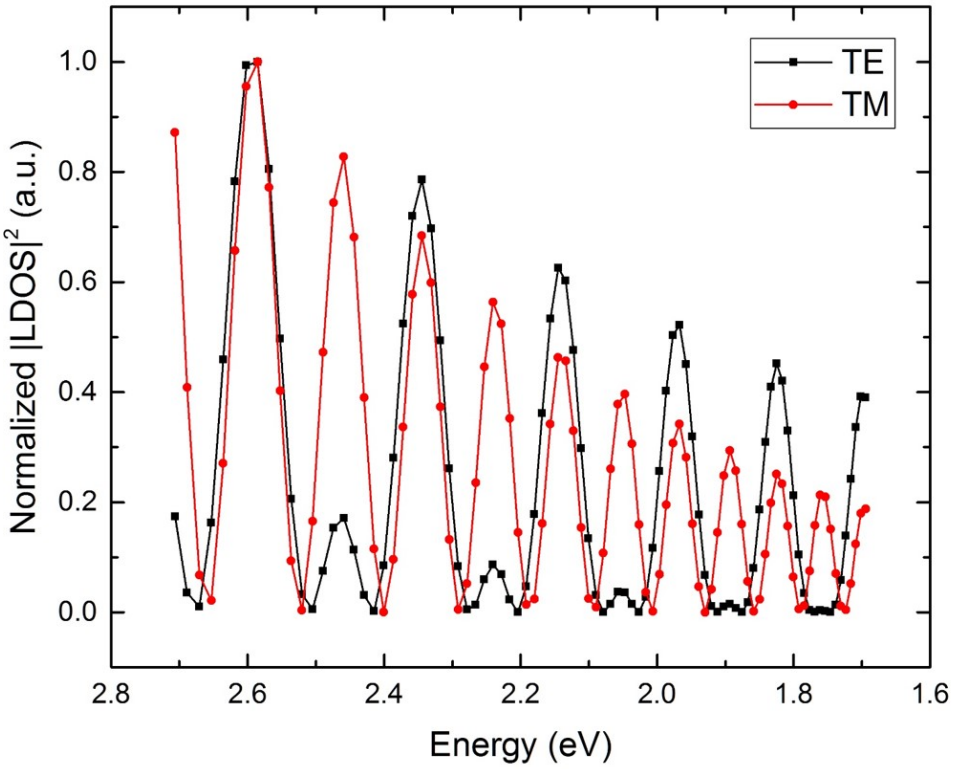

Figure 5: LDOS versus energy with TEz and TMz mode.

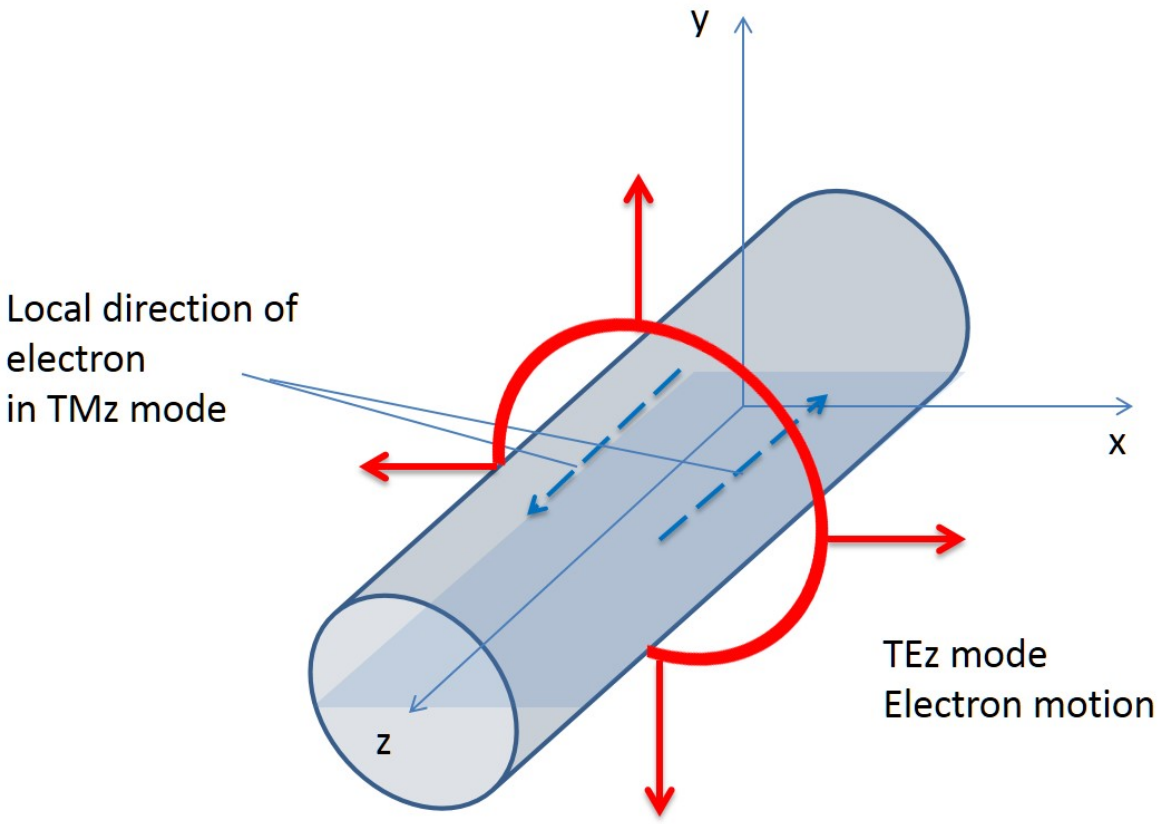

Figure 6: Electron motion in TEz and TMz mode.

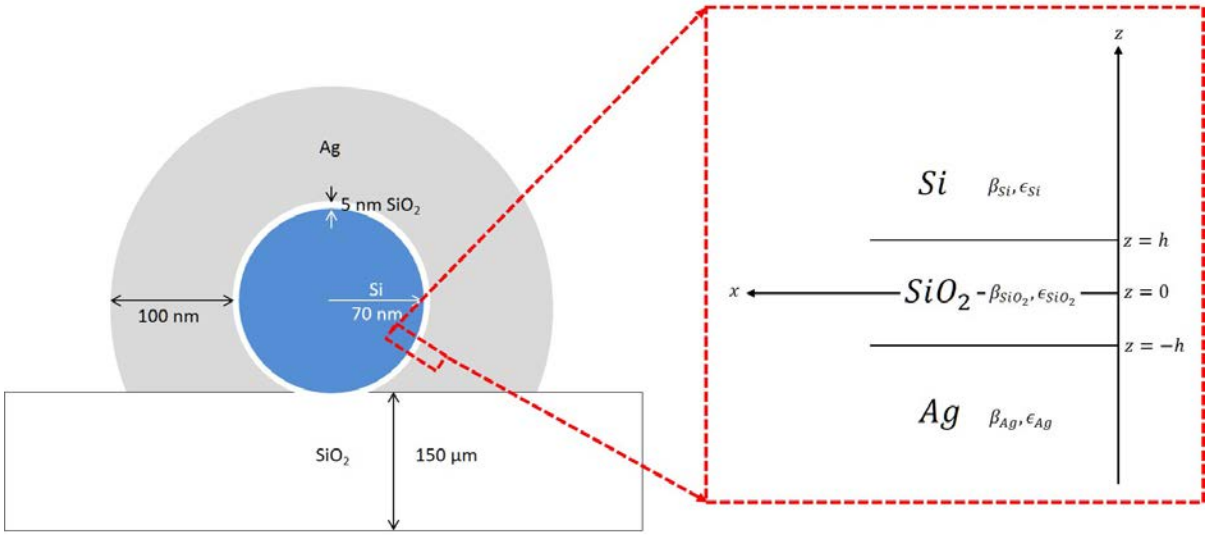

Figure 7: Si-SiO_2-Ag heterostructure.

The wave is time-harmonic TMz mode, and the structure is semi-infinite compared to the wavelength of the wave in x direction. **H** can be written as follows

$$\begin{aligned} \mathbf{H} &= H_y(x,z)e^{i\omega t}\hat{y} = Ae^{i\beta x}e^{-s_1 z}e^{i\omega t}\hat{y} \\ \mathbf{E} &= \tilde{\mathbf{E}}(x,z)e^{i\omega t} \end{aligned} \tag{2.10}$$

Since **H** has only y-component, $\nabla \times \mathbf{H} = -\frac{\partial H_y}{\partial z}\hat{x} + \frac{\partial H_y}{\partial x}\hat{z}$. We can rewrite Equation 2.9

$$\begin{aligned} -\frac{\partial H_y}{\partial z} &= \epsilon\frac{\partial E_x}{\partial t} = i\omega\epsilon E_x \\ \frac{\partial H_y}{\partial x} &= \epsilon\frac{\partial E_z}{\partial t} = i\omega\epsilon E_z = i\beta H_y \end{aligned} \tag{2.11}$$

Equation 2.11 can be rearranged to

$$\begin{aligned} E_x &= \frac{i}{\omega\epsilon}\frac{\partial H_y}{\partial z} \\ E_z &= \frac{\beta}{\omega\epsilon}H_y \end{aligned} \tag{2.12}$$

a general description of transverse magnetic modes are

$$\left.\begin{aligned} H_y(z) &= Ae^{i\beta x}e^{-s_1 z}e^{i\omega t} \\ E_x(z) &= \frac{i}{\omega\epsilon_1\epsilon_0}\frac{\partial H_y}{\partial z} = -iA\frac{1}{\omega\epsilon_1\epsilon_0}s_1 e^{i\beta x}e^{-s_1 z}e^{i\omega t} \\ E_z(z) &= \frac{\beta}{\omega\epsilon_1\epsilon_0}H_y = A\frac{\beta}{\omega\epsilon_1\epsilon_0}e^{i\beta x}e^{-s_1 z}e^{i\omega t} \end{aligned}\right\} \quad \text{z} > h/2 \tag{2.13}$$

$$\left.\begin{aligned} H_y(z) &= Ce^{i\beta x}e^{s_2 z} + De^{i\beta x}e^{-s_2 z}e^{i\omega t} \\ E_x(z) &= \frac{i}{\omega\epsilon_2\epsilon_0}\frac{\partial H_y}{\partial z} = iC\frac{1}{\omega\epsilon_2\epsilon_0}s_2 e^{i\beta x}e^{s_2 z} - iD\frac{1}{\omega\epsilon_2\epsilon_0}s_2 e^{i\beta x}e^{-s_2 z}e^{i\omega t} \\ E_z(z) &= \frac{\beta}{\omega\epsilon_2\epsilon_0}H_y = C\frac{\beta}{\omega\epsilon_2\epsilon_0}e^{i\beta x}e^{s_2 z} - D\frac{\beta}{\omega\epsilon_2\epsilon_0}e^{i\beta x}e^{-s_2 z}e^{i\omega t} \end{aligned}\right\} \quad -h/2 < \mathrm{z} < h/2, \tag{2.14}$$

$$\left.\begin{aligned} H_y(z) &= Be^{i\beta x}e^{s_3 z}e^{i\omega t} \\ E_x(z) &= \frac{i}{\omega\epsilon_3\epsilon_0}\frac{\partial H_y}{\partial z} = iB\frac{1}{\omega\epsilon_3\epsilon_0}s_3 e^{i\beta x}e^{s_3 z}e^{i\omega t} \\ E_z(z) &= \frac{\beta}{\omega\epsilon_3\epsilon_0}H_y = B\frac{\beta}{\omega\epsilon_3\epsilon_0}e^{i\beta x}e^{s_3 z}e^{i\omega t} \end{aligned}\right\} \quad \mathrm{z} < -h/2, \tag{2.15}$$

where

$$s_i = s_{z,i} \;\; (i = 1, 2, 3).$$

The recoprocal value, $1/|s_z|$, is defined as the evanescent decay length, $\hat{z}$. Continuity of H_y and E_x of the interface requires

at z = h/2,

$$Ae^{-s_1 h/2} = Ce^{s_2 h/2} + De^{-s_2 h/2} \tag{2.16}$$

$$A\frac{1}{\epsilon_1}s_1 e^{-s_1 h/2} = C\frac{1}{\epsilon_2}s_2 e^{s_2 h/2} - D\frac{1}{\epsilon_2}s_2 e^{-s_2 h/2} \tag{2.17}$$

and at z = -h/2,

$$Be^{-s_3 h/2} = Ce^{-s_2 h/2} + De^{s_2 h/2} \tag{2.18}$$

$$B\frac{1}{\epsilon_3}s_3 e^{-s_3 h/2} = C\frac{1}{\epsilon_2}s_2 e^{-s_2 h/2} - D\frac{1}{\epsilon_2}s_2 e^{s_2 h/2} \tag{2.19}$$

Equation 2.16-Equation 2.19 can be put in a matrix form:

$$\begin{pmatrix} e^{-s_1 h/2} & 0 & -e^{s_2 h/2} & -e^{-s_2 h/2} \\ \frac{s_1}{\epsilon_1}e^{-s_1 h/2} & 0 & -\frac{s_2}{\epsilon_2}e^{s_2 h/2} & \frac{s_2}{\epsilon_2}e^{-s_2 h/2} \\ 0 & e^{-s_3 h/2} & -e^{-s_2 h/2} & -e^{s_2 h/2} \\ 0 & \frac{s_3}{\epsilon_3}e^{-s_3 h/2} & -\frac{s_2}{\epsilon_2}e^{-s_2 h/2} & \frac{s_2}{\epsilon_2}e^{s_2 h/2} \end{pmatrix} \begin{pmatrix} A \\ B \\ C \\ D \end{pmatrix} = 0 \tag{2.20}$$

In order for a nontrivial solution to exist, the determinant of the matrix should be equal to zero.

Now we solve the wave equation for TM modes,

$$\frac{\partial^2 H_y}{\partial z^2} - \left(k_0^2 \epsilon + \beta^2\right) H_y = 0, \tag{2.21}$$

in each region, we get dispersion relation

$$s_i^2 = \beta^2 - k_0^2 \epsilon_i \;\; (i = 1, 2, 3), \tag{2.22}$$

which has to be satisfied in order for solutions to exist.

Now B, C, and D can be solved in terms of A from Equation 2.16-Equation 2.19. From Equation 2.16, we get

$$Ce^{s_2h/2} = Ae^{-s_1h/2} - De^{-s_2h/2} \tag{2.23}$$

Combining Equation 2.23 and Equation 2.17, we get

$$\begin{aligned} A\frac{1}{\epsilon_1}s_1e^{-s_1h/2} &= \frac{1}{\epsilon_2}s_2\left(Ae^{-s_1h/2} - De^{-s_2h/2}\right) - D\frac{1}{\epsilon_2}s_2e^{-s_2h/2} \\ A\left(\frac{s_2}{\epsilon_2} - \frac{s_1}{\epsilon_1}\right)e^{-s_1h/2} &= 2D\frac{s_2}{\epsilon_2}e^{-s_2h/2} \\ D &= \frac{A}{2}\frac{\epsilon_2}{s_2}\left(\frac{s_2}{\epsilon_2} + \frac{s_1}{\epsilon_1}\right)e^{(s_2-s_1)h/2} \end{aligned} \tag{2.24}$$

Combining Equation 2.24 and Equation 2.23, we get

$$\begin{aligned} Ce^{s_2h/2} &= Ae^{-s_1h/2} - \frac{A}{2}\frac{\epsilon_2}{s_2}\left(\frac{s_2}{\epsilon_2} - \frac{s_1}{\epsilon_1}\right)e^{-s_1h/2} \\ &= Ae^{-s_1h/2}\left[1 - \frac{\epsilon_2}{2s_2}\left(\frac{s_2}{\epsilon_2} - \frac{s_1}{\epsilon_1}\right)\right] \\ C &= Ae^{(-s_1-s_2)h/2}\left(1 + \frac{\epsilon_2 s_1}{2s_2\epsilon_1} - \frac{1}{2}\right) \\ C &= \frac{A}{2}\frac{\epsilon_2}{s_2}\left(\frac{s_2}{\epsilon_2} + \frac{s_1}{\epsilon_1}\right)e^{(-s_1-s_2)h/2} \end{aligned} \tag{2.25}$$

Finally, Combining Equation 2.25 and Equation 2.24 with Equation 2.18, we get

$$\begin{aligned} Be^{-s_3h/2} &= \frac{A}{2}\frac{\epsilon_2}{s_2}\left(\frac{s_2}{\epsilon_2} + \frac{s_1}{\epsilon_1}\right)e^{(-s_1-s_2)h/2}e^{-s_2h/2} + \frac{A}{2}\frac{\epsilon_2}{s_2}\left(\frac{s_2}{\epsilon_2} + \frac{s_1}{\epsilon_1}\right)e^{(s_2-s_1)h/2}e^{s_2h/2} \\ B &= \frac{A}{2}\frac{\epsilon_2}{s_2}\left[\left(\frac{s_2}{\epsilon_2} + \frac{s_1}{\epsilon_1}\right)e^{(-s_1-2s_2)h/2} + \left(\frac{s_2}{\epsilon_2} + \frac{s_1}{\epsilon_1}\right)e^{(-s_1+2s_2)h/2}\right]e^{s_3h/2} \end{aligned} \tag{2.26}$$

Next, substituting Equation 2.24, Equation 2.26, and Equation 2.25 into Equation 2.13, Equation 2.14, and Equation 2.15, $E_x(z)$ and $E_z(z)$ become

$$E_x(z) = \begin{cases} -iA\frac{s_1}{\omega\epsilon_1\epsilon_0}e^{-s_1 z}e^{i\beta x} & \text{z} > h/2 \\ i\frac{A}{2}\frac{1}{\omega\epsilon_0}\left[\left(\frac{s_2}{\epsilon_2}+\frac{s_1}{\epsilon_1}\right)e^{(-s_1-s_2)h/2}e^{s_2 z} - \left(\frac{s_2}{\epsilon_2}+\frac{s_1}{\epsilon_1}\right)e^{(-s_1+s_2)h/2}e^{-s_2 z}\right]e^{i\beta x} & -h/2 < \text{z} < h/2 \\ i\frac{A}{2}\frac{1}{\omega\epsilon_0}\frac{s_3\epsilon_2}{s_2\epsilon_3}\left[\left(\frac{s_2}{\epsilon_2}+\frac{s_1}{\epsilon_1}\right)e^{(-s_1-2s_2)h/2} + \left(\frac{s_2}{\epsilon_2}+\frac{s_1}{\epsilon_1}\right)e^{(-s_1+2s_2)h/2}\right]e^{s_3 h/2}e^{s_3 z}e^{i\beta x} & \text{z} < -h/2 \end{cases} \tag{2.27}$$

and

$$E_z(z) = \begin{cases} A\frac{\beta}{\omega\epsilon_1\epsilon_0}e^{-s_1 z}e^{i\beta x} & \text{z} > h/2 \\ \frac{A}{2}\frac{1}{\omega\epsilon_0}\frac{\beta}{s_2}\left[\left(\frac{s_2}{\epsilon_2}+\frac{s_1}{\epsilon_1}\right)e^{(-s_1-s_2)h/2}e^{s_2 z} + \left(\frac{s_2}{\epsilon_2}+\frac{s_1}{\epsilon_1}\right)e^{(-s_1+s_2)h/2}e^{-s_2 z}\right]e^{i\beta x} & -h/2 < \text{z} < h/2 \\ \frac{A}{2}\frac{\beta}{\omega\epsilon_0}\frac{\epsilon_2}{s_2\epsilon_3}\left[\left(\frac{s_2}{\epsilon_2}+\frac{s_1}{\epsilon_1}\right)e^{(-s_1-2s_2)h/2} + \left(\frac{s_2}{\epsilon_2}+\frac{s_1}{\epsilon_1}\right)e^{(-s_1+2s_2)h/2}\right]e^{s_3 h/2}e^{s_3 z}e^{i\beta x} & \text{z} < -h/2 \end{cases} \tag{2.28}$$

Equation 2.20 gives two solutions, which will be referred as "even mode" and "odd mode" [19] for convenience. The even mode electric fields are expressed as follow:

$$E_{xe}(z) = \begin{cases} -i\frac{s_{Si}^2-\beta_x^2}{\omega\mu_0\epsilon_{Si}\epsilon_0}A_e^{Si}e^{-s_{Si}z}e^{i\beta x} & \text{z} > h/2 \\ -i\frac{s_{SiO_2}^2-\beta_x^2}{\omega\mu_0\epsilon_{SiO_2}\epsilon_0}D_e^{SiO_2}\sin(-s_{SiO_2}z)e^{i\beta x} & -h/2 < \text{z} < h/2 \\ -i\frac{s_{Ag}^2-\beta_x^2}{\omega\mu_0\epsilon_{Ag}\epsilon_0}A_e^{Ag}e^{-s_{Ag}z}e^{i\beta x} & \text{z} < -h/2 \end{cases} \tag{2.29}$$

and

$$E_{ze}(z) = \begin{cases} \frac{s_{Si}\beta_x}{\omega\mu_0\epsilon_{Si}\epsilon_0}A_e^{Si}e^{-s_{Si}z}e^{i\beta x} & \text{z} > h/2 \\ \frac{s_{SiO_2}\beta_x}{\omega\mu_0\epsilon_{SiO_2}\epsilon_0}D_e^{SiO_2}\cos(-s_{Si}z)e^{i\beta x} & -h/2 < \text{z} < h/2 \\ \frac{s_{Ag}\beta_x}{\omega\mu_0\epsilon_{Ag}\epsilon_0}A_e^{Si}e^{-s_{Ag}z}e^{i\beta x} & \text{z} < -h/2 \end{cases} \tag{2.30}$$

And the odd mode electric fields are:

$$E_{xo}(z) = \begin{cases} -i\frac{s_{Si}^2-\beta_x^2}{\omega\mu_0\epsilon_{Si}\epsilon_0}A_e^{Si}e^{-s_{Si}z}e^{i\beta x} & \text{z} > h/2 \\ -i\frac{s_{SiO_2}^2-\beta_x^2}{\omega\mu_0\epsilon_{SiO_2}\epsilon_0}C_e^{SiO_2}\cos\left(-s_{SiO_2}z\right)e^{i\beta x} & -h/2 < \text{z} < h/2 \\ -i\frac{s_{Ag}^2-\beta_x^2}{\omega\mu_0\epsilon_{Ag}\epsilon_0}A_e^{Ag}e^{-s_{Ag}z}e^{i\beta x} & \text{z} < -h/2 \end{cases} \tag{2.31}$$

and

$$E_{zo}(z) = \begin{cases} \frac{s_{Si}\beta_x}{\omega\mu_0\epsilon_{Si}\epsilon_0}A_e^{Si}e^{-s_{Si}z}e^{i\beta x} & \text{z} > h/2 \\ \frac{s_{SiO_2}\beta_x}{\omega\mu_0\epsilon_{SiO_2}\epsilon_0}C_e^{SiO_2}\sin\left(-s_{Si}z\right)e^{i\beta x} & -h/2 < \text{z} < h/2 \\ \frac{s_{Ag}\beta_x}{\omega\mu_0\epsilon_{Ag}\epsilon_0}A_e^{Si}e^{-s_{Ag}z}e^{i\beta x} & \text{z} < -h/2 \end{cases} \tag{2.32}$$

Figure 8 show the electric field pattern of these two modes. The results shows that the confinement of SPP at the interface between Si and SiO_2 is about 5 nm.

Now the power absorption rate of SPP in silicon region can be computed using the electric field. In the classical electromagnetic theory, the power absorption rate is given by

$$P_{abs}(\omega) = \frac{\omega}{2}Im\left[\int \overrightarrow{P}_\omega(\mathbf{r})\cdot\overrightarrow{E}_\omega(\mathbf{r})^* d^3r\right] \tag{2.33}$$

We know the polarization vector $\overrightarrow{P}_\omega = \epsilon_0\tilde{\chi}_\omega\overrightarrow{E}_\omega$, where $\tilde{\chi} = \tilde{\epsilon_r} + 1$ Equation 2.33 becomes

$$P_{abs}(\omega) = \frac{\omega}{2}Im\left[\int \epsilon_0\tilde{\chi}_\omega|E_\omega(r)|^2 d^3r\right] \tag{2.34}$$

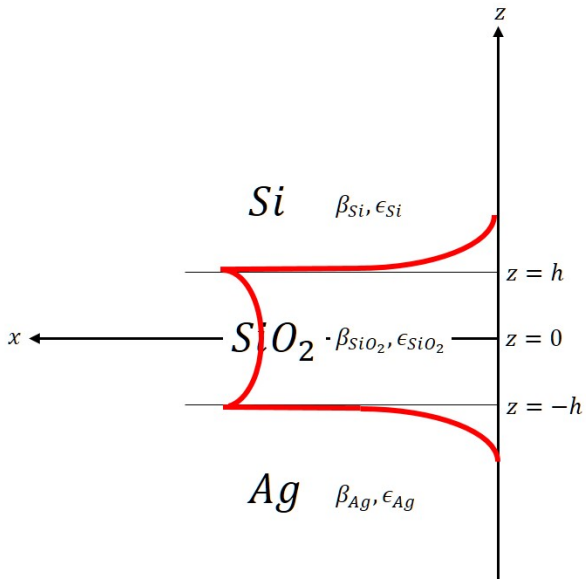

(a) Even mode.

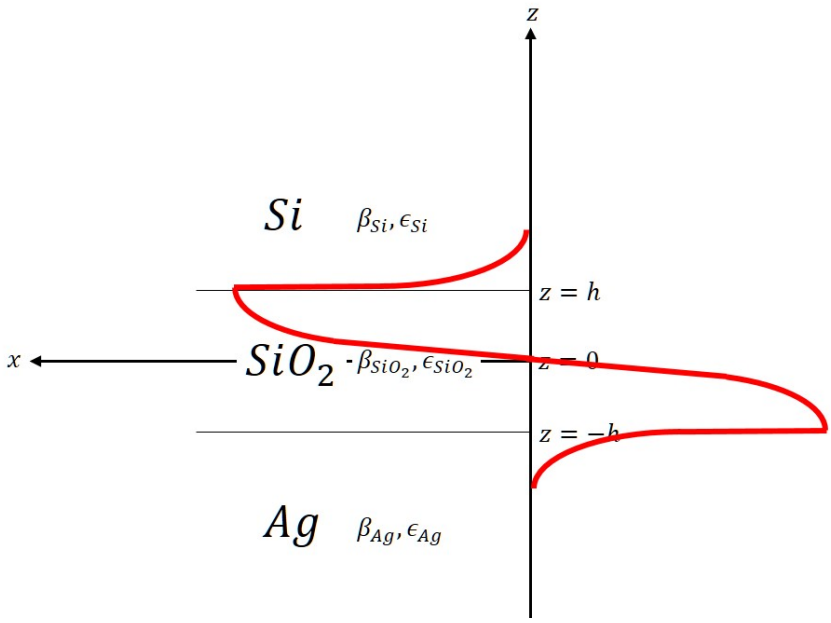

(b) Odd mode.

Figure 8: Electric field pattern in 1D Si-SiO_2-Ag system (a) even mode (b) odd mode.

By Fourier transforming $E_\omega(r)$ and using wavevector- and frequency- dependent susceptibility, the power absorption rate of SPP in silicon region is given by [8]

$$P_{abs}^{Si}(\omega) \approx \frac{\omega\epsilon_0}{4\pi\beta''} \int \frac{|E_x|^2 \tilde{\chi}_{\omega,q}^{xx}}{|s+iq_z|^2} dq_z \tag{2.35}$$

where $\tilde{\chi}_{\omega,q}^{xx}$ is the xx component of the wavevector- and frequency- dependent susceptibility tensor of silicon. Figure 9 show the result. It is suggested that the amplitude of power absorption rate of the even mode are generally greater than that of the odd mode except for the region where the incoming photon energy is larger than 1.4 eV. While more research should be done for the quantitative analysis, the result can qualitatively agree with previous reported experimental results by Cho et. al [4]. This promising result leads to the three dimensional (3D) study.

From the results, the dispersion relation of SPP can be also obtained. Since the limiting frequency of SPP in Si-SiO_2-Ag 1D structure is given by

$$\omega_{SPP}^{max} = \frac{\omega_p^{bulk}}{\sqrt{1+\epsilon_2}} = 4.07eV, \tag{2.36}$$

The projected dispersion relation is shown in Figure 10. From the uncertainty principle, $\Delta x \cdot \Delta p = \Delta x \cdot \hbar\Delta k \geq \frac{\hbar}{2}$. Then, with 5 nm confinement, the uncertainty of the wavevector, Δk, is $1 \times 10^8 m^{-1}$. With the presence of a grating coupler, in this case the roughness of the interface between SiO_2 and Ag, the wavevector can change by $\frac{2\pi}{a}$, where a is the grating period. Considering 120 nm grating period gives $0.6 \times 10^8 m^{-1}$ increase in the wavevector of SPP, the interface roughness will give enough wavevector increase in SPP well over the point indicated

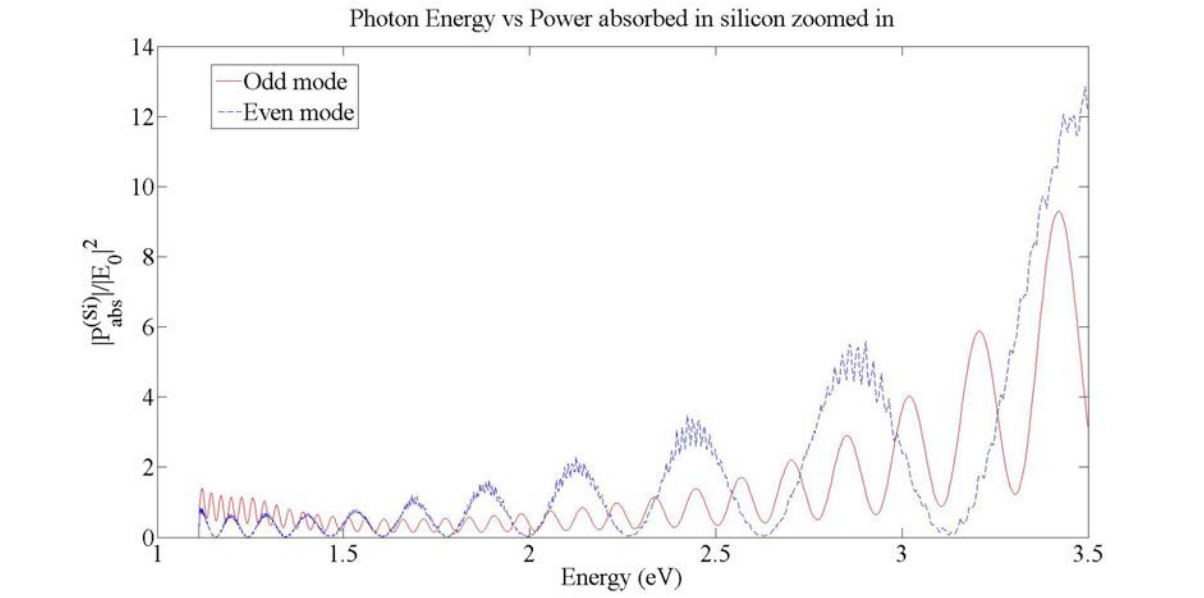

Figure 9: Power absorption rate of SPP in the silicon region in Si-SiO_2-Ag 1D structure. Both even mode and odd mode are shown.

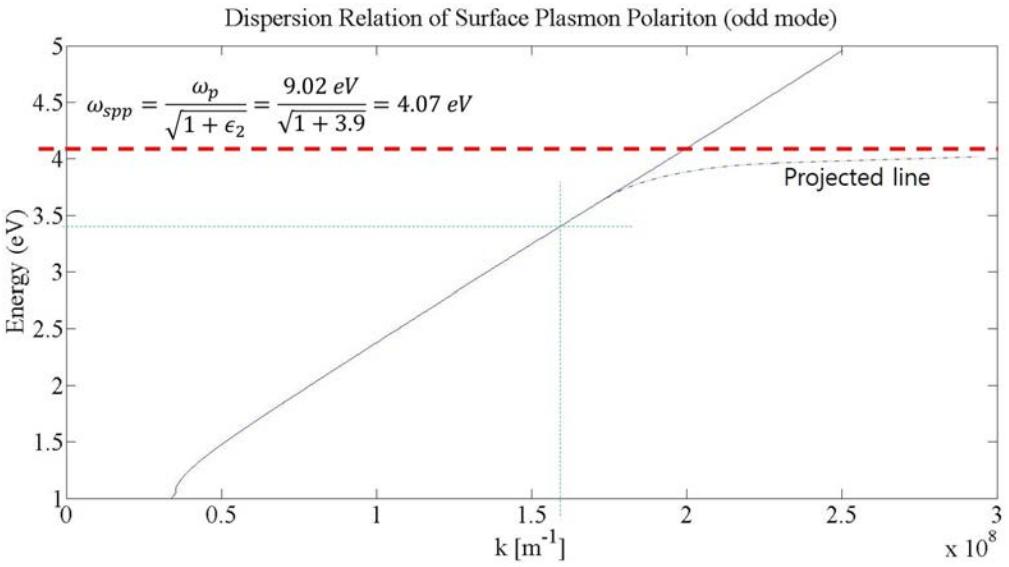

Figure 10: Dispersion relation of SPP in Si-SiO_2-Ag 1D structure. Red dashed line indicates the maximum frequency of SPP, and green dashed line the energy of SPP when its wavevector is $1.6 \times 10^8 m^{-1}$.

as green dashed line in Figure 10 with the corresponding SPP energy of 3.4 eV. This SPP that carries high energy and wavevector can be absorbed by an electron in the valence band of silicon, which can make nonlocal absorption in silicon possible.

2.2.1 Power absorption in Si-Ag cylinder

In this section, the power absorption in 3D structure as shown in Figure 1a will be presented. First, a simplified structure, Si-Ag cylindrical structure, will be studied. In other words, the effect of SiO_2 interlayer will be neglected in the present section.

For the transverse electric to z axis (TE^z) modes, the vector potentials are

$$\mathbf{A} = 0 \tag{2.37a}$$

$$\mathbf{F} = \hat{z}F_z(\rho, \phi, z). \tag{2.37b}$$

Equation 2.37b must satisfy the reduced wave equation for the vector potential $\mathbf{F}$ given as

$$\nabla^2 F_z(\rho, \phi, z) + \beta^2 F_z(\rho, \phi, z) = 0. \tag{2.38}$$

In cylindrical coordinates, Equation 2.38 is expressed by

$$\frac{1}{\rho}\frac{\partial}{\partial\rho}\left(\rho\frac{\partial F_z}{\partial\rho}\right) + \frac{1}{\rho^2}\frac{\partial^2 F_z}{\partial\phi^2} + \frac{\partial^2 F_z}{\partial z^2} + \beta^2 F_z = 0. \tag{2.39}$$

Using separation of variables, a solution of Equation 2.39 can be written in the following form:

$$F_z(\rho, \phi, z) = [A_1 K_m(\beta_\rho \rho) + A_2 I_m(\beta_\rho \rho)][B_1 cos(m\phi) + B_2 sin(m\phi)][G_1 e^{-j\beta_z z} + G_2 e^{+j\beta_z z}], \tag{2.40}$$

where $\beta_\rho^2 + \beta_z^2 = \beta^2$. The ρ component of Equation 2.40 represents evanescent waves which can excite surface plasmon polaritons on the interface. [17] Electric and magnetic field components from the vector potential $\mathbf{F}$ are given by

$$\begin{aligned} E_\rho &= -\frac{1}{\epsilon\rho}\frac{\partial F_z}{\partial \phi}, & H_\rho &= -j\frac{1}{\omega\mu\epsilon}\frac{\partial^2 F_z}{\partial\rho\partial z}, \\ E_\phi &= \frac{1}{\epsilon}\frac{\partial F_z}{\partial \rho}, & H_\phi &= -j\frac{1}{\omega\mu\epsilon}\frac{1}{\rho}\frac{\partial^2 F_z}{\partial\phi\partial z}, \\ E_z &= 0, & H_z &= -j\frac{1}{\omega\mu\epsilon}\left(\frac{\partial^2}{\partial z^2} + \beta^2\right) F_z. \end{aligned} \tag{2.41}$$

Considering only wave that travels in +z direction (i.e. $G_2 = 0$), the vector potential F_z can be written in each region shown in Figure 1a by

$$F_z = \begin{cases} A_{mn} I_m(\beta_\rho^s \rho)\left[B_1 cos(m\phi) + B_2 sin(m\phi)\right] e^{-j\beta_z z}, & 0 < \rho < h \\ D_{mn} K_m(\beta_\rho^A \rho)\left[C_1 cos(m\phi) + C_2 sin(m\phi)\right] e^{-j\beta_z z}, & h < \rho < p \end{cases} \tag{2.42}$$

where $m = 0, 1, 2, \cdots$.

Using Equation 2.41 and Equation 2.42 and assuming the core cylinder is a perfect dielectric (i.e. $\mu = \mu_0$), the electric and magnetic fields in $0 < \rho < h$ region can be expressed by

$$E_\rho^s = -A_{mn}\frac{m}{\epsilon_s \rho} I_m(\beta_\rho^s \rho)\left[B_2 cos(m\phi) - B_1 sin(m\phi)\right] e^{-j\beta_z z} \tag{2.43a}$$

$$E_\phi^s = A_{mn}\frac{\beta_\rho^s}{\epsilon_s} I'_m(\beta_\rho^s \rho)\left[B_1 cos(m\phi) + B_2 sin(m\phi)\right] e^{-j\beta_z z} \tag{2.43b}$$

$$E_z^s = 0 \tag{2.43c}$$

$$H_\rho^s = -A_{mn}\frac{\beta_\rho^s \beta_z}{\omega\mu_0\epsilon_s} I'_m(\beta_\rho^s \rho)\left[B_1 cos(m\phi) + B_2 sin(m\phi)\right] e^{-j\beta_z z} \tag{2.43d}$$

$$H_\phi^s = -A_{mn}\frac{m\beta_z}{\omega\mu_0\epsilon_s}\frac{1}{\rho} I_m(\beta_\rho^s \rho)\left[B_2 cos(m\phi) - B_1 sin(m\phi)\right] e^{-j\beta_z z} \tag{2.43e}$$

$$H_z^s = -jA_{mn}\frac{\left(\beta_\rho^s\right)^2}{\omega\mu_0\epsilon_s} I_m(\beta_\rho^s \rho)\left[B_1 cos(m\phi) + B_2 sin(m\phi)\right] e^{-j\beta_z z}, \tag{2.43f}$$

and in $h < \rho < p$ region by

$$E_\rho^A = -D_{mn}\frac{m}{\epsilon_A \rho} K_m(\beta_\rho^A \rho)\left[C_2 cos(m\phi) - C_1 sin(m\phi)\right] e^{-j\beta_z z} \tag{2.44a}$$

$$E_\phi^A = D_{mn}\frac{\beta_\rho^A}{\epsilon_A} K'_m(\beta_\rho^A \rho)\left[C_1 cos(m\phi) + C_2 sin(m\phi)\right] e^{-j\beta_z z} \tag{2.44b}$$

$$E_z^A = 0 \tag{2.44c}$$

$$H_\rho^A = -D_{mn}\frac{\beta_\rho^A \beta_z}{\omega\mu_0\epsilon_A} K'_m(\beta_\rho^A \rho)\left[C_1 cos(m\phi) + C_2 sin(m\phi)\right] e^{-j\beta_z z} \tag{2.44d}$$

$$H_\phi^A = -D_{mn}\frac{m\beta_z}{\omega\mu_0\epsilon_A}\frac{1}{\rho} K_m(\beta_\rho^A \rho)\left[C_2 cos(m\phi) - C_1 sin(m\phi)\right] e^{-j\beta_z z} \tag{2.44e}$$

$$H_z^A = -jD_{mn}\frac{\left(\beta_\rho^A\right)^2}{\omega\mu_0\epsilon_A} K_m(\beta_\rho^A \rho)\left[C_1 cos(m\phi) + C_2 sin(m\phi)\right] e^{-j\beta_z z}. \tag{2.44f}$$

Similarly, by letting

$$\mathbf{A} = \hat{z} A_z(\rho, \phi, z) \tag{2.45a}$$

$$\mathbf{F} = 0, \tag{2.45b}$$

the electric and magnetic fields for the transeverse magnetic to z axis (TM_z) in $0 < \rho < h$ region modes can written as

$$E_\rho^s = -P_{mn} \frac{\beta_\rho^s \beta_z}{\omega \mu_0 \epsilon_s} I_m'(\beta_\rho^s \rho) \left[B_1 cos(m\phi) + B_2 sin(m\phi) \right] e^{-j\beta_z z} \tag{2.46a}$$

$$E_\phi^s = -P_{mn} \frac{m \beta_z}{\omega \mu_0 \epsilon_s} \frac{1}{\rho} I_m(\beta_\rho^s \rho) \left[B_2 cos(m\phi) - B_1 sin(m\phi) \right] e^{-j\beta_z z} \tag{2.46b}$$

$$E_z^s = -j P_{mn} \frac{\left(\beta_\rho^s\right)^2}{\omega \mu_0 \epsilon_s} I_m(\beta_\rho^s \rho) \left[B_1 cos(m\phi) + B_2 sin(m\phi) \right] e^{-j\beta_z z} \tag{2.46c}$$

$$H_\rho^s = P_{mn} \frac{m}{\mu_0} \frac{1}{\rho} I_m(\beta_\rho^s \rho) \left[B_2 cos(m\phi) - B_1 sin(m\phi) \right] e^{-j\beta_z z} \tag{2.46d}$$

$$H_\phi^s = -P_{mn} \frac{\beta_\rho^s}{\mu_0} I_m'(\beta_\rho^s \rho) \left[B_1 cos(m\phi) + B_2 sin(m\phi) \right] e^{-j\beta_z z} \tag{2.46e}$$

$$H_z^s = 0, \tag{2.46f}$$

and in $h < \rho < p$ region as

$$E_\rho^A = -Q_{mn}\frac{\beta_\rho^A \beta_z}{\omega\mu_0\epsilon_A}K'_m(\beta_\rho^A\rho)\left[C_1 cos(m\phi) + C_2 sin(m\phi)\right]e^{-j\beta_z z} \tag{2.47a}$$

$$E_\phi^A = -Q_{mn}\frac{m\beta_z}{\omega\mu_0\epsilon_A}\frac{1}{\rho}K_m(\beta_\rho^A\rho)\left[C_2 cos(m\phi) - C_1 sin(m\phi)\right]e^{-j\beta_z z} \tag{2.47b}$$

$$E_z^A = -jQ_{mn}\frac{\left(\beta_\rho^A\right)^2}{\omega\mu_0\epsilon_A}K_m(\beta_\rho^A\rho)\left[C_1 cos(m\phi) + C_2 sin(m\phi)\right]e^{-j\beta_z z} \tag{2.47c}$$

$$H_\rho^A = Q_{mn}\frac{m}{\mu_0}\frac{1}{\rho}K_m(\beta_\rho^A\rho)\left[C_2 cos(m\phi) - C_1 sin(m\phi)\right]e^{-j\beta_z z} \tag{2.47d}$$

$$H_\phi^A = -Q_{mn}\frac{\beta_\rho^A}{\mu_0}K'_m(\beta_\rho^A\rho)\left[C_1 cos(m\phi) + C_2 sin(m\phi)\right]e^{-j\beta_z z} \tag{2.47e}$$

$$H_z^A = 0. \tag{2.47f}$$

For a cylindrical structure, pure TE or TM modes cannot exist unless the fields have azimuthal symmetry. [20] In general, the electric and magnetic fields exist in combinations of both TE and TM mode, namely hybrid modes. The hybrid modes or HEM modes, standardized by IEEE, [**?**] can be written by selecting $cos(m\phi)$ variation terms for E_z and $sin(m\phi)$ variation terms for H_z and taking a linear combination of TE and TM modes:

$0 < \rho < h$ region

$$E_\rho^s = -j\frac{1}{\left(\beta_\rho^s\right)^2}\left[m\omega\mu_0 A_m\frac{1}{\rho}I_m(\beta_\rho^s\rho) + \beta_z\beta_\rho^s B_m I_m'(\beta_\rho^s\rho)\right]cos(m\phi)e^{-j\beta_z z} \tag{2.48a}$$

$$E_\phi^s = j\frac{1}{\left(\beta_\rho^s\right)^2}\left[\omega\mu_0\beta_\rho^s A_m I_m'(\beta_\rho^s\rho) + m\beta_z B_m\frac{1}{\rho}I_m(\beta_\rho^s\rho)\right]sin(m\phi)e^{-j\beta_z z} \tag{2.48b}$$

$$E_z^s = B_m I_m(\beta_\rho^s\rho)cos(m\phi)e^{-j\beta_z z} \tag{2.48c}$$

$$H_\rho^s = -j\frac{1}{\left(\beta_\rho^s\right)^2}\left[\beta_z\beta_\rho^s A_m I_m'(\beta_\rho^s\rho) + m\omega\epsilon_s B_m\frac{1}{\rho}I_m(\beta_\rho^s\rho)\right]sin(m\phi)e^{-j\beta_z z} \tag{2.48d}$$

$$H_\phi^s = -j\frac{1}{\left(\beta_\rho^s\right)^2}\left[m\beta_z\frac{1}{\rho}A_m I_m(\beta_\rho^s\rho) + \omega\epsilon_s\beta_\rho^s B_m I_m'(\beta_\rho^s\rho)\right]cos(m\phi)e^{-j\beta_z z} \tag{2.48e}$$

$$H_z^s = A_m I_m(\beta_\rho^s\rho)sin(m\phi)e^{-j\beta_z z}, \tag{2.48f}$$

where

$$\left(\beta_\rho^s\right)^2 + \beta_z^2 = \beta_s^2 = \frac{\omega^2}{c^2}\epsilon_s \tag{2.48g}$$

$$A_m = -j\frac{\left(\beta_\rho^s\right)^2}{\omega\mu_0\epsilon_s}A_{mn}B_2 \tag{2.48h}$$

$$B_m = -j\frac{\left(\beta_\rho^s\right)^2}{\omega\mu_0\epsilon_s}D_{mn}B_1 \tag{2.48i}$$

$$' \equiv \frac{\partial}{\partial(\beta_\rho^s\rho)}, \tag{2.48j}$$

$h < \rho < p$ region as

$$E_\rho^A = -j\frac{1}{\left(\beta_\rho^A\right)^2}\left[m\omega\mu_0 C_m\frac{1}{\rho}K_m(\beta_\rho^A\rho) + \beta_z\beta_\rho^A D_m K_m'(\beta_\rho^A\rho)\right]cos(m\phi)e^{-j\beta_z z} \tag{2.49a}$$

$$E_\phi^A = j\frac{1}{\left(\beta_\rho^A\right)^2}\left[\omega\mu_0\beta_\rho^A C_m K_m'(\beta_\rho^A\rho) + m\beta_z D_m\frac{1}{\rho}K_m(\beta_\rho^A\rho)\right]sin(m\phi)e^{-j\beta_z z} \tag{2.49b}$$

$$E_z^A = D_m K_m(\beta_\rho^A\rho)cos(m\phi)e^{-j\beta_z z} \tag{2.49c}$$

$$H_\rho^A = -j\frac{1}{\left(\beta_\rho^A\right)^2}\left[\beta_z\beta_\rho^A C_m K_m'(\beta_\rho^A\rho) + m\omega\epsilon_A D_m\frac{1}{\rho}K_m(\beta_\rho^A\rho)\right]sin(m\phi)e^{-j\beta_z z} \tag{2.49d}$$

$$H_\phi^A = -j\frac{1}{\left(\beta_\rho^A\right)^2}\left[m\beta_z\frac{1}{\rho}C_m K_m(\beta_\rho^A\rho) + \omega\epsilon_A\beta_\rho^A D_m K_m'(\beta_\rho^A\rho)\right]cos(m\phi)e^{-j\beta_z z} \tag{2.49e}$$

$$H_z^A = C_m K_m(\beta_\rho^A\rho)sin(m\phi)e^{-j\beta_z z}, \tag{2.49f}$$

where

$$\left(j\beta_\rho^A\right)^2 + \beta_z^2 = -\left(\beta_\rho^A\right)^2 + \beta_z^2 = \beta_A^2 = \frac{\omega^2}{c^2}\epsilon_A \tag{2.49g}$$

$$C_m = -j\frac{\left(\beta_\rho^s\right)^2}{\omega\mu_0\epsilon_s}P_{mn}C_2 \tag{2.49h}$$

$$D_m = -j\frac{\left(\beta_\rho^s\right)^2}{\omega\mu_0\epsilon_s}Q_{mn}C_1 \tag{2.49i}$$

$$' \equiv \frac{\partial}{\partial(\beta_\rho^A\rho)}. \tag{2.49j}$$

At $\rho = h$, the tengential component of the electric and magnetic fields,$E_\phi(\rho = h, 0 < \phi < 2\pi, z), E_z(\rho = h, 0 < \phi < 2\pi, z), H_\phi(\rho = h, 0 < \phi < 2\pi, z)$, and $H_z(\rho = h, 0 < \phi < 2\pi, z)$, must

be continuous. These boundary conditions leads to find the coefficients $A_m, B_m, C_m,$ and D_m. By applying all four conditions, Equation 2.49 becomes

$$A_m I_m(\beta_\rho^s h) - C_m K_m(\beta_\rho^A h) = 0 \tag{2.50a}$$

$$B_m I_m(\beta_\rho^s h) - D_m K_m(\beta_\rho^A h) = 0 \tag{2.50b}$$

$$\frac{1}{\left(\beta_\rho^s\right)^2}\left[\omega\mu_0\beta_\rho^s A_m I_m'(\beta_\rho^s h) + m\beta_z B_m \frac{1}{h} I_m(\beta_\rho^s h)\right] + \frac{1}{\left(\beta_\rho^A\right)^2}\left[\omega\mu_0\beta_\rho^A C_m K_m'(\beta_\rho^A h) + m\beta_z D_m \frac{1}{h} K_m(\beta_\rho^A h)\right] = 0 \tag{2.50c}$$

$$\frac{1}{\left(\beta_\rho^s\right)^2}\left[m\beta_z A_m \frac{1}{h} I_m(\beta_\rho^s h) + \omega\epsilon_s\beta_\rho^s B_m I_m'(\beta_\rho^s h)\right] + \frac{1}{\left(\beta_\rho^A\right)^2}\left[m\beta_z C_m \frac{1}{h} K_m(\beta_\rho^A h) + \omega\epsilon_A\beta_\rho^A D_m K_m'(\beta_\rho^A h)\right] = 0. \tag{2.50d}$$

Equation 2.50 can be put in a matrix form, $\mathbf{M}\overrightarrow{\mathbf{x}} = 0$, where $\overrightarrow{\mathbf{x}} = \begin{pmatrix} A_m \\ B_m \\ C_m \\ D_m \end{pmatrix}$ and

$$\mathbf{M} = \begin{pmatrix} I_m(\beta_\rho^s h) & 0 & -K_m(\beta_\rho^A h) & 0 \\ 0 & I_m(\beta_\rho^s h) & 0 & -K_m(\beta_\rho^A h) \\ \frac{\omega\mu_0}{\beta_\rho^s} I_m'(\beta_\rho^s h) & \frac{m\beta_z}{\left(\beta_\rho^s\right)^2 h} I_m(\beta_\rho^s h) & \frac{\omega\mu_0}{\beta_\rho^A} K_m'(\beta_\rho^A h) & \frac{m\beta_z}{\left(\beta_\rho^A\right)^2 h} K_m(\beta_\rho^A h) \\ \frac{m\beta_z}{\left(\beta_\rho^s\right)^2 h} I_m(\beta_\rho^s h) & \frac{\omega\epsilon_s}{\beta_\rho^s} I_m'(\beta_\rho^s h) & \frac{m\beta_z}{\left(\beta_\rho^A\right)^2 h} K_m(\beta_\rho^A h) & \frac{\omega\epsilon_A}{\beta_\rho^A} K_m'(\beta_\rho^A h) \end{pmatrix} \tag{2.51}$$

In order for a nontrivial solution to exist, the determinant of the matrix $\mathbf{M}$) should be equal to zero. This, Equation 2.48g, and Equation 2.49g can be solved numerically find β_ρ^s and β_ρ^A for each ω, then the coefficients A_m through D_m can be found for each m.

Using the similar approach used in 1D analysis, the electric field and the power absorption rate can be found. Figure 11 show typical patterns of the electric field in silicon region in 3D Si-

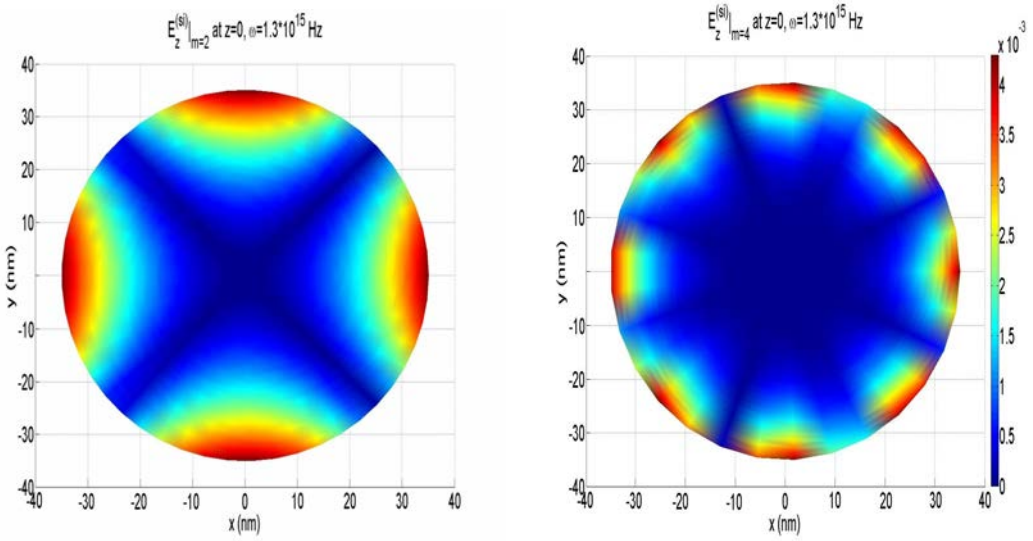

(a) m=2 mode. (b) m=4 mode.

Figure 11: Selected electric field pattern in silicon region in 3D Si-Ag system (a) m=2 mode (b) m=4 mode.

Ag system. These types of electric field patten in cylindrical geometries are sometimes referred as "whispering gallery mode" [21] which can open up many possibilities in optical society.

The power absorption rate in 3D Si-Ag structure can be computed similarly to the 1D case. However, the Hankel transformation is used instead of the Fourier transform to consider the non-locality. [22] That is:

$$G_n(k) = \int_0^{infty} g_n(r) J_n(kr) \sqrt{kr} dr, \tag{2.52}$$

where

$$J_n(kr) = \frac{1}{2\pi} \int_{\phi_0}^{2\pi+\phi_0} e^{[i(n\phi - kr\sin(\phi))]} d\phi. \tag{2.53}$$

Then the power absorption in silicon region in 3D Si-Ag structure is given by

$$P_{abs}^{Si}(\omega) = \frac{\omega\epsilon_0}{2} Im \left[\int \left(\tilde{\chi}_{\omega,q}^{\rho} + \tilde{\chi}_{\omega,q}^{\phi} + \tilde{\chi}_{\omega,q}^{z} \right) \frac{|E_x|^2}{|s + iq_z|^2} dq_z \right]. \tag{2.54}$$

The susceptibility tensor elements can be obtained from the tensor transformation of the Cartesian coordinate susceptibility tensor described in Appendix A.

$I'_m(x)$ and $K'_m(x)$ can be calculated using the recurrence relations of the modified Bessel functions which is given by [23, 24]

$$H'_m(x) = \frac{1}{2} \left[H_{m-1}(X) + H_{m+1}(x) \right], \tag{2.55}$$

where H_m is I_m or K_m.

2.3 Second-order absorption process

In the present section, another possible light absorption mechanism in silicon will be presented. It is often referred to second order process that has been proposed many times for indirect band gap materials. [25–29] Phonon dispersion relation of Si and the density of state of three major phonons in SiO_2 are presented first. Then a theory of massive number of phonon generation will be discussed proceeded by the scattering rate calculation.

2.3.1 Phonons in Silicon and Silicon Dioxide

2.3.1.1 Phonon Dispersion Relation of Silicon

Phonon dispersion relation of silicon is studies in depth, and widely known by far. There are many utilities available to calculate the phonon dispersion relation of silicon, but General Utility Lattice Program (GULP) was used to calculate the phonon dispersion in the first Brillouin zone of silicon [30] The result is presented in Figure 12.

2.3.1.2 Phonon density of State of Silicon Dioxide

There are three major phonons that play the significant role in atomic interactions known in SiO_2: two longitudinal optical (LO) phonons and a acoustic phonon. [31] The density of states of phonons in SiO_2 were calculated using GULP [30] and presented in Figure 13.

2.3.2 Bloembergen's derivation

When the electromagnetic field pulse is sufficiently short comparing to the phonon mode of a material, impulsive stimulated scattering (ISS) can occur [32]. Unlike phonons generated from ordinary scattering processes, the phonons generated as a result of ISS are in the same

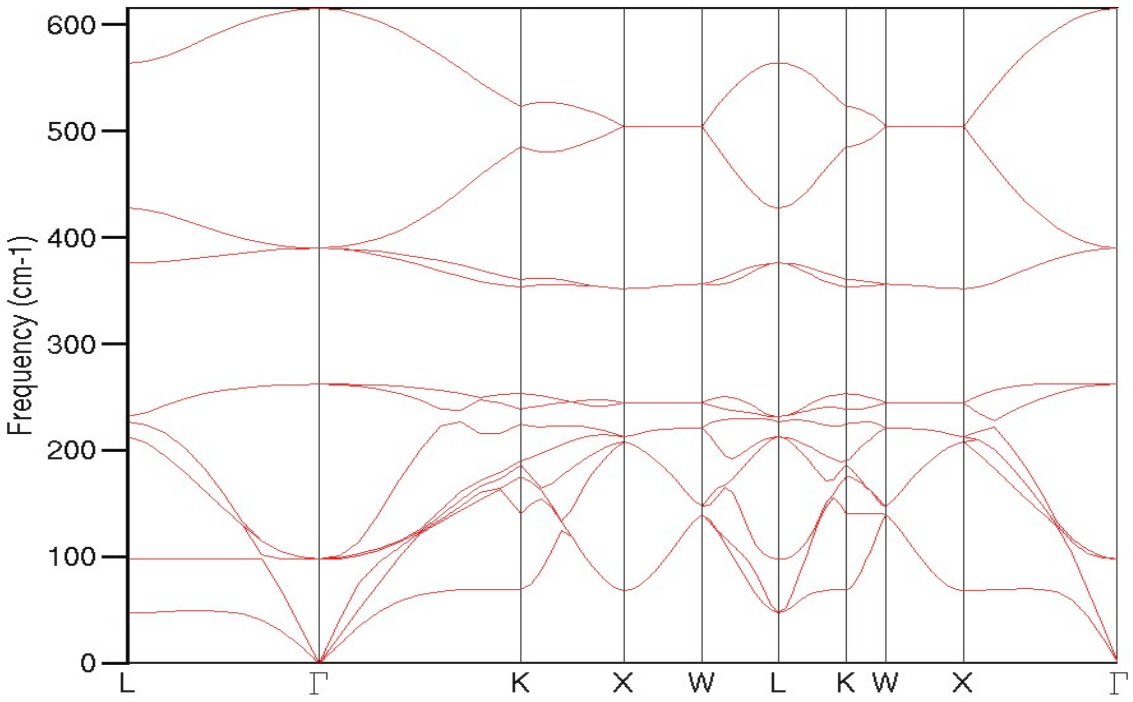

Figure 12: Phonon dispersion relation of silicon in the first Brillouin zone.

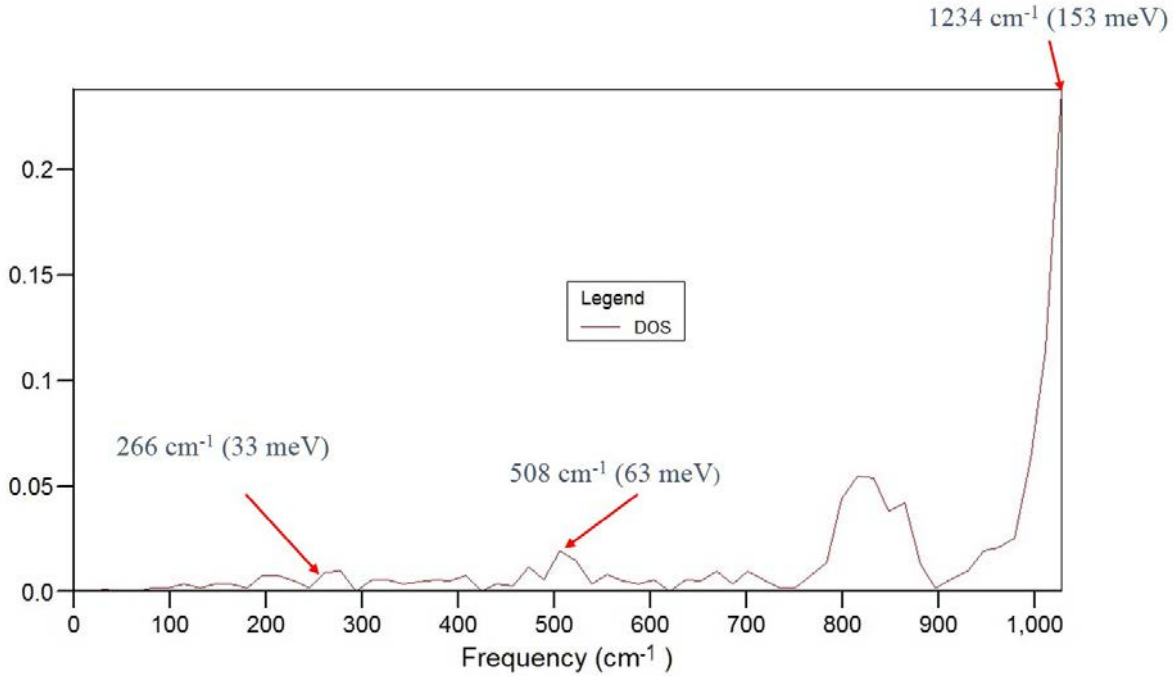

Figure 13: Phonon density of state of SiO_2.

mode. These "coherent" phonons, which can be *"selected"* [33], would have high phonon occupation number. On the other hand, laser incident on metal creates plasmons at the metal-SiO_2 interface. Since surface plasmon polaritons can be defined as a specific set of surface electromagnetic modes [34], we assume the plasmons as an amplified electric field in this abstract; the magnitude of triggering pulse will be treated as a product of the Purcell enhancement factor, the magnitude of the electric pulse, and the plasmon efficiency.

The term "plasmon efficiency" used here is defined as the amount of energy that goes to create surface plasmons from a triggering electric field. This can be calculated by computing the transmittance of incoming (triggering) electric field from source location to silver, assuming transmitted electromagnetic energy is entirely used to generate surface plasmons.

We begin with the equation of motion for stimulated Raman scattering in Lagrangian mechanics, which is given by:

$$\frac{\partial}{\partial t}\left(\frac{\partial L}{\partial \dot{\mathbf{Q}}}\right) - \frac{\partial L}{\partial \mathbf{Q}} = 0 \tag{2.56}$$

where L is the Lagrangian density given by:

$$L = L_{rad} + L_{vib} + L_{int} \tag{2.57}$$

where, (2.58)

$$L_{rad} = \frac{1}{2}\left(E^2 - B^2\right) \tag{2.59}$$

$$L_{vib} = \frac{1}{2}\dot{\mathbf{Q}}_\nu^2 + \frac{1}{2}\omega_0^2\mathbf{Q}_\nu^2 + \frac{1}{2}\beta\left(\nabla\mathbf{Q}_\nu\right)^2 \tag{2.60}$$

$$L_{int} = N\alpha\mathbf{E}\mathbf{E} \tag{2.61}$$

$$\mathbf{Q}_\nu = \mathbf{R}\sqrt{2\rho} \tag{2.62}$$

where $\mathbf{R}$ is the relative displacement and ρ is the reduced mass density. The optical polarizability α is given by the Placzek model: [32]

$$\alpha = \alpha_0 + \left(\frac{\partial\alpha}{\partial\mathbf{Q}_\nu}\right)_0 \mathbf{Q}_\nu. \tag{2.63}$$

Here,

$$\begin{aligned}
\frac{\partial}{\partial t}\left(\frac{\partial L}{\partial\dot{\mathbf{Q}}}\right) &= \frac{\partial}{\partial t}\left(\dot{\mathbf{Q}}_\nu\right) = \ddot{\mathbf{Q}}_\nu \\
\frac{\partial L}{\partial\mathbf{Q}} &= \frac{\partial}{\partial\mathbf{Q}}\left(-\frac{1}{2}\omega_0^2\mathbf{Q}_\nu^2 + \frac{1}{2}\beta\left(\nabla\mathbf{Q}_\nu\right)^2 + N\left(\alpha_0 + \left(\frac{\partial\alpha}{\partial\mathbf{Q}_\nu}\right)_0\mathbf{Q}_\nu\right)\mathbf{E}\mathbf{E}\right) \\
&= -\omega_0^2\mathbf{Q}_\nu + \frac{1}{2}\beta\frac{\partial}{\partial\mathbf{Q}}\left(\nabla\mathbf{Q}_\nu\right)^2 + \frac{\partial}{\partial\mathbf{Q}}\left(N\left(\frac{\partial\alpha}{\partial\mathbf{Q}_\nu}\right)_0\mathbf{Q}_\nu\mathbf{E}\mathbf{E}\right) \\
&= -\omega_0^2\mathbf{Q}_\nu + \beta\nabla^2\mathbf{Q}_\nu + N\left(\frac{\partial\alpha}{\partial\mathbf{Q}_\nu}\right)_0\mathbf{E}\mathbf{E}.
\end{aligned} \tag{2.64}$$

Then, the equation of motion becomes:

$$\begin{aligned} \frac{\partial}{\partial t}\left(\frac{\partial L}{\partial \dot{\mathbf{Q}}}\right) - \frac{\partial L}{\partial \mathbf{Q}} &= 0 \\ \ddot{\mathbf{Q}}_\nu + \omega_0^2 \mathbf{Q}_\nu - \beta \nabla^2 \mathbf{Q}_\nu - N\left(\frac{\partial \alpha}{\partial \mathbf{Q}_\nu}\right)_0 \mathbf{EE} &= 0. \end{aligned} \tag{2.65}$$

After adding a phenomenological damping term $2\Gamma\mathbf{Q}_\nu$, the equation is:

$$\ddot{\mathbf{Q}}_\nu + \omega_0^2 \mathbf{Q}_\nu - \beta \nabla^2 \mathbf{Q}_\nu + 2\Gamma \mathbf{Q}_\nu = N\left(\frac{\partial \alpha}{\partial \mathbf{Q}_\nu}\right)_0 \mathbf{EE}, \tag{2.66}$$

where the dispersion relation of the vibration is given by:

$$\omega_\nu = \sqrt{\omega_0^2 - \beta k_\nu^2}. \tag{2.67}$$

Assuming $\mathbf{Q}_\nu \sim e^{-i\omega_\nu t}$, Equation 2.66 becomes:

$$\beta \nabla^2 \mathbf{Q}_\nu + \left(\omega_0^2 - \omega_\nu^2\right) \mathbf{Q}_\nu - i2\omega_\nu \Gamma \mathbf{Q}_\nu = N\left(\frac{\partial \alpha}{\partial \mathbf{Q}_\nu}\right)_0 \mathbf{EE}. \tag{2.68}$$

2.3.2.1 The Wave Equation

Assuming there is only three waves, the vibrational wave (optical phonon) at ω_ν, the incoming electric field (laser field) at ω_l, and the SPP wave in the dielectric at ω_s with $\omega_l - \omega_s = \omega\nu$, the wave equation in cgs unit for $\mathbf{E}_s$ is given by:

$$\begin{aligned}
\nabla \times \mathbf{E_s} &= -\frac{1}{c}\frac{\partial \mathbf{B_s}}{\partial t} \\
\nabla \times \mathbf{B_s} &= \frac{4\pi}{c}\mathbf{J_s} + \frac{1}{c}\epsilon_s \frac{\partial \mathbf{E_s}}{\partial t} \\
\nabla \times (\nabla \times \mathbf{E_s}) &= -\frac{1}{c}\frac{\partial}{\partial t}(\nabla \times \mathbf{B_s}) \\
&= -\frac{1}{c^2}\left(4\pi \frac{\partial \mathbf{J_s}}{\partial t} + \epsilon_s \frac{\partial^2 \mathbf{E_s}}{\partial t^2}\right).
\end{aligned} \tag{2.69}$$

For the case of electric dipole [35]

$$\nabla \times (\nabla \times \mathbf{E_s}) - \frac{\omega_s^2 \epsilon_s}{c^2}\mathbf{E_s} = 4\pi \frac{\omega_s^2}{c^2}\mathbf{J} = 4\pi \frac{\omega_s^2}{c^2}\mathbf{P}_s, \tag{2.70}$$

where,

$$\begin{aligned}
\mathbf{P}_s &= \mathbf{P}^{Linear} = N\alpha \mathbf{E}_{local} \\
\mathbf{E}_{local} &= \mathbf{E}_l.
\end{aligned} \tag{2.71}$$

So the wave equation for $\mathbf{E}_s$ becomes:

$$\nabla \times (\nabla \times \mathbf{E_s}) - \frac{\omega_s^2 \epsilon_s}{c^2}\mathbf{E_s} = 4\pi \frac{\omega_s^2}{c^2} N \left(\frac{\partial \alpha}{\partial \mathbf{Q}_\nu}\right)_0 \mathbf{Q}_\nu \mathbf{E}_l. \tag{2.72}$$

From Equation 2.68, we find:

$$\mathbf{Q}_\nu = N\left(\frac{\partial\alpha}{\partial\mathbf{Q}_\nu}\right)_0 \mathbf{E}_l\mathbf{E}_s^*/\left(\beta k_\nu^2 + \omega_0^2 - \omega_\nu^2 - i2\omega_\nu\Gamma\right). \tag{2.73}$$

Substituting Equation 2.73 into Equation 2.72, we get

$$\nabla\times(\nabla\times\mathbf{E_s}) - \frac{\omega_s^2}{c^2}[\epsilon_s + 4\pi\chi_R\mathbf{E}_l\mathbf{E}_l^*]\mathbf{E_s} = 0, \tag{2.74}$$

where,

$$\chi_R = -N\left(\frac{\partial\alpha}{\partial\mathbf{Q}_\nu}\right)_0 : N\left(\frac{\partial\alpha}{\partial\mathbf{Q}_\nu}\right)_0 / \left(\beta k_\nu^2 + \omega_0^2 - \omega_\nu^2 - i2\omega_\nu\Gamma\right). \tag{2.75}$$

From the Maxwell's equations, letting ϵ_2 region be the metal and ϵ_2 region be the dielectric, we get:

$$\mathbf{E}_l = \frac{\mathbf{H}_y}{\omega_l\epsilon_0\epsilon_l(\omega_l)}\left(k_{2z}\hat{z} - k_x\hat{x}\right)exp\left(ik_x x + ik_{2z}z\right) \tag{2.76}$$

$$\mathbf{E}_s = \frac{\mathbf{H}_y}{\omega_s\epsilon_0\epsilon_s}\left(k_{1z}\hat{z} - k_x\hat{x}\right)exp\left(ik_x x + ik_{1z}z\right). \tag{2.77}$$

The polar phonons generated by laser-induced plasmons evanescence into the silicon. The coherent optical phonon displacement can be calculated by solving Equation 2.68 with Equation 2.72 and Equation 2.73 as following [33]:

$$Q(z>0, t>0) = Q_0 e^{-\gamma(t-zn/c)}\sin\left[\omega_0(t-zn/c)\right],$$

where

$$Q_0 = 2\pi I N \alpha' e^{-\omega_0^2 \tau_L^2/4}/\omega_0 nc,$$

where I is the magnitude of the triggering pulse, α' is the differential polarizability, τ_L is the pulse duration. The optical phonon displacement is plotted in Figure 14 for silicon inside the nanocavity in 140 fs laser pulse at 4.11×10^{15}Hz. For the given phonon displacement, the energy loss due to the emission of coherent optical phonons is given by [33]:

$$\begin{aligned} \Delta E = \frac{\Delta I}{I} &= -\frac{2\pi N \omega_0 l \left(\frac{\partial \alpha}{\partial R}\right) R_0'}{nc} \\ \text{where } R_0' &= \frac{4\pi I \left(\frac{\partial \alpha}{\partial R}\right)_0 e^{-\frac{\omega_0^2 \tau_L^2}{4}}}{\omega_0 nc}. \end{aligned}$$

We found that the energy loss due to the emission of coherent optical phonon in SiO_2 to be about 5 % of the plasmons, which is about 135 meV with 2.7 eV. Parameters used in the calculation are summarized in Table II. This indicates that almost every plasmon produces a coherent optical phonon at Si-SiO_2 interface: this mechanism could be a possible source of massive nonequilibrium phonon production which would lead to the second-order photon emission process in silicon.

2.3.3 Local Density of State Analysis on Plasmon-Phonon interaction

FDTD simulation similar to Section 2.1.4 was performed to investigate the effect of polar SiO_2 interlayer. The result also shows that the location of dominant peaks in LDOS spectra for the structure with SiO_2 interlayer in Figure 15 are separated by an average of 150 meV, whereas those for the structure without SiO_2 interlayer are separated by an average of 100 meV.

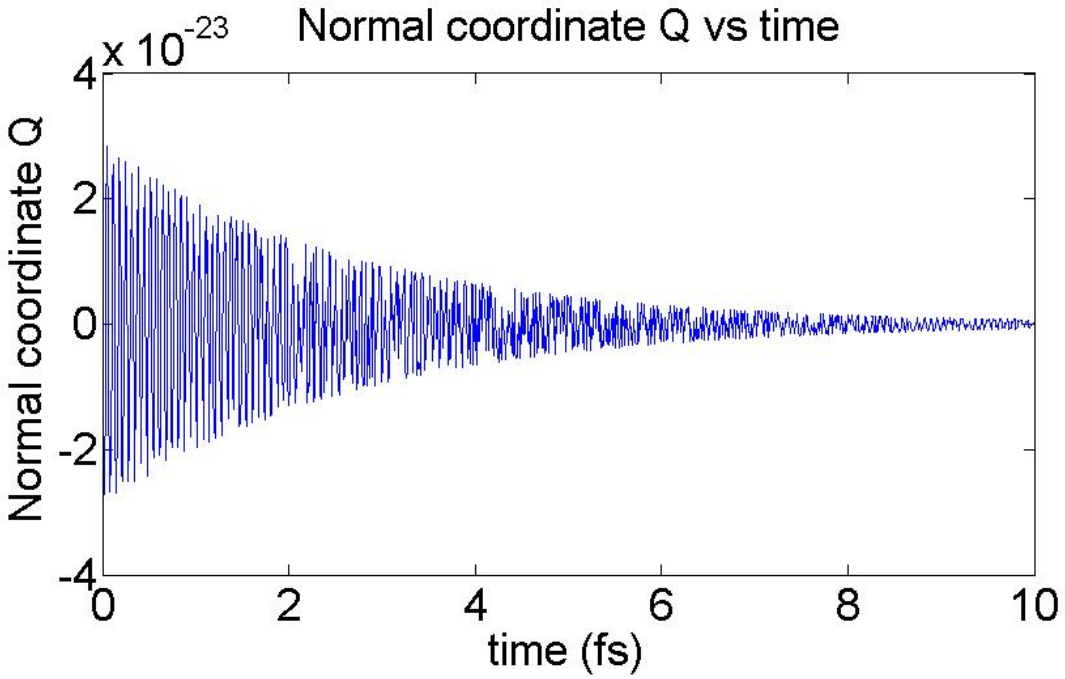

Figure 14: Coherent optical phonon displacement in silicon. ©2014 IEEE

This indicates that the SiO_2 interlayer affects the resonant mode inside the cavity. Moreover, the 150-meV separation of the modes may open the way to exploiting combined plamon and phonon modes in device applications since SiO_2 has a strong polar mode at 153 meV.

2.3.4 Scattering Rates of Electrons in Silicon with Interface Coherent Phonons in SiO_2

The electron-phonon scattering rates of SiO_2 can be calculated via following sets of equations: [31] For LO phonons

$$\gamma = \frac{e^2\omega}{\hbar\nu}\left(\frac{1}{\epsilon_\infty} - \frac{1}{\epsilon_0}\right)\left[(n_\omega + 1)\ln\left(W_2^+/W_1^+\right) + n_\omega \ln\left(W_2^+/W_1^+\right)\right] \tag{2.78}$$

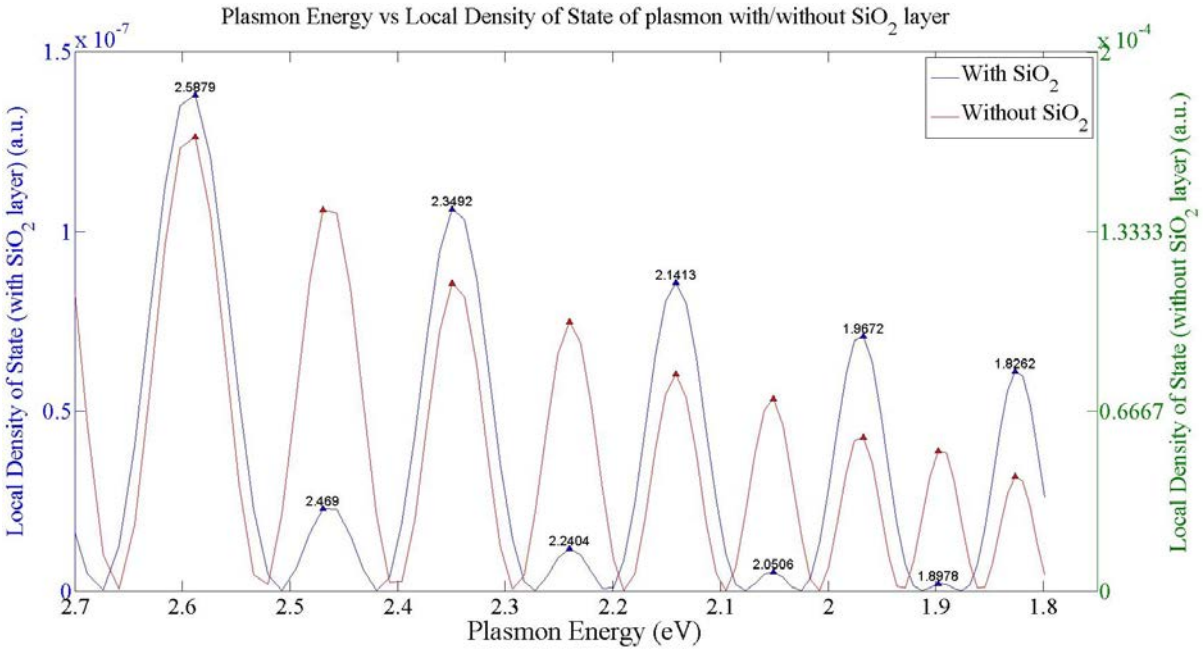

Figure 15: LDOS versus energy with TMz mode; comparison with the LDOS of the structure without SiO_2 interlayer. ©2014 IEEE

Parameter	SiO_2
Density of Oscillator	2.3×10^{22} atoms/cm^3
Amplitude of the field	7420 V/cm^2
Frequency of the field (ω)	6.52×10^2 THz
Refractive index	1.55181 at 4.11×10^2 THz
Pulse duration	50 fs
Damping constant	$0.37 \times \omega$ (ref. [33])
Scattering cross section	$2.8 \times 10^{-14} cm^2$

TABLE II: PARAMETERS USED TO CALCULATE THE ENERGY LOSS DUE TO THE EMISSION OF COHERENT OPTICAL PHONON IN SILICON DIOXIDE.

For acoustic phonons

$$\gamma^{\pm} = \frac{3|S|^2}{4\pi M_p N_c \hbar\nu} \int_0^{q^{\pm}_{max}} \frac{q^3}{\omega(q)} \left[n(q) + \frac{1}{2} \pm \frac{1}{2} f(q) \right] dq \tag{2.79}$$

where γ^+ is acoustic phonon emission and γ^- absorption.

Parameters used to calculate phonon-electron scattering can be obtained in Appendix B or in reference [31]. Figure 16 exhibits the calculated scattering rates. The results show that the scattering of LO phonons and electron is relatively high in visible region, which is an evidence

that an electron in a virtual state right after a photon absorption can absorb phonons to be excited to the conduction band.

2.4 Conclusion

In conclusion, Ag in 1D Si-SiO_2-Ag system can invoke SPP with a triggering pulse, which can carry both energy and momentum. The SPP is generally confined at the interfaces and absorbed by electrons in silicon. The energy and the momentum of SPP can be estimated using semiclassical approach and the amount of the power absorbed can also be estimated. The results show that the confinement of SPP is 5 nm, and it is indeed possible to excite electrons in the valence band of silicon to the conduction band with aid of SPP wavevector shifting by interface roughness. The results also show the qualitative agreement with the previous experimental results. In addition, the conventional second order process was supplemented by stimulated Raman scattering theory that would generate a massive number of coherent phonons with an assist of plasmons. The promising qualitative agreement with the experimental data was obtained which will lead to several future works.

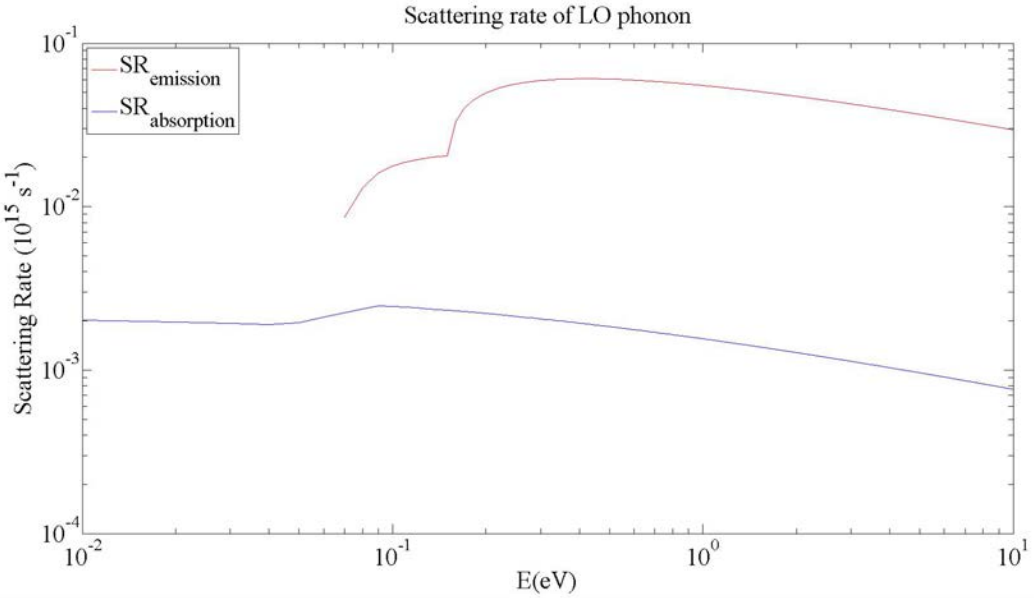

(a) LO phonon

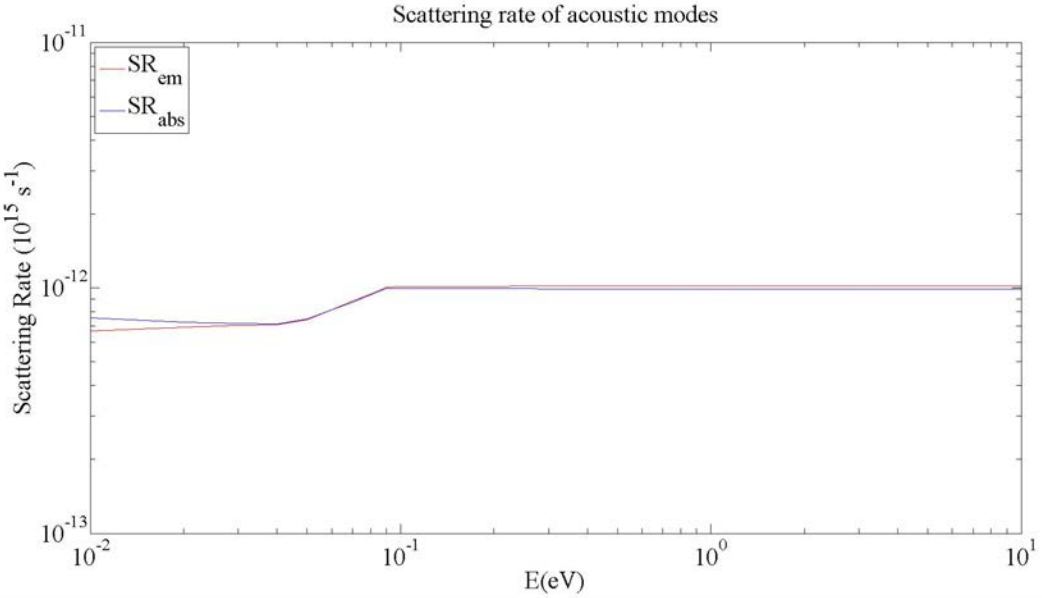

(b) Acoustic phonon

Figure 16: Scattering rate of phonon-electron in SiO_2 (a) LO phonon (b) Acoustic phonon

CHAPTER 3

NUMERICAL CALCULATIONS OF THE SCATTERING CROSS SECTION OF PLASMONIC NANODISKS

3.1 Introduction

Since Ritchie introduced energy loss by "the excitation of plasma oscillations or 'plasmons'" from thin metallic films [36] in 1957, plasmonics has emerged as a possible solution in many field of studies such as SERS, nonlinear optics, optoelectronics, and many more. [9,37–39] With the development of fabrication of metallic structures in nano-scale, it has become possible to precisely tune on the excitation of plasmons in plasmonic materials. [9] However, the plasmonic materials currently being used are mostly precious metals like gold and silver. In this work, the scattering cross section (SCS) of various sized nanodisks made of three non-precious metals, aluminum, nickel, and copper, are examined and compared to the result of silver.

3.2 Theory

3.2.1 Numerical computation of scattering cross section

One of the most interesting quantities regarding optical responses of metals is the SCS. With development of numerical analysis techniques, [12, 40–42] The SCS is in indicator of how much plasmons interact with the incident electromagnetic waves. While it is possible to calculate the SCS at each wavelength of electromagnetic waves in the interested range, it is more efficient to

---

[0]Parts of this thesis were reproduced with permission from ©2015 IEEE

apply the Fourier transform on a response spectrum to a short pulse to get the broad range spectra. [16] The scattered power spectrum of an object through a surface that encloses it is given by

$$P(\omega) = \mathbb{R} \oint_S (\mathbf{E}_\omega(\mathbf{r})^* \times \mathbf{H}_\omega(\mathbf{r})) \cdot d\mathbf{A}, \tag{3.1}$$

where $\mathbf{E}_\omega(\mathbf{r})$ and $\mathbf{H}_\omega(\mathbf{r})$ are computed by Fourier-transforming the time-dependent electric and the time-dependent magnetic field over all time:

$$\mathbf{E}_\omega(\mathbf{r}) = \frac{1}{\sqrt{2\pi}} \int e^{i\omega t} \mathbf{E}(\mathbf{r}, t) dt \tag{3.2}$$

$$\mathbf{H}_\omega(\mathbf{r}) = \frac{1}{\sqrt{2\pi}} \int e^{i\omega t} \mathbf{H}(\mathbf{r}, t) dt. \tag{3.3}$$

According to the conservation law, the incident power, $P_0(\omega)$ should be equal to the sum of the absorption, $P_{abs}(\omega)$, the scattering $P_{scat}(\omega)$, and the interaction between two $P_{int}(\omega)$, :

$$P_0(\omega) = P_{abs}(\omega) + P_{scat}(\omega) + P_{int}(\omega). \tag{3.4}$$

So, it is not possible to just subtract $P_{abs}(\omega)$ from $P_0(\omega)$ to get $P_{scat}(\omega)$. It makes much more sense to subtract the Fourier-transformed incident fields from that of the total field to achieve the goal. That is,

$$P_{scat}(\omega) = \mathbb{R} \oint_S ([\mathbf{E}_\omega(\mathbf{r}) - \mathbf{E}_{\omega,0}(\mathbf{r})]^* \times [\mathbf{H}_\omega(\mathbf{r}) - \mathbf{H}_{\omega,0}(\mathbf{r})]) \cdot d\mathbf{A}. \tag{3.5}$$

The scattering cross section, C_{scat}, can be obtained by taking the ratio of $P_{scat}(\omega)$ to the incident irradiance, I_0:

$$C_{scat} = \frac{P_{scat}(\omega)}{I_0}. \tag{3.6}$$

3.3 Method

An open source Finite-Domain Time-Different method simulaiton code, MEEP [16], is used for all calculations. A Gaussian source with the central frequency at 355 nm is placed near nanodisks of Ag, Al, Ni and Cu with diameters from 70 nm to 160 nm in 10 nm increments enclosed by the Perfect Matching Layers (PML) [9] for excitation. The Drude-Lorentz model is used to describe the polarizability of the metals. The calculation is done in two steps; first, the source is placed in an open region enclosed by PML, and the electric field flux is calculated at each time step to get the incident $\mathbf{E}(\mathbf{r}, t)$ and $\mathbf{H}(\mathbf{r}, t)$. Then, in step 2, the electric field flux is calculated with metallic nanodisks placed and the scattered power, $P_{scat}(\omega)$, is calculated based on the open-region-field-flux calculated in the previous step. All computations are performed on a PC with a quad core at 3.0 GHz CPU and 6 GB RAM.

3.4 Results and discussion

Overall, all three metals show the same red-shift pattern as the diameter increases as shown in Figure 2. Unlike the Ag nanodisk, which tends to present the highest SCS in the ultraviolet

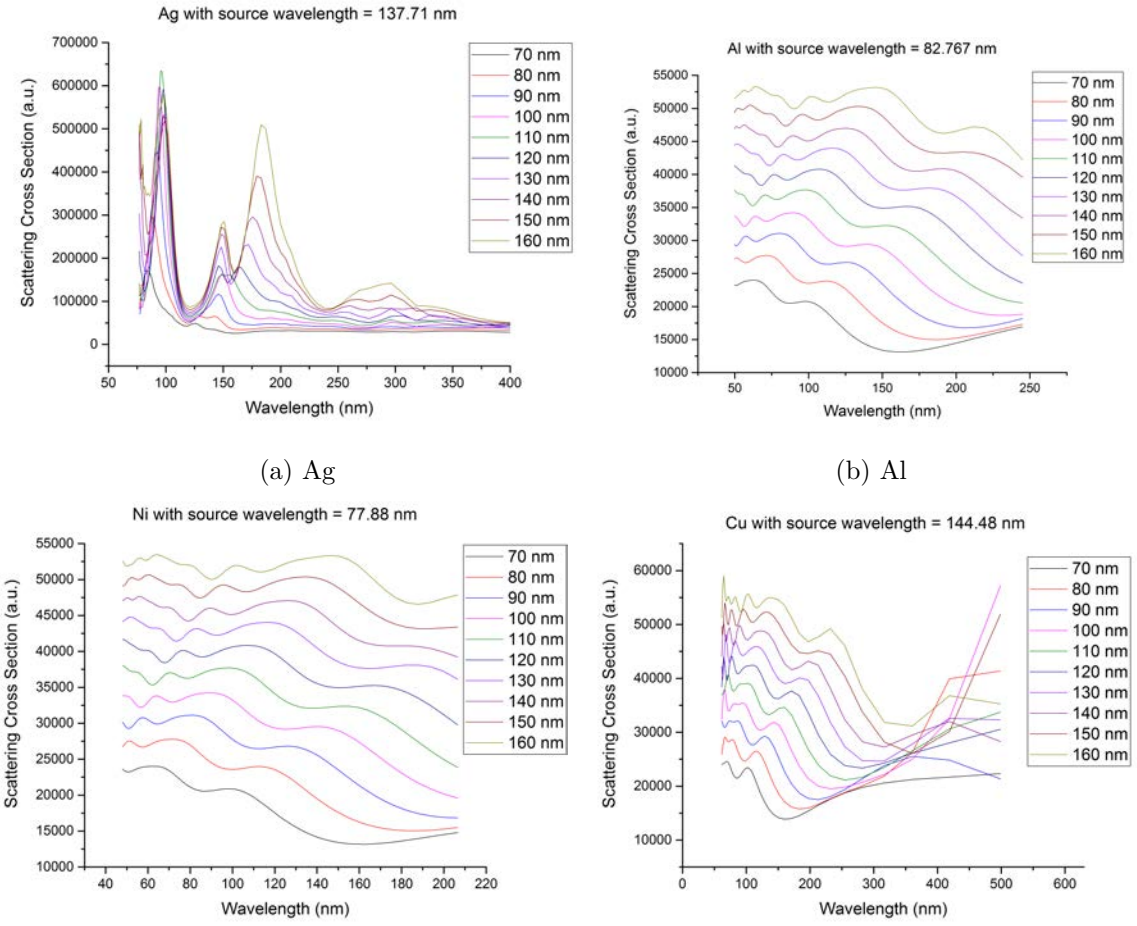

(a) Ag

(b) Al

(c) Ni

(d) Cu

Figure 17: Scattering cross section as a function of light frequency for (a) Ag, (b) Al, (c) Cu, and (d) Ni nanodisks with diameters from 70 nm to 160 nm with sources at plasma frequencies of each metal.

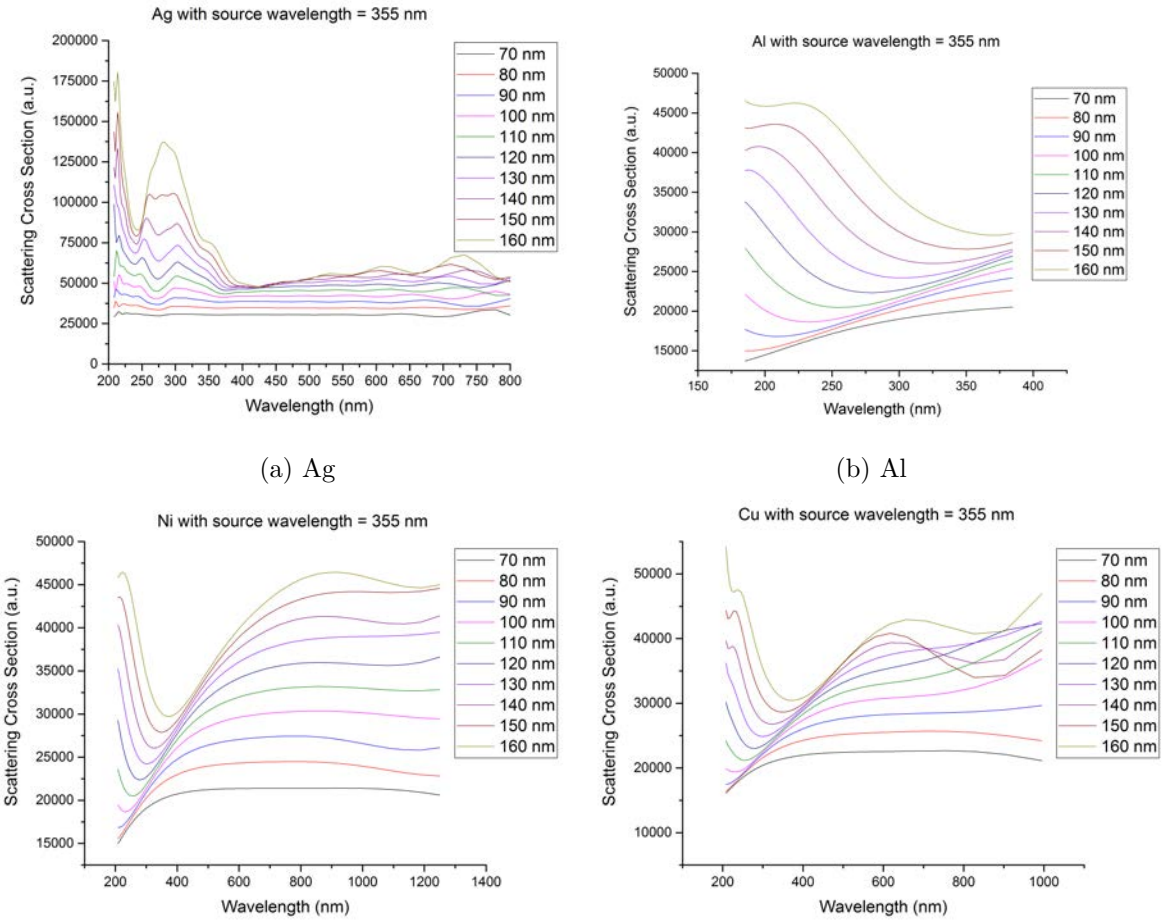

(a) Ag (b) Al

(c) Ni (d) Cu

Figure 18: Scattering cross section as a function of light frequency for (a) Ag, (b) Al, (c) Cu, and (d) Ni nanodisks with diameters from 70 nm to 160 nm with the source wavelength of 355 nm (visible source). In the visible range (300 nm - 800 nm), the amplitude of SCS of nonprecious metals are comparable to that of silver.

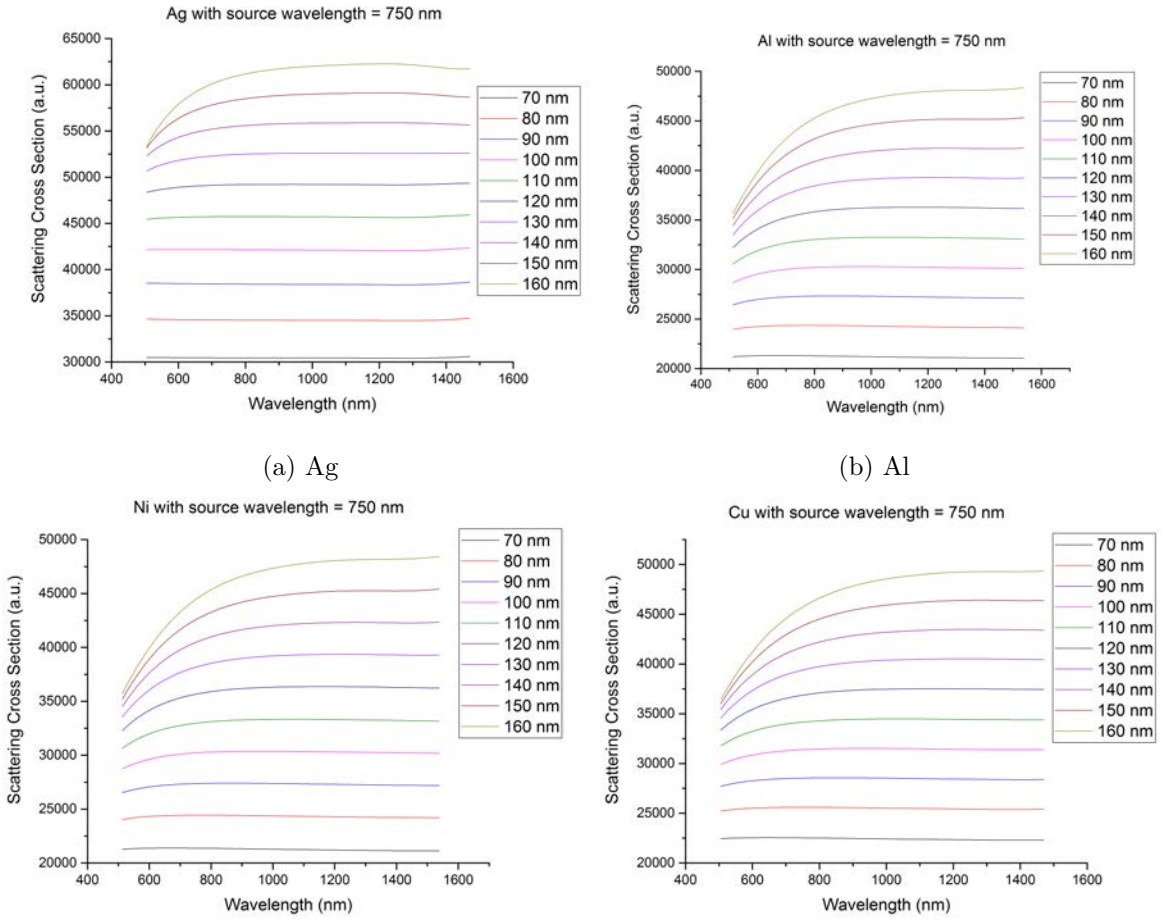

(a) Ag (b) Al

(c) Ni (d) Cu

Figure 19: Scattering cross section as a function of light frequency for (a) Ag, (b) Al, (c) Cu, and (d) Ni nanodisks with diameters from 70 nm to 160 nm with the source wavelength of 750 nm (infrared source).

range, Al, Ni, and Cu nanodisks exibit the high SCS throughout the visible region. Also amplitudes of the SCS of the Al, Ni, and Cu nanodisks ($\approx 2.2 \times 10^4$ atomic units for 70-nm-diameter nanodisks) are comparable with the Ag nanodisk ($\approx 3 \times 10^4$ atomic units). These results can lead to a conclusion that non-precious metals such as aluminum, nickel, and copper can be used as an alternative to silver without sacrifying the efficiency in the visible range.

CHAPTER 4

CONTROLLING THE IONIC CURRENTS BY MODIFYING MEMBRANE POTENTIAL NEAR ION CHANNELS IN CATFISH HORIZONTAL RETINA CELLS WITH QUANTUM DOTS

4.1 Background

Cellular ion currents in excitable cells, such as neurons and muscle cells, are essential for the function of living organisms, as they allow the cells to communicate. These ion currents are possible due to an electrochemical gradient created by varying concentrations of ions inside and outside of the cell. K^+ is approximately 30 times more concentrated intracellularly than extracellularly, while Na^+ is approximately 10 times more concentrated extracellularly than intracellularly. This is primarily due to the Na^+/K^+ pump, which uses energy to transport 3 Na^+ ions out of the cell for every 2 K^+ ions into the cell. In addition, K^+ is allowed to passively flow through leak channels. The unequal ion concentrations inside and outside the cell result in two opposing gradients a concentration gradient and an electrical gradient. At equilibrium, when these two forces negate each other, the electric potential across the membrane is typically around -70 mV, known as the resting membrane potential. [43] Because the cell membrane is comprised of a hydrophobic lipid bilayer, hydrophilic particles like ions cannot pass directly through the membrane and instead must rely on a variety of channels. In addition to the K^+ leak channels mentioned above, which open and close randomly, several other types of ion channels

exist. Ligand-gated ion channels open upon binding to a specific receptor. Glutamate-gated channels, for instance, open when bound to the neurotransmitter glutamate and play a major role in excitatory signaling in the brain. [44] Mechanically activated channels exist in the inner ear and open in response to sound waves. [43] This study focuses on voltage-gated ion channels, which open in response to changes in membrane potential. Retinal horizontal cells are neuronal cells found in the retina that are responsible for enhancing visual contrast [45]. Horizontal cells from channel catfish retina were used in this study due to their large flat morphology, which makes them ideal for whole cell patch clamp recordings. [46] These cells display six types of ion currents. Na^+ current is activated in response to membrane depolarization. Its threshold is around -50 mV, at which point channels begin to open and Na^+ flows into the cell. This creates a positive feedback loop, further depolarizing the membrane. An L-type Ca^{2+} current, which activates at around -30 mV, also flows into the cell and contributes to membrane depolarization. Whereas Na^+ conductance only lasts several milliseconds, [47] Ca^{2+} current can last for around 100 ms, though it is small in magnitude compared to Na^+ current. [48] Several K^+ currents are responsible for repolarizing the membrane. Transient outward K^+ current is rapidly activated and consists of K^+ moving out of the cell during membrane repolarization. Delayed rectifying K^+ channels open slowly and play a large role in repolarization by enabling K^+ flow out of the cell to the point where the membrane is hyperpolarized. Anomalous rectifying K^+ current is activated by hyperpolarization and consists of K^+ flowing into the cell to bring the membrane voltage back to resting potential. [43, 49] Leak currents are not voltage dependent and simply operate according to Ohms law to maintain resting membrane potential. A number

of studies have been done on factors that can affect the activation voltage of voltage-gated ion channels, [50–53] since the ability to influence the activation dynamics could have potential applications for a variety of diseases affecting voltage-gated ion channels, such as epilepsy or cardiac arrhythmia. [54] In this work, TiO_2 nanoparticles, or quantum dots (QDs), are used in conjunction with retinal horizontal cells to study the effects of light-induced electric field on the behavior of voltage-gated ion channels. Previous theoretical work has postulated on semiconductor QDs ability to influence voltage-gated ion channels with their polarization. [55,56]. It has been shown that neurons grown on HgTe nanoparticle-containing films experience action potentials when irradiated with UV light. [57] CdS QDs have also been shown to cause ion channel activation when excited optically. [58] Since TiO_2 is biocompatible, it would make an even better candidate for use with living cells than QDs containing heavy metals.

4.2 Methods

4.2.1 Cell Culture

Channel catfish were obtained from Keystone Hatcheries (Richmond, IL) and from Wing Lee Co. (Chicago, IL). Fish were dark adapted for at least an hour before use, anesthetized with a solution of approximately 1 g/gallon of ethyl 3-aminobenzoate methanesulfonate (Sigma Aldrich, St. Louis, MO) and 2.5 g/gallon of sodium bicarbonate (Sigma Aldrich, St. Louis, MO), and sacrificed by cervical transection and pithing. Retinal horizontal cells were obtained with previously described protocols. [59, 60] Both eyes were removed, sliced in half, and the posterior half was immersed in a solution containing approximately 1 mg/mL papain (Acros Organics, Fair Lawn, NJ) and 0.5 mg/mL L-cysteine (Sigma Aldrich, St. Louis, MO). After

30 min, retinas were removed and rinsed 8 times in Ringers solution containing 126 mM NaCl, 4 mM KCl, 3 mM $CaCl_2$, 1 mM $MgCl_2$, 15 mM dextrose, and 10 mM HEPES, pH 7.4. The retinas were then dissociated by gentle agitation with a glass pipette. After around 15 seconds of agitation, the supernatant, containing primarily photoreceptors, was removed and discarded. The remainder of the retinas, containing primarily horizontal cells, was agitated for an additional 30 seconds. The resulting suspension was placed in 35-mm cell culture dishes containing 4 mL of Ringers solution (approximately 2 drops of suspension per dish). The dishes were kept at 14^oC until use and recordings were obtained on the same day.

4.2.2 Whole Cell Patch Clamp Recordings

Whole cell patch clamp recordings were obtained using a HEKA EPC 10 USB amplifier (Holliston, MA). Glass capillaries (Sutter Instruments, Novato, CA) were pulled to form pipettes with resistances of 4-8 $M\Omega$ and filled with intracellular solution containing 110 mM KCl, 0.5 mM $CaCl_2$, 5 mM EGTA, and 10 mM HEPES. The pH was adjusted to 7.0 using KOH. Once the pipette was brought into contact with the cell, suction was applied to create a gigaohm seal and rupture the membrane. For recordings obtained with TiO_2, 140 mM TiO_2 QDs (Sigma Aldrich, St. Louis, MO) were added to the dish after successful formation of the gigaohm seal. A 325-nm and 442-nm dual wavelength 100-mW IK Series He-Cd Laser (Kimmon Electric Company, Tokyo, Japan) was shined on the cell to excite the TiO_2 QDs (Figure 20). Voltage pulses from -110 mV to 60 mV, each lasting 200 ms, were applied sequentially and the resulting current readings were recorded using HEKA Patchmaster acquisition software. When voltage-gated currents begin to flow through the membrane, the amplifier applies an equal and opposite

current necessary to maintain the cell at the set voltage. Voltage-activated ion currents can thus be measured. Recordings were obtained with and without laser excitation, and the minimum current during the first 15 ms was used to plot I-V curves, since the maximum inward current due to Na^+ conductance occurs during this time period. A total of 12 different data sets were obtained from different cells. In addition, 12 control trials were performed in the absence of TiO_2 to confirm that any change in channel conductance was not caused by UV light itself.

4.2.3 Extended Hodgkin and Huxley model

Hodgkin and Huxley proposed an electrical circuit model (HH model) of a cell membrane from a squid axon with two different types of voltage-gated ion channels in 1952. [47] In the HH model, current from an individual ion channel is described by equation with the membrane potential and a set of first order differential equations which can be empirically fitted well with the experimental data. That is,

$$I_i = g_i^{max} \cdot m_n(V,t) \cdot h_p(V,t) \cdot (V - E_i) \tag{4.1}$$

where i is the type of ion channel, E_i is the reverse potential of i type of ion channel, $m_n(V,t)$ and $h_p(V,t)$ are activation and inactivation constants, respectively, and n and p are power constants. These constants are given by:

$$\frac{dm_i}{dt} = \alpha_{m_i}(V) \times (1 - m_i(t)) - \beta_{m_i}(V) \times m_i(t) \tag{4.2}$$

$$\frac{dh_i}{dt} = \alpha_{h_i}(V) \times (1 - h_i(t)) - \beta_{h_i}(V) \times h_i(t) \tag{4.3}$$

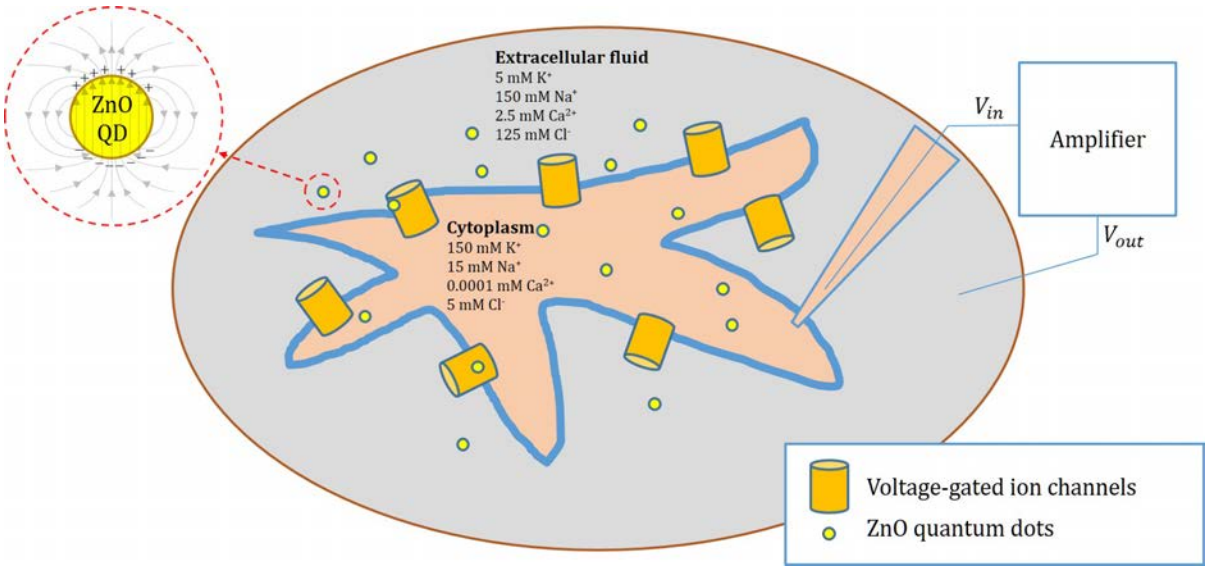

Figure 20: Schematic of whole cell patch clamp recordings performed in this study. EGTA in the intracellular fluid serves as a Ca^{2+} chelator, effectively making the free Ca^{2+} concentration in M range. A gigaohm seal is created by bringing the electrode-containing glass capillary to the cell membrane and applying suction until the membrane inside the pipette is ruptured. The membrane can then be maintained at a set voltage point (Vcmd) through a current generated by the amplifier.

	α_m	β_m	α_h	β_h
Transient outward K^+ current [61,62]	$\frac{24}{1+e^{-\frac{V-50}{28}}}$	$8e^{-\frac{V}{36}}$	$0.5e^{-\frac{V}{60}}$	$\frac{0.4}{1+e^{-\frac{V+40}{5}}}$
Delayed rectifying K^+ current [61–63]	$\frac{4(65-V)}{e^{\frac{65-V}{50}}-1}$	$48e^{-\frac{45-V}{85}}$	$\frac{30}{1+e^{\frac{V+92}{7}}}$	$\frac{16}{1+e^{\frac{V+100}{15}}}$
Anomalous rectifying K^+ current [61, 62]	$m_{Ka}=\frac{1}{1+e^{\frac{V+60}{12}}}$			
Ca^{2+} [63]	$\frac{5(70-V)}{e^{\frac{70-V}{28}}-1}$	$2e^{\frac{-V}{15}}$	$h_{Ca}=\frac{[K]}{[K]+[Ca]_{out}}$	
Na^+ current [61]	$\frac{20(38-V)}{e^{\frac{38-V}{25}}-1}$	$200e^{-\frac{55+V}{18}}$	$1.0e^{-\frac{80+V}{8}}$	$\frac{0.8}{1+e^{\frac{80-V}{75}}}$
Leakage current [47,61]				

	$g_{max}[nS]$	$E_i[mV]$	I_{ion}
Transient outward K^+ current [61,62]	3.0	-80	$g_{Kv}m_{Kv}^3h_{Kv}(V-E_{Kv})$
Delayed rectifying K^+ current [61–63]	22.0	-80	$g_Am_A^4h_A(V-E_A)$
Anomalous rectifying K^+ current [61, 62]	4.5	-80	$g_{Ka}m_{Ka}^5(V-E_{Ka})$
Ca^{2+} current [63]	30.0	$12.9\log\frac{[Ca]_{in}}{[Ca]_{out}}$	$g_{Ca}m_{Ca}^4h_{Ca}(V-E_{Ca})$
Na^+ current [61]	5.0	55	$g_{Na}m_{Na}^3h_{Na}(V-E_{Na})$
Leakage current [47,61]	0.5	-80	$g_i(V-E_i)$

TABLE III: SUMMARY OF THE PARAMETERS FOR HH MODEL USED.

where αs and βs are empirical parameters that are tunable to designated behavior of ion channels. The parameters used in this work are summarized in Table III. The total ionic current in a cell is given by the sum of currents from all individual ion channels plus the capacitive current due to the change of the membrane potential in time:

$$I_{ion}^{total} = C_{membrane}\frac{dV}{dt} + \sum_i I_i(V,t) \tag{4.4}$$

With the presence of a QD that produces electrostatic field, Equation 4.4 becomes

$$I_{ion}^{total} = C_{membrane}\frac{dV}{dt} + \sum_i I_i(V + V_{QD},t) \tag{4.5}$$

To model the electric field from TiO_2 QDs, a QD is assumed to be a sphere. When it is in an intense laser field, electron and hole pairs are created. As a result, it is polarized uniformly along the polarization direction of the laser. This phenomena is referred to as induced polarization, which is mathematically described by

$$\overrightarrow{P} = \alpha\overrightarrow{E} \tag{4.6}$$

where $\alpha = \left(1 - \frac{\sqrt{E_g}}{4.06}\right)\frac{M}{\rho} \times 4.4060 \times 10^{-35} F \cdot m^2$ (Hodgkin and Huxley 1952), $\overrightarrow{E}$ is the laser field, E_g is the band gap of QD, M is the molecular weight of QD, ρ is the density of QD. Then the surface charge σ is calculated by

$$\sigma = \overrightarrow{P} \cdot \hat{n} = P \cdot \cos(\theta) \tag{4.7}$$

The laser field is calculated from the intensity of laser used in the experiment, the total power of which is 100 mW, by the relationship between the time average of energy density of laser and the amplitude of electric field which is given by

$$|E|^2 = \frac{2I}{cn\epsilon_0} \tag{4.8}$$

where I is the intensity per unit area, c is the speed of light, n is the refractive index of the media, and ϵ_0 is vacuum permittivity. Then, the electric field produced from a TiO_2 QD can be calculated by solving Gausss law: [64]

$$E_{QD}^{induced} = \frac{P_{induced}}{3\epsilon}\frac{R^3}{r^3}\left[2\cos(\theta)\hat{r} + \sin(\theta)\hat{\theta}\right], r > R \tag{4.9}$$

where ϵ is the dielectric function of the surrounding media and R is radius of a QD. In water-based electrolytes, the screening effect has to be considered as an exponential decay:

$$E_{QD}^{electrolyte} = E_{QD}^{induced} \cdot e^{-(r-R)/\lambda_D} \tag{4.10}$$

λ_D is the Debye length of the electrolyte which can be written by

$$\lambda_D = \sqrt{\frac{\epsilon k_b T}{2N_A e^2 I}} \tag{4.11}$$

where k_B is Boltzmann constant, T is temperature, N_A is Avogadros number, e is elementary charge, and I is ionic strength of the electrolyte, which is given by $I = \frac{1}{2}\sum_{i=1}^{n} c_i z_i^2$, and c_i is the molar concentration of the ith ion in the electrolyte and z_i is the charge of the ith ion.

4.3 Results and Discussion

A typical whole cell voltage clamp recording is shown in Figure 21. For applied voltages below -70 mV, there is net negative current, or an influx of positive ions into the cell. This inward current is caused primarily by inwardly rectifying K^+ channels that are activated by hyperpolarizating voltages. At resting membrane potential (around -70 mV), the cell is at equilibrium and there is no net current flow. At voltages of -50 through 0 mV, voltage-gated activation of Na^+ channels can be seen as Na^+ rapidly flows into the cell due to the high concentration gradient, resulting in a large negative current which is represented by the green trace corresponding to V=0 mV in the inset of Figure 21a. Voltage-gated K^+ channels are also opening at this time, but the Na^+ conductance dominates, which explains the net negative current. At membrane potentials of greater than 30 mV, K^+ currents dominate; current flow through Na^+ channels is small near the Nernst equilibrium potential for Na^+, so the net current is positive. [43,65] The large spikes of positive or negative current at the beginning and end of the voltage pulse are capacitive currents caused by rearrangement of charges at the membrane, [65] and they can be ignored for the purposes of this experiment.

Out of the 12 recordings made in the presence of TiO_2, 6 showed a noticeable shift in the voltage associated with maximum Na^+ conductance, as shown in a representative plot in Figure 22a, which is consistent with the Hodgkin-Huxley model discussed in the previous section. In all cases, it is difficult to ensure that the quantum dot distribution near the cell membrane is sufficient to shift the voltage associated with maximum Na^+ conductance, so null results are to be expected in some percentage of the cases studied. Whereas the maximum inward current

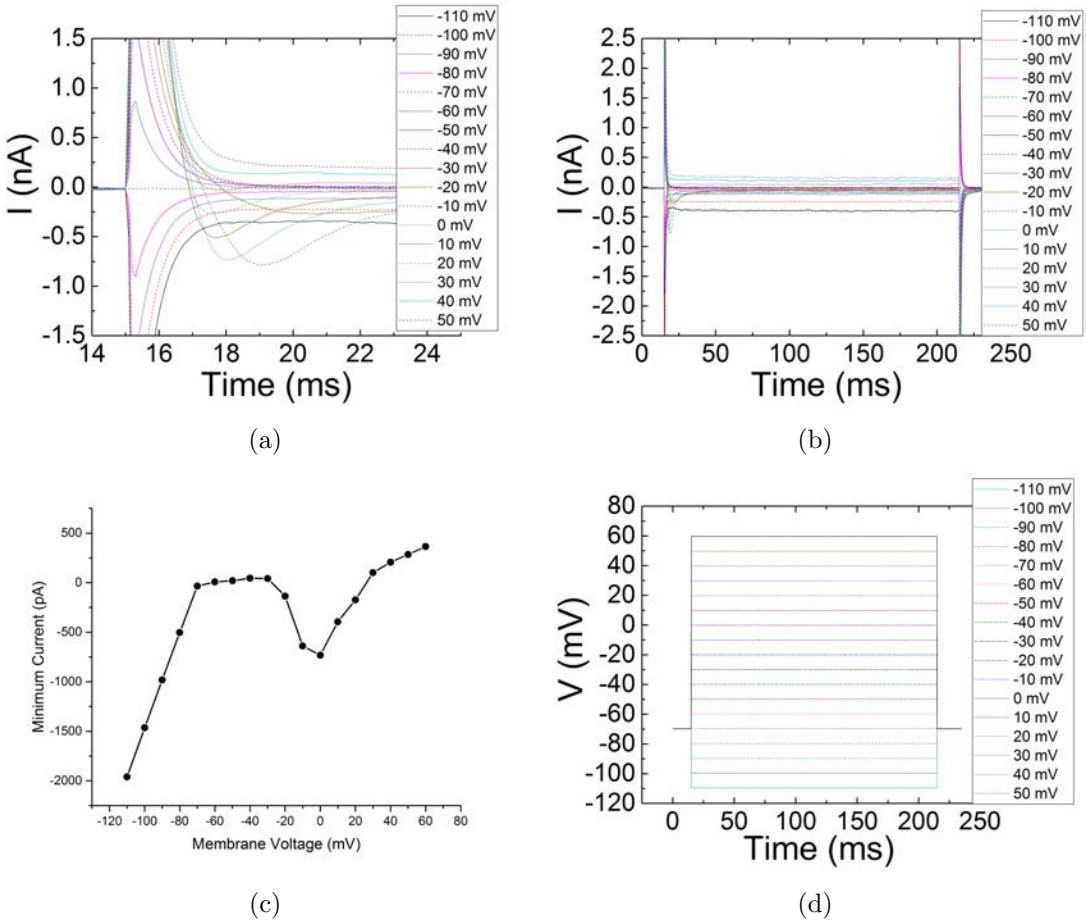

Figure 21: Typical whole cell voltage clamp recordings. A series of 200-ms voltage pulses from -110 to +60 mV in magnitude are applied sequentially (a). The corresponding current traces are recorded (b). The initial portion contained within the red rectangle is enlarged (c) to better examine the voltage-activated Na^+ currents and the subsequent repolarizing K^+ currents which dominate the membrane conductance in this range. The minimum current readings from the 15-25 ms range are plotted against the applied voltage to obtain an I-V curve (d).

occurred at around 0 mV prior to laser UV excitation, with laser excitation it shifted in the negative direction to around -10 mV. This shift was not observed in the control experiments performed in the absence of TiO_2 (Figure 22b). It is clear that the presence of both TiO_2 and UV light is necessary for the shift to occur, suggesting that it occurs due to the optical excitation and resulting polarization of TiO_2.

A shift in cellular activation voltage similar to one observed in this work has been previously reported in response to a variety of factors. It has been shown that protonation enhances Na^+ conductance [51] and Ca^{2+} conductance [52] in retinal horizontal cells, resulting in a shift in voltage associated with maximum inward current. This is likely due in part to H+ screening the negative charges near the membrane, with the resulting change in electrochemical gradient leading to a shift in activation potential. [66] Similarly, studies involving mutant K^+ channels which were missing either the N or C terminus of the channel showed in a shift in activation voltage. [50] While the exact mechanism of modulation of many voltage-gated channels is still under debate, it is largely believed that the voltage sensing occurs due to reorientation of positively and negatively charged subunits of the ion channel in response to potential changes, resulting in opening or closing of the channel. [65] It, therefore, is reasonable that the presence of protons or the absence of a charged terminus would cause a change in the channels conductance. In our case, the electric fields from optically-excited TiO_2 affect the channels in a similar manner by introducing an induced electrostatic potential, altering the orientation of the charged subunits and causing the channel to open or close. The distance between the QD and the ion channel plays a large role in this phenomenon. The strength of the

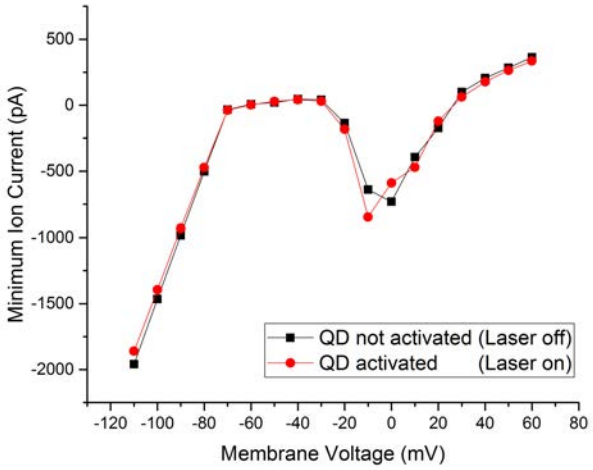

(a)

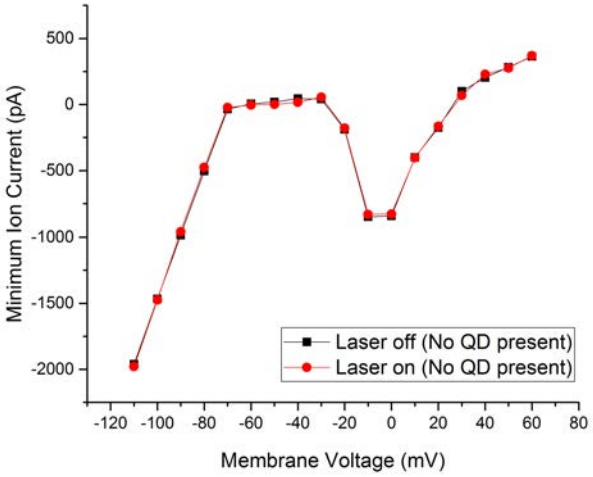

(b)

Figure 22: Representative I-V plots obtained from whole cell recordings in the presence (a) and absence (b) of TiO_2. Black traces were obtained with the laser off and red with the laser on. A shift in the voltage associated with the maximum Na^+ conductance can be seen in the presence of UV-excited TiO_2. This trend was observed in 6 out of the 12 cells tested.

electric field generated by polarized TiO_2 decreases exponentially with distance due to screening by the electrolyte, [64] in this case the Ringers solution, so it is imperative for the TiO_2 to be in close proximity to the ion channel in order for the voltage shift to occur. This may explain why 6 out of 12 cells did not show the activation voltage shift observed in the other half of the cells tested.

Our simulation shows that in retinal horizontal cells the addition of an excited TiO_2 QD results in a left shift of the I-V characteristics along the voltage axis, in the case when the polarization axis of the QD is perpendicular to the membrane and the QD is 1 nm away from the ion channel based on HH model described earlier. (See ref. [67] for an example HH simulation code) In Figure 23, I-V characteristics of a horizontal cell are plotted which represent the total ion currents in response to the applied membrane potential. Inset of Figure 23 represents the magnification near the local minima where Na^+ channels play the major role. The voltage associated with the minimum current is shifted to the left in the presence of the excited QD compared to without QD. The shifts of I-V characteristics also appear in case of individual ion channels, as shown in Figure 24. For each ion channel, the I-V curves shifted to the left in the range that the specific channel is activated with addition of QD. For example, the activation range of the voltage gated anomalous rectifying K^+ channel is below potentials of -40 mV, [68] and there is a clear shift of I-V characteristics to the left in this range. The behavior of individual ion currents (Figure 24) in the presence of QD can be used to explain the trends observed experimentally (Figure 22). The minor left-shift in I-V curve observed experimentally in the -110 mV to -70 mV range can be attributed to anomalous rectifying K^+ channels. The

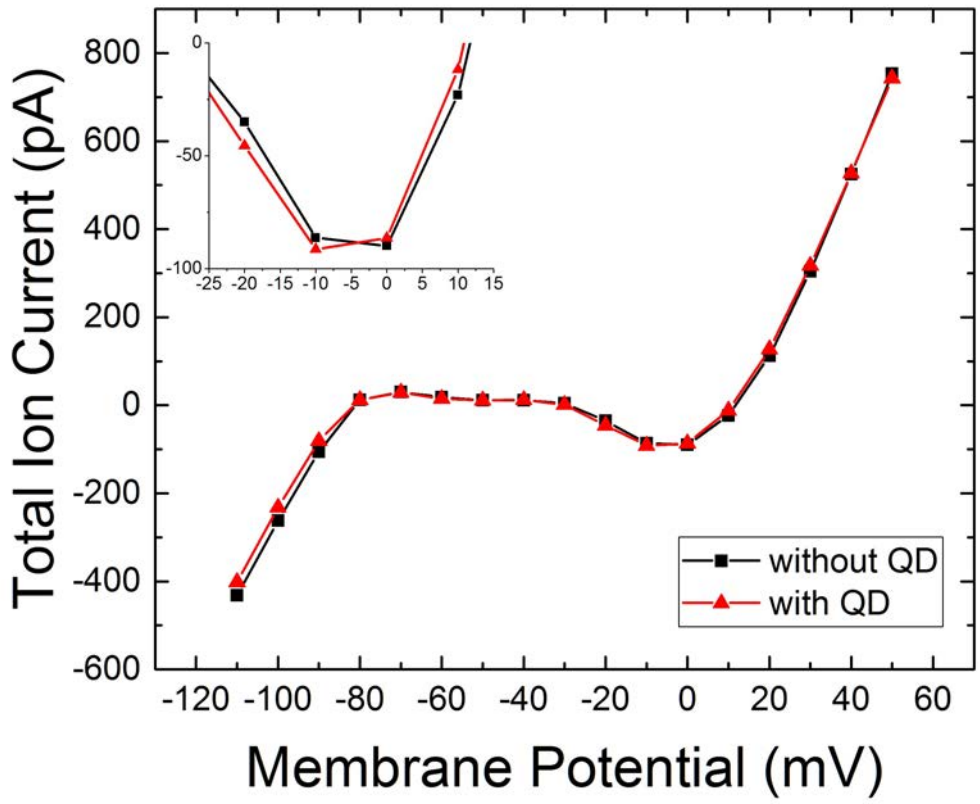

Figure 23: characteristics of a horizontal cell, which represent the total ion currents in response to the applied membrane potentials. The minimum point with QD is shifted to the left compared to that without QD.

shift in the I-V curve in -40 mV to +20 mV range is due to voltage-gated Na^+ and Ca^{2+} channels, the conductances of which dominate in this range. Since these trends were observed in 6 of the 12 cells tested, it is likely that in the other half of the cells the QDs were more than 1 nm away from the voltage-gated ion channels, resulting in strong screening of electric fields.

Although this simulation is specific to retinal horizontal cells, the parameters can be easily adjusted to predict the behaviors of other cell types in response to induced electric fields or other external stimuli. This is potentially relevant in medical applications for treatment of ion-channel related diseases.

4.4 Conclusion

In this work, optically-excited TiO_2 QD are shown to influence the opening of voltage-gated ion channels in retinal horizontal cells by shifting the cells I-V characteristics to more negative voltage values. This trend is especially strong in the physiologically relevant region of -30 mV to +40 mV, where voltage-gated Na^+ and K^+ channels display the highest conductance. Theoretical modeling confirmed that this is due to the electric fields generated by optically-excited TiO_2 QDs located within 1 nm of the ion channels. As in the case of Pappas et al., [57] the present studies support the conclusion that the illuminated QDs in close proximity to cellular membranes containing ion channels can modify the ion channel I-V curves. In the present work, the QDs were illuminated with UV radiation whereas in the previous studies of Pappas et al., infrared radiation was used to polarize the QDs. Together, these studies indicate that modified ion-channel characteristics may be realized under a range of illuminating wavelengths. These results have potential applications for studies of diseases affecting voltage-gated ion channels.

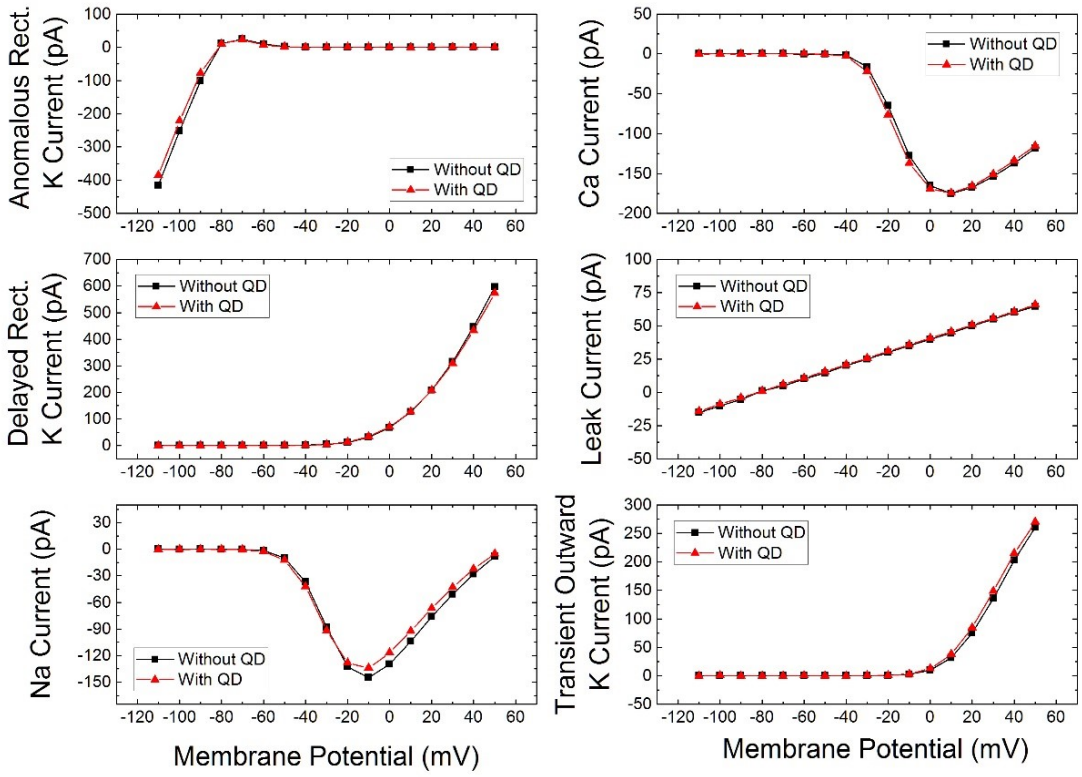

Figure 24: I-V characteristics of individual ion channels in a horizontal cell. For each ion channel, the I-V curves shifted to the left in the range that the specific channel is activated with addition of QD.

Moreover, these results indicate that it may be possible to modify or control the physiological behavior of cellular and neuronal ion channels, potentially opening the way to modifying ion channel behaviors in ways that impact cellular and neuronal functions in both diseased and healthy cells.

CHAPTER 5

OPTICAL, STRUCTURAL, ELECTROSTATIC PROPERTIES OF ZNO QUANTUM DOTS

5.1 Introduction

ZnO is an inorganic material with a multitude of environmental, industrial, and pharmacological applications, due to its favorable properties such as high chemical, mechanical, and thermal stability, wide energy band gap, strong luminescence, and biocompatibility. [70] For instance, it is a widely-used in the rubber industry as an additive due to its thermal properties, [71] in the textile industry due to its protective ultraviolet-absorbing quality, [72] in the electronics industry due to its wide band gap and strong bond energy, [73, 74] and in cosmetics and pharmaceutics due to antibacterial properties and ability to absorb ultraviolet (UV) radiation. [75] ZnO can exist in a variety of structures, including rods, spheres, and sheets, and can be synthesized using a variety of methods depending on the desired structure and application. This work will focus on ZnO nanoparticles, or quantum dots (QDs). One of the properties that make ZnO QDs very interesting is their spontaneous polarizability. [76] Wurtzite structures composed of two different kinds of atoms like ZnO QDs, which consist of alternating layers of different charges, tend to have the spontaneous polarization along the growth axis, namely

---

[0]Parts of this chapter were reproduced with permission from J. Appl. Phys. 118, 194304 (2015). Copyright 2015, AIP Publishing LLC [69]

c-axis. [77] Unlike induced polarization due to the external electric field, the spontaneous polarization leads to a very large built-in electrostatic potentials. This unique property opens up the possibilities of various applications in electronics, optoelectronics, biological sciences, etc. [55, 56, 78] However, a direct measurement of the electrostatic field due to the spontaneous polarization of ZnO QDs has not been reported yet due to their high mobility. Electrostatic force microscopy (EFM), the method used in this work to measure electrostatic fields of ZnO, relies on the probe first scanning the sample in contact mode to obtain a height profile, followed by a lift mode scan a set distance above the sample surface. Any force-induced change in probe oscillation in lift mode can thus be attributed to features of the sample, and it is therefore imperative that the QDs not be moved by the probe during the contract scan. Immobility is highly desired in scanning probe microscopy, [79] as demonstrated by efforts to immobilize samples via various methods, such as cryogenic freezing, [80] coating the substrate with gelatin, [81] or covalently binding samples to substrate. [79] Immobilizing colloidal nanoparticles has an added advantage of preventing aggregating upon drying.

In effort of immobilize nanoparticles, we used a simple layer-by-layer (LBL) synthesis technique. Developed in 1990s, LBL synthesis involves polyelectrolyte films which are formed when a positively charged substrate is exposed to an aqueous solution of polyanions, followed by rinsing and exposure to an aqueous solution of polycations. [82] The strong electrostatic attraction between opposite charges results in absorption of molecules to the surface, and strong electrostatic repulsion between same charges limits the absorbed molecules to only a single layer. The steps can be repeated as many times as needed to create nanoscale multilayer films [83] with

a variety of biomedical applications, such as drug delivery, coatings for implants, and surfaces for cell adhesion. [84] Charged nanoparticles can be used in place of one of the polyelectrolytes in order to form nanoparticle-polyelectrolyte films. [85] Multi-material composites are useful in a wide variety of scientific disciplines, as they allow one to take advantage of both materials desirable characteristics. In this work, we successfully synthesized and characterized optical and structural properties of ZnO QDs. We show here that ZnO can be successfully integrated into an LBL film, and the resulting layer of ZnO immobilized on a polymer surface makes it easier to study ZnO using AFM, [86] EFM, or other techniques where any movement is detrimental. We have also successfully measured ZnOs electrical properties, namely the electric field produced by its spontaneous polarization, using the mechanical properties of polymers to immobilize ZnO QDs. The ZnO QDs in this work are synthesized using sol-gel method, and their average diameter is determined to be around 7 nm using the size-dependent PL spectroscopy. Raman spectroscopy, AFM, and TEM are used to further verify the size and structure of the QDs.

5.2 Methods

5.2.0.1 Synthesis

ZnO QDs were synthesized using the sol-gel method by first dissolving 2.8 g of potassium hydroxide (Sigma Aldrich, St. Louis, MO) in 50 mL of methanol (EM Science, Gibbstown, NJ) to make 1 M KOH solution and dissolving 0.55 g of zinc acetate dihydrate (Sigma Aldrich, St. Louis, MO) in 25 mL of methanol to make 0.1 M zinc acetate solution. The KOH solution was placed in a burette and added slowly to the zinc acetate solution while measuring the pH. The resulting solution was stirred and maintained at 50 C throughout the dropwise addition process.

The presence of a cloudy white precipitate indicated ZnO nanoparticle formation. When the pH reached a stable reading of 10-11, KOH addition was stopped, and the solution was left to stir for 1 hour, after which 0.25 mL of tetraethylorthosilicate (TEOS) (ACROS Organics, New Jersey, USA) was added. TEOS is a capping agent, and it prevents further growth of ZnO by coating the surface of the particle. [87] Following TEOS, 0.5 mL of water was added to the QD solution to aid the coating process. [88] The solution was then filtered using 3K Nanocep molecular weight cutoff device (Life Sciences, Ann Arbor, MI), once in methanol and twice in water, to remove any excess ions. The final product exhibited yellow fluorescence under UV light, confirming the presence of ZnO QDs.

5.2.1 LBL film synthesis

In order to accurately measure the electrostatic force and the corresponding electric field from colloidal ZnO QDs, the QDs should be immobilized. Immobilization can be achieved by processing the colloidal QDs into a thin film using LBL synthesis technique. ZnO quantum dots used for LBL films were suspended in 20 mM HEPES buffer with 1% sodium citrate (RICCA Chemical, Arlington, USA) to create a negatively-charged coating necessary for the successful synthesis of LBL films. [89] LBL films were prepared using previously described protocols. [57, 90, 91] A gold-coated silicon wafer was first placed into a petri dish with 0.5% poly(diallyldimethlammonium chloride) (PDDA) (Sigma Aldrich, St. Louis, USA), pH 3. After 10 minutes, it was removed and placed in deionized water (DI H2O) for 1 minute for rinsing. The wafer was then placed in ZnO solution for 20 minutes, followed by one minute of rinsing in DI H2O. The process was repeated to obtain the needed number of layers. (See Figure 27

(a) for a schematic diagram that summarizes the steps) The resulting films can be described as (PDDA/ZnO)n, where n is the number of PDDA/ZnO layers.

5.2.2 Characterization

To confirm the formation of ZnO QDs, the solution was placed in an Epi Chem II Darkroom (UVP Laboratory Products, Upland, CA) and illuminated with 254-nm UV light. PL and Raman spectra, which are know to be one of the most accurate method to characterize optical properties of nanostrutures, [92] were obtained with an IK Series He-Cd Laser (Kimmon Electric Company, Tokyo, Japan) and SpectraPro 2500 detector (Action Research Corporation, Greer, SC). PL measurements were obtained with a 325-nm wavelength excitation beam of 20 mW and a grating of 1200 grooves/mm. Raman measurements were obtained with a 442-nm wavelength excitation beam of 80 mW and a grating of 3600 grooves/mm. Samples were prepared by dropcasting ZnO solution on a silicon substrate. For TEM, a sample was prepared by placing a drop of colloidal ZnO QDs on a hydrophobic surface and placing a 200-mesh copper grid with a holey carbon layer (SPI Supplies, West Chester, PA) face down on the drop for 10 minutes. The sample was then moved to a clean surface facing up, and the excess solution was removed before imaging with JEOL JEM-100CXII (Tokyo, Japan). For ellipsometry (Gaertner Scientific L117, Skokie, IL), a sample was prepared by depositing LBL film on an intrinsic silicon wafer, and the dielectric constant of PDDA-ZnO QD layer was estimated as the average of static dielectric constant of bulk ZnO and PDDA. [93] Among possible values of thickness calculated by ellipsometry, a solution has been chosen so that the thickness of the substrate is close to the known value of the silicon substrate provided by the manufacturer. Finally, AFM and EFM

samples were prepared by synthesizing ZnO LBL film on a gold coated silicon wafer. Film thickness was measured using a Gaertner Scientific Ellipsometer (Skokie, IL). AFM and EFM measurements were performed on a Bruker Dimension Icon AFM (Billerica, MA). A conductive SCM-PIT probe was used for EFM measurements. To ensure that the probe is not within the atomic interaction range, the lift height for the interleave scan was set to 17 nm.

5.3 Results

5.3.1 UV radiation

ZnO is a direct band gap semiconductor, meaning an electron from in the conduction band can move to the valence band and recombine with a hole without changing momentum, with an unusually large band gap of 3.37 eV. [70] This recombination of electrons and holes releases energy which is responsible for a luminescence band of ZnO found in the UV region. As with other fluorescent QDs, this emission band is size dependent due to quantum confinement, with smaller QDs displaying lower-wavelength emission. Wurtzite ZnO, the most common form of ZnO, [94] also displays a second emission band in the visible region. Its size dependence and origin are not completely clear, but it is most likely caused by defects in the crystal structure, such as oxygen vacancies, zinc vacancies, interstitial zinc ions, oxygen antisites, and transitions. [95,96] Figure 25 shows the solution of ZnO QDs in methanol shortly after synthesis. As reported previously, the presence of visible luminescence is indicative of ZnO formation and signifies defects in the crystal structure. Subsequent PL measurements provided more detailed information on the emission spectrum of ZnO.

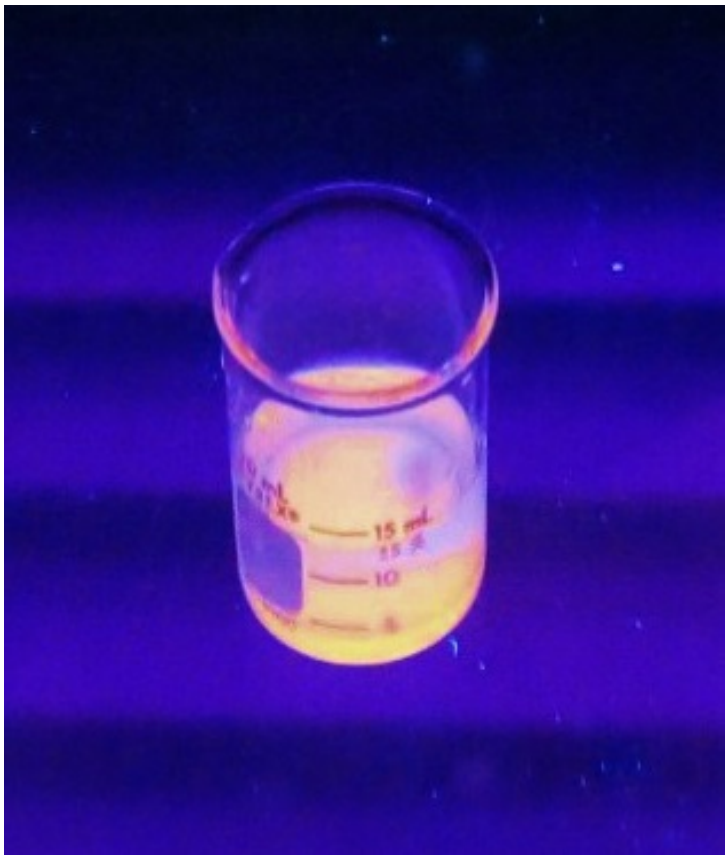

Figure 25: ZnO QDs displaying yellow luminescence in a UV darkroom. Wavelength of excitation light is 254 nm.

5.3.2 Photoluminescence Spectroscopy

PL studies have been undertaken in this work in order to estimate the diameters of the ZnO quantum dot synthesized in this study. Figure 26 shows the PL spectrum of ZnO QDs excited by a 325-nm wavelength He-Cd laser. As expected, the spectrum contains a strong UV peak and several weaker peaks in the visible range which are responsible for its luminescence.

The strong peak at 378 nm has been shown to be directly related to the band gap of the QD and is thus size-dependent due to quantum confinement. [95] The average size of the QDs can thus be approximated from the spectrum using the expression: [97]

$$E_g^{QD} = E_g^{bulk} + \frac{h^2}{8r^2}\left(\frac{1}{m_e m_0} + \frac{1}{m_h m_0}\right) - \frac{1.8e^2}{4\pi\epsilon r} - \frac{0.124e^4}{(2h\epsilon)^2}\left(\frac{1}{m_e m_0} + \frac{1}{m_h m_0}\right)^{-1} \tag{5.1}$$

where E_g^{QD} is the band gap of the QD,E_g^{bulk} is the band gap of bulk ZnO ($5.36 \times 10^{-19} J$), h is Plancks constant ($6.626 \times 10^{-34} m^2 kg/s$), r is QD radius, m_e is effective mass of an electron (0.29), m_h is the effective mass of a hole (1.21), [97] m_0 is mass of an electron ($9.11 \times 10^{-31} kg$), e is electron charge ($1.6 \times 10^{-19} C$), ϵ is the relative dielectric constant of ZnO (4.64), [98] and ϵ_0 is permittivity of free space ($8.85 \times 10^{-12} F/m$). The PL peak at 378 nm corresponds to $E_g^{QD} = 5.26 \times 10^{-19} J$. Substituting these values into the expression yields an r value of 3.4 nm, indicating that the average QD size is around 6.8 nm. Several theories exist to explain ZnO luminescence in the 500-600 nm range. [84] Studies comparing ZnO prepared under different gases demonstrated that the peak observed around 510 nm is higher in intensity for ZnO

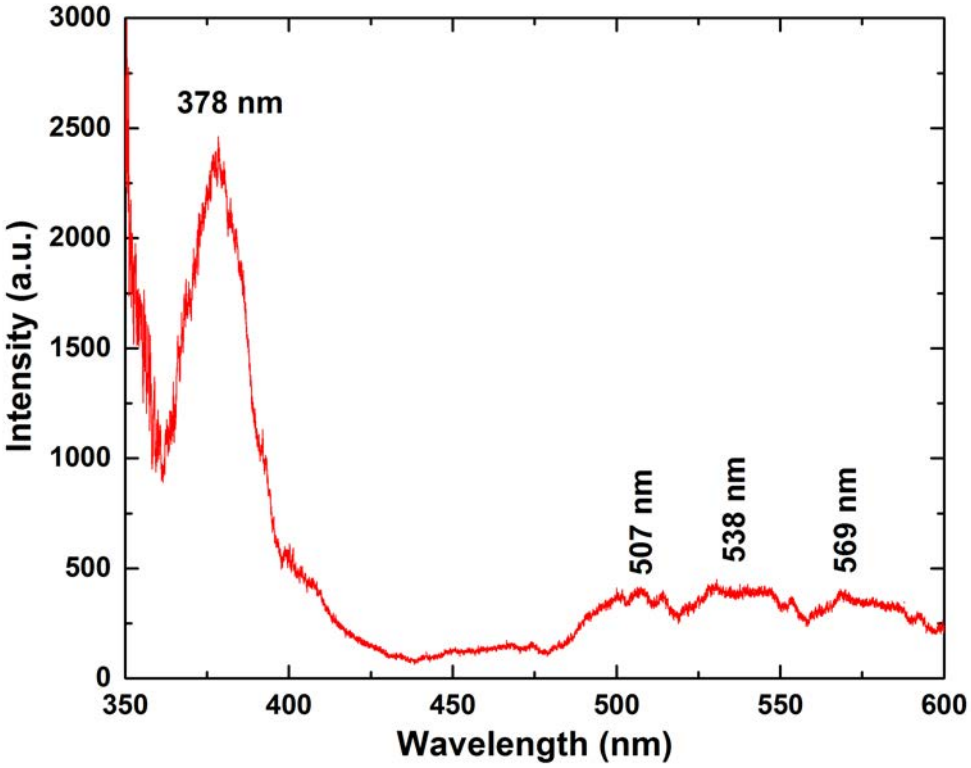

Figure 26: PL spectrum of ZnO QDs obtained with 325-nm wavelength laser source. Laser power is 20 mW.

annealed in N_2 than for ZnO annealed in O_2, suggesting that oxygen vacancies are responsible for this emission band. [99] Because the ZnO used in our study is in O_2 atmosphere during and after synthesis, oxygen vacancies are less abundant and the visible range bands are weak in intensity compared to the UV absorption band. Other studies have attributed the visible range peaks to Zn vacancies which occur frequently in ZnO prepared in O_2 atmosphere. Zn vacancies are acceptors with a ground level which is located above the ZnO valence band, so conduction band electrons may recombine with Zn vacancy centers, resulting in energy release. [100, 101] Zn interstitials, in turn, can act as donors, with ground levels located slightly below the conduction band. While these defects typically result in green-range emission, the peak location is also in part temperature-dependent. At room temperature, an electron is typically moved from an interstitial Zn level to the conduction band and subsequently recombines with a hole at the oxygen vacancy level, releasing a photon of energy around 2.25 eV (551 nm). At lower temperatures, a conduction band electron is captured at the Zn interstitial level and subsequently recombines with a hole at the oxygen vacancy level, releasing a photon of energy around 2.1 eV (590 nm). [96] Several studies also observed a size-dependence of the visible emission band, with larger QDs displaying a red-shifted, broader band, while smaller QDs display a sharper blue-shifted band. [83, 88] In summary, the visible range peaks in the ZnO PL spectrum are likely due to a combination of Zn and oxygen vacancies and Zn interstitials caused by experimental conditions such as temperature and gases present, as well as QD size. The strong UV peak at 378 nm suggests that the average QD diameter is around 7 nm, which is in agreement with AFM and TEM measurements presented later in this work.

5.3.3 Raman Spectroscopy

The non-resonant Raman spectroscopy spectrum of ZnO QDs obtained in this study is shown in Figure 27. It is observed that the spectrum consist of peaks at 440 cm^{-1} and 577 cm^{-1}. The 440 cm^{-1} peak corresponds to E2 (high) phonon while the 577 cm^{-1} peak is attributed to LO phonon with an intermediate phonon frequency between A1 (LO) at 574 cm^{-1} and E1 (LO) at 591 cm^{-1}. [102] The E2 (high) phonon peak has been shown to exhibit a large shift variation due to impurities present or due to variation in the constituent isotropic masses of atoms forming ZnO. [103]

5.3.4 Transmission Electron Microscopy (TEM)

In this work we have imaged the synthesized ZnO quantum dots using TEM, and the image of ZnO QDs is shown in Figure 28. The inset image in Figure 28 is the Fourier transform of the image representing the presence of crystal structures. The crystal structures circled in red embedded in amorphous carbon region were identified as ZnO QDs that are sized from 5 nm to 10 nm, which is in agreement with earlier calculations from PL spectrum and subsequent AFM measurements.

5.3.5 Ellipsometry of LBL film

To augment the previously-discussed characterization methods used to determine the physical and optical properties of ZnO QDs, additional characterizations of ZnO LBL films have been accomplished using ellipsometry. Figure 29 shows the thickness of the film with different numbers of layers obtained by averaging 7 different measurements from various locations of the sample. While the absolute value of the thickness should be considered as estimation, the

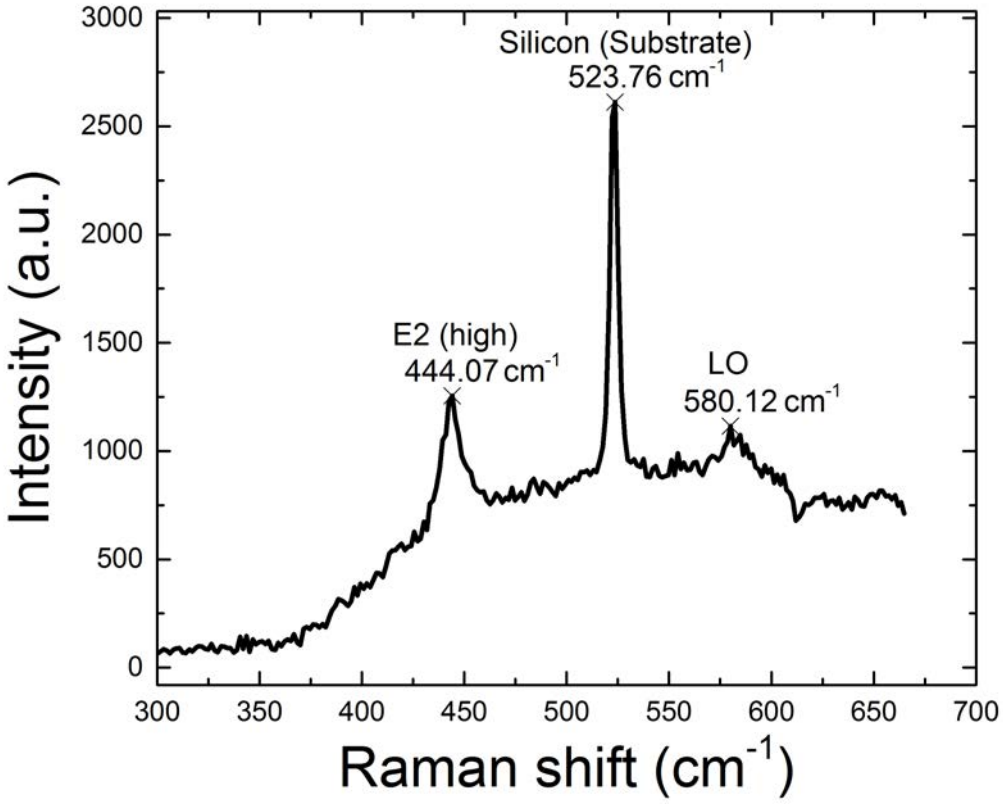

Figure 27: Nonresonant Raman spectrum of ZnO QD excited with a laser source of 442 nm wavelength. Laser power is 80 mW. Background spectrum has been subtracted from the obtained data.

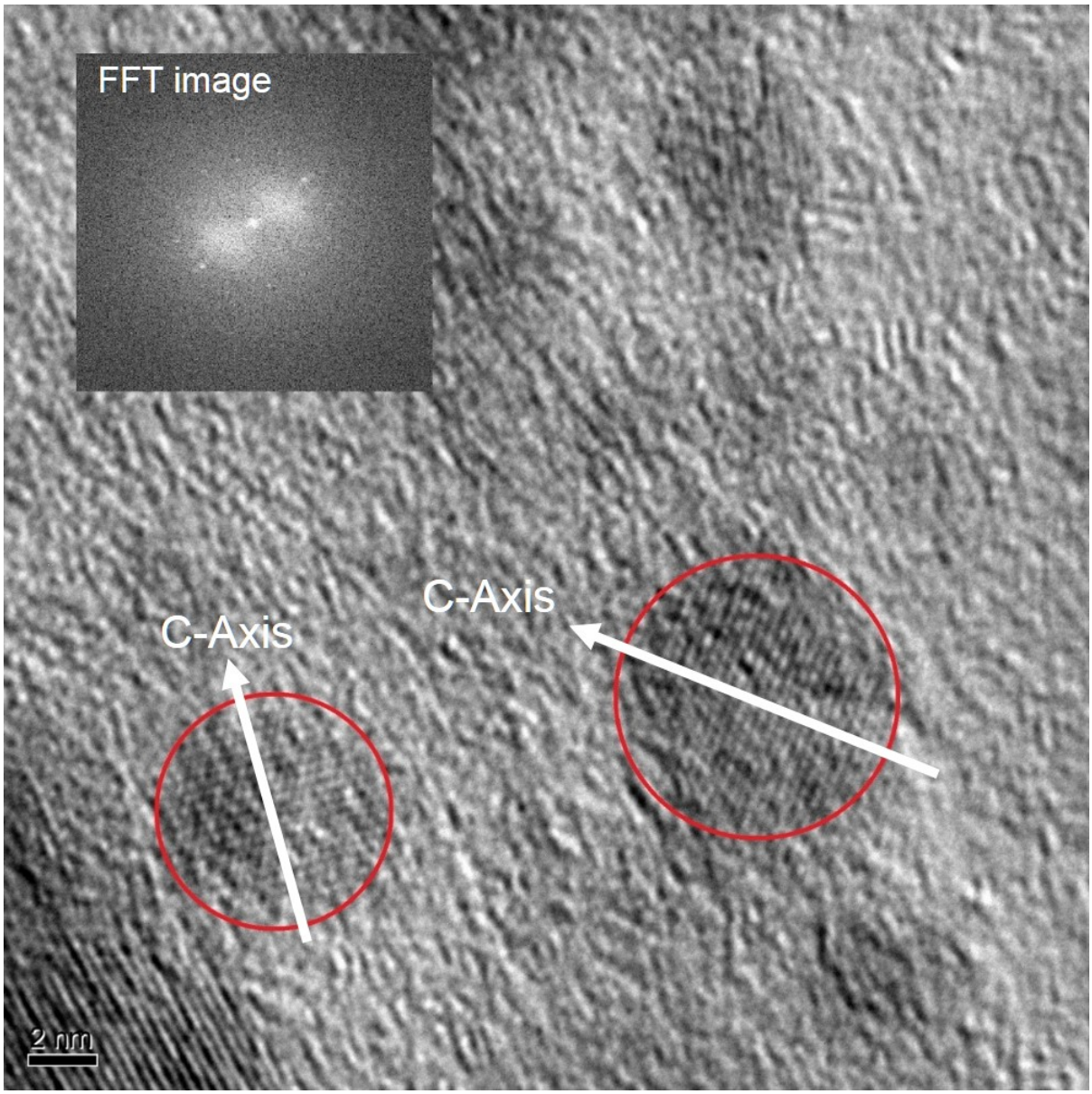

Figure 28: Typical TEM image of ZnO QDs. The red circles indicate the locations of ZnO QDs. The inset image shows the Fourier transform of the image representing the presence of crystal structures in parts of the image.

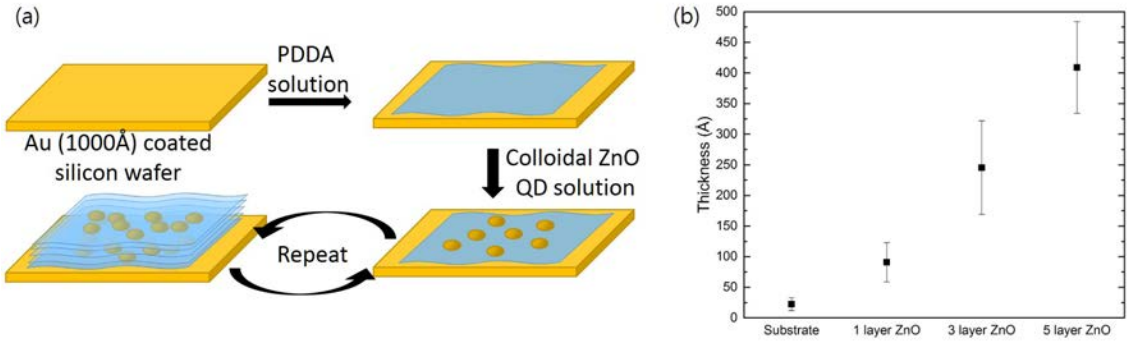

Figure 29: (a) Schematic diagram of LBL film assembly. (b) Thickness of ZnO LBL films with different number of layers calculated via ellipsometry. The substrate used was an intrinsic silicon wafer.

increasing pattern suggests that one layer of the film is approximately 8 nm thick, and the thickness of the film is uniform.

These results demonstrate that LBL films can be successfully synthesized with ZnO QDs and polycation polymers, which is essential for our subsequent AFM and EFM measurements. ZnO-polymer LBL films also have potential biomedical applications. Pappas et al, for instance, demonstrated that neuronal cells can be grown on an LBL surface containing HgTe nanoparticles, which can subsequently be excited with IR radiation, generating electric fields and thereby inducing action potentials in the neuronal cells. [57] In our case, since ZnO QDs have built-in

spontaneous polarization, no external radiation is needed to polarize them. The lack of need for external radiation is practical when considering the potential biological and medical uses of these LBL films.

5.3.6 Atomic Force Microscopy

Atomic force microscopy was performed on a $(PDDA/ZnO)_3$ sample for the topology measurement of a ZnO LBL film. Figure 30 shows the typical pattern of a ZnO LBL film with corresponding height profiles for selected (dash lined) regions. It appears that three ZnO QDs embedded in PDDA are shown in 500 nm by 500 nm area. The top three dashed lines show ZnO QDs with diameters of 6 nm to 8 nm. The bottom-most dashed line, which is less than 3 nm in height according to its height profile, indicates that the smaller dot-like structures are likely PDDA.

5.3.7 Electrostatic Force Microscopy

The EFM measurements of ZnO in LBL films are used here to study the electrical properties of ZnO caused by its spontaneous polarization. The electrostatic force generated by the QDs can be estimated from the EFM phase shift using the spring constant of the EFM probe. The resulting electric field can subsequently be calculated using the net surface charge of the ZnO QDs. Figure 31 shows the typical EFM pattern with the corresponding probe displacement in the lift mode. The red circles indicate ZnO QDs embedded in the PDDA, and the blue circles indicate clumps of PDDA. The two regions indicated in Figure 31(a) are similar in heights (about 3 nm higher from the rest of the sample), but the lift scan in Figure 31(b) shows that the regions indicated by the blue circles do not attract the probe, which means that the regions

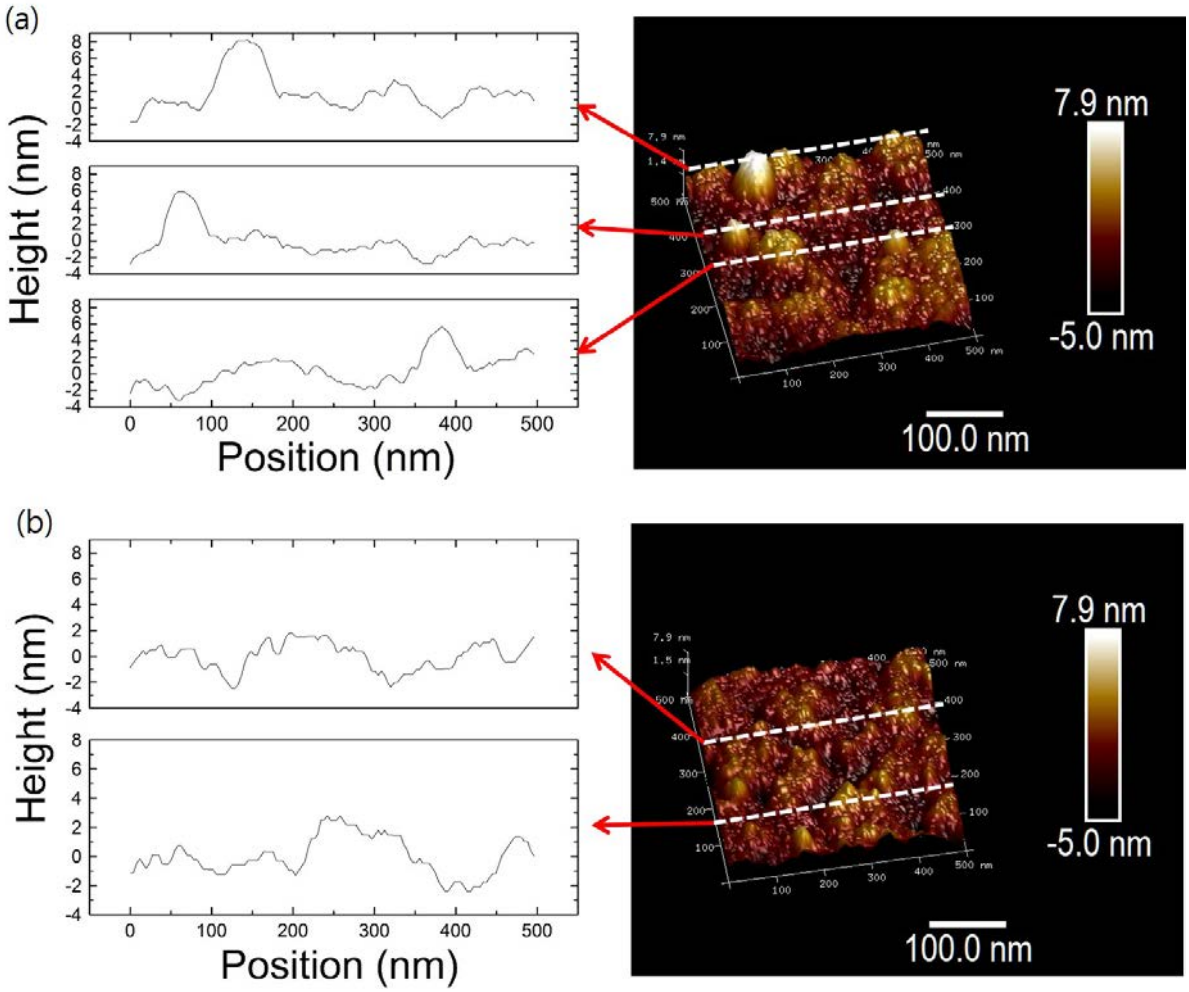

Figure 30: Typical AFM pattern of (a) a (PDDA/ZnO)3 film (b) a PDDA film with corresponding height profiles for selected (dashed lined) regions.

are without any electrostatic force. The regions indicated with the red circles, however, do attract the probe, which indicates that the regions clearly exhibit electrostatic forces. Further analysis is done using Lorentzs law, $F = qE$, where F is electrostatic force, q is the charge, and E is the electric field. Considering that the SCM-PIT probe has the spring constant of 2.8 N/m, the corresponding force to the 150 pm displacement, shown in Figure 31(c), is 420 pN. The amount of charge in ZnO QD with the diameter of 7 nm can be written by the charge per unit area, $0.07C/m^2$, times the exposed surface area of ZnO QD, $38.5nm^2$ which is equal to $0.07C/m^2 \times \pi(7nm)^2 = 2.7 \times 10^{-18}C$. Then the amplitude of the electric field from the ZnO QD can be estimated by $E = \frac{F}{q} \approx 10^8 V/m$.

Considering that the distance- and orientation-dependent electrostatic field produced from the spontaneous polarization of a ZnO QD is given by

$$E_{QD}^{spon} = \frac{P}{3\epsilon}\frac{R^3}{r^3}\left[2\cos(\theta)\hat{(r)} + \sin(\theta)\hat{\theta}\right], r > R \tag{5.2}$$

where P is the polarization, R is the radius of the QD, ϵ is the dielectric function of the media, θ is the angle of the growth axis, and r is the distance from the center of the QD, the theoretical value at 10 nm from the QD when $\theta = 0$ is approximately $0.9 \times 10^8 V/m$, which is comparable to the experimental result.

The orientation dependence of the electric field can be also measured by examining the shift of the cantilever oscillation phase in EFM since it provides a more accurate determination than is obtained by study of the amplitude displacement profile. The phase shift can be interpreted

as the perturbation of the harmonic oscillation of the probe. The mathematical relationship between the phase shift and the force can be described as [64]

$$\Delta\phi = -\frac{Q}{k}\frac{dF}{dz} \tag{5.3}$$

where Q is the quality factor, k is the spring constant, F is the perturbing force, which is the electrostatic force acting on the probe in this work, and z-axis is the probe oscillation axis. Therefore, when the electrostatic force from one QD is relatively stronger than another QD, the phase shift of the QD is larger than the other. Considering that the distance between the probe and QDs are constant, by setting the lift height as equal, the dominant factor of the change in the electrostatic field strength from different QDs can be understood as the change in orientation of QDs, when the size of the QDs are similar. Figure 31(a) shows the map of 5 ZnO QDs that are similarly sized. The phase shift shown in Figure 32(a) depicts, for instance, that the phase shift caused by the electrostatic force from QD1 is bigger than that of QD4, which can be interpreted that the angle between the c-axis of the QD1 and the probe oscillation axis, z, is smaller than that of QD4. A complete analysis of a suggested QD orientation is presented in Figure 32(b). While the quantification of the electric field is extremely difficult because lots of approximations and assumptions are involved, this technique is useful to see how the ZnO QDs are oriented relative to each other.

Knowing the electric field produced by ZnO is useful when considering some of the many applications of ZnO. In the example given earlier on neuronal stimulation using LBL films, the electric field produced by ZnO can be used to calculate the necessary distance between the QD

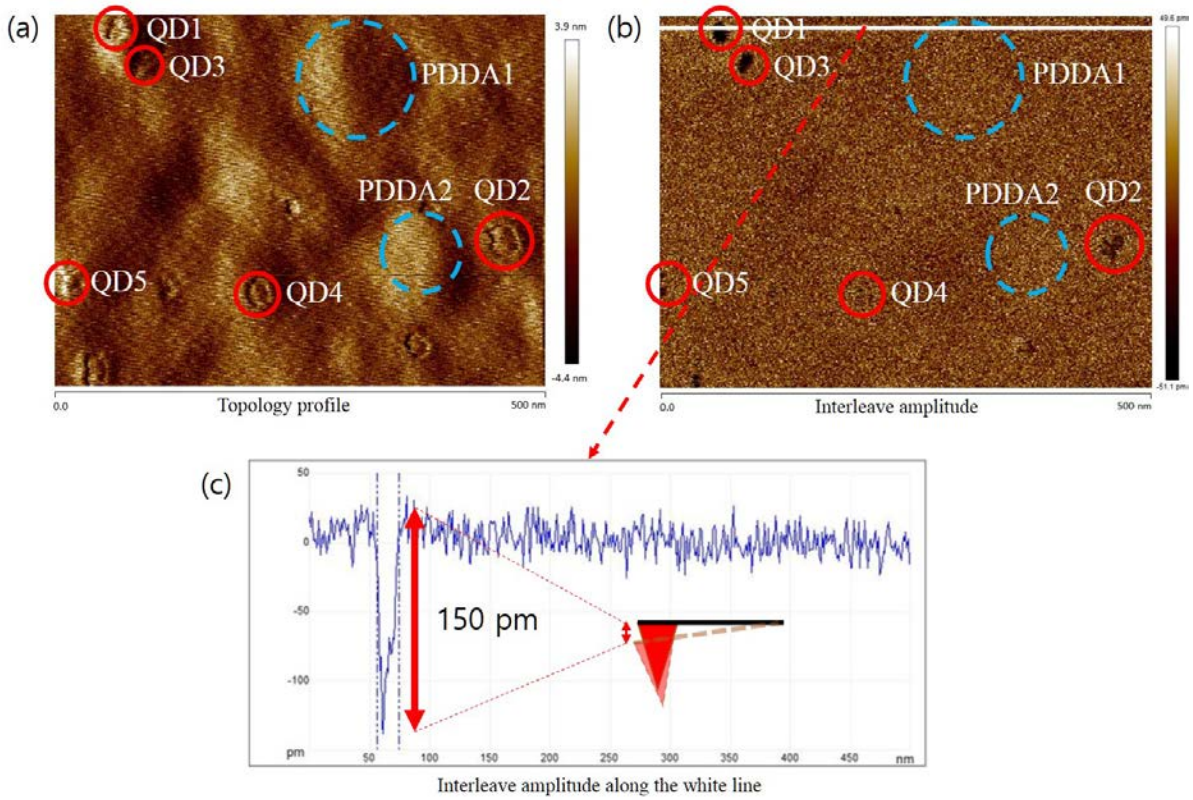

Figure 31: Typical EFM pattern of ZnO QDs in PDDA polymer. (a) Top view of topology map. Red solid circles indicate QDs and blue dashed circle indicate clumps of PDDA. (b) Probe displacement pattern in the lift mode (interleave amplitude) (c) Corresponding displacement profile of the region indicated by the white line. The schematic drawing indicates the movement of the probe attractive by the electrostatic force from a ZnO QD.

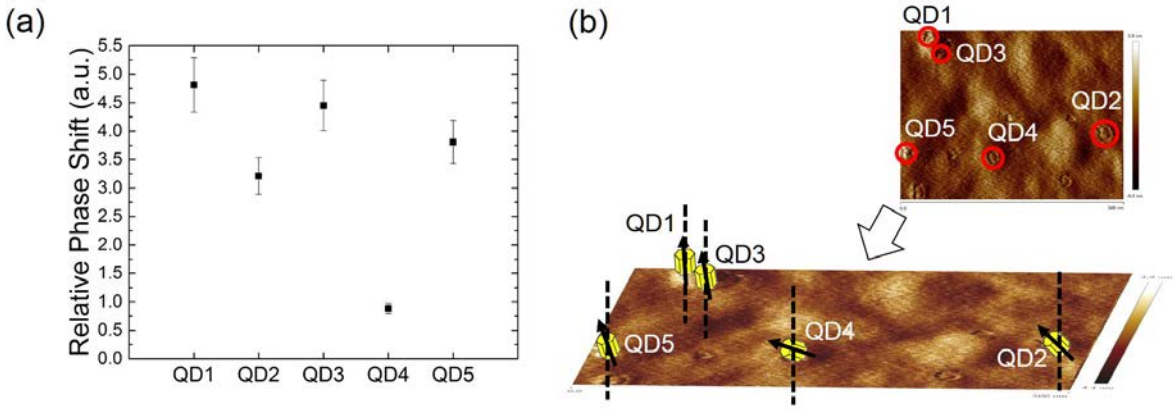

Figure 32: The effect of the orientation of ZnO QDs on the electrostatic force. (a) The change in phase of the EFM tip cantilever oscillation due to electrostatic forces. Labels of QDs corresponds to the map shown in Figure 7(a). (b) The location map of the QDs and the schematic diagrams of possible orientations of QDs. Arrows indicates the c-axis of QDs and the dashed lines are the axis normal to the surface.

and the cell membrane to induce an action potential. [57] It has also been shown, for instance, that when synthesizing ZnO-graphene hybrid structures, the orientation of ZnOs growth axis affects its binding strength to graphene due to a charge redistribution in graphene in response to ZnOs dipole. [104] Because ZnO is often used in various hybrid structures, knowing its electric field can give important insight into its interactions with other materials.

CHAPTER 6

CONCLUSION AND FUTURE WORK

This dissertation presented screening, coulomb interactions, and plasmonic phenomena on the nanoscale that affect luminescent, ionic, and electrolytic Properties of Nanostructures. In Chapter 2, theories of optical absorption mechanism in indirect band gap semiconductor, silicon, were proposed. a confined SPP can provide both energy and momentum to excite an electron in the valence band of silicon to the conduction band, which normally is difficult to happen with photons. Conventional second order process was supplemented by stimulated Raman scattering theory that would generate a massive number of coherent phonons with an assist of plasmons. The promising qualitative agreement with the experimental data was obtained which will lead to several future works that will be discussed later in this chapter in detail.

In Chapter 3, numerical studies have performed on the SCS of nonprecious metals, aluminum, nickel, and copper, to investigate the possibility of the metals as plasmonic materials in visible range as a replacement of already known good plasmonic materials such as silver and gold which are not cost effective. The results show that in the visible range, nonprecious metal nanodisks can be a good substitute of precious metals, and the SCS of them are tunable by changing their diameters. This will open up many opportunities in the future applications.

Chapter 4 discussed the effect of static electric field producing quantum dots on the ionic currents through ion channels in catfish horizontal retina cells by modifying the membrane potential. Hodgkin and Huxley model was used to back up the experimental findings which

agreed each other. It is shown that the electric field producing QDs, TiO_2 and ZnO QDs, indeed affect the ion current in a neuronal cell by changing the membrane potential. It is especially true in the physiologically relevant region where voltage-gated Na^+ and K^+ channels plays major roles.

Finally in Chapter 5, synthesis and optical, structural, electrostatic characterization of ZnO quantum dots were demonstrated. Knowing the electric field produced by ZnO is useful when considering some of the many applications of ZnO. In the example given earlier on neuronal stimulation using LBL films, the electric field produced by ZnO can be used to calculate the necessary distance between the QD and the cell membrane to induce an action potential. It has also been shown, for instance, that when synthesizing ZnO-graphene hybrid structures, the orientation of ZnOs growth axis affects its binding strength to graphene due to a charge redistribution in graphene in response to ZnOs dipole. Because ZnO is often used in various hybrid structures, knowing its electric field can give important insight into its interactions with other materials.

This work has demonstrated several promising aspects of various research on the nanoscale which inspires future works. First of all, hot luminescence from silicon has been very demanding, yet extremely hard to achieve. With the qualitatively agreeable 1D approximation and 3D study can lead to in-depth analysis. In the future, since the plasmonic interaction in silicon is likely a nonlinear process, the wavevector- and frequency-dependent second and third order susceptibility has been studied for better estimation as shown in Appendix A. Also, the 3D cylindrical Ag-SiO_2-Si system has been worked out, and can be researched further. With more

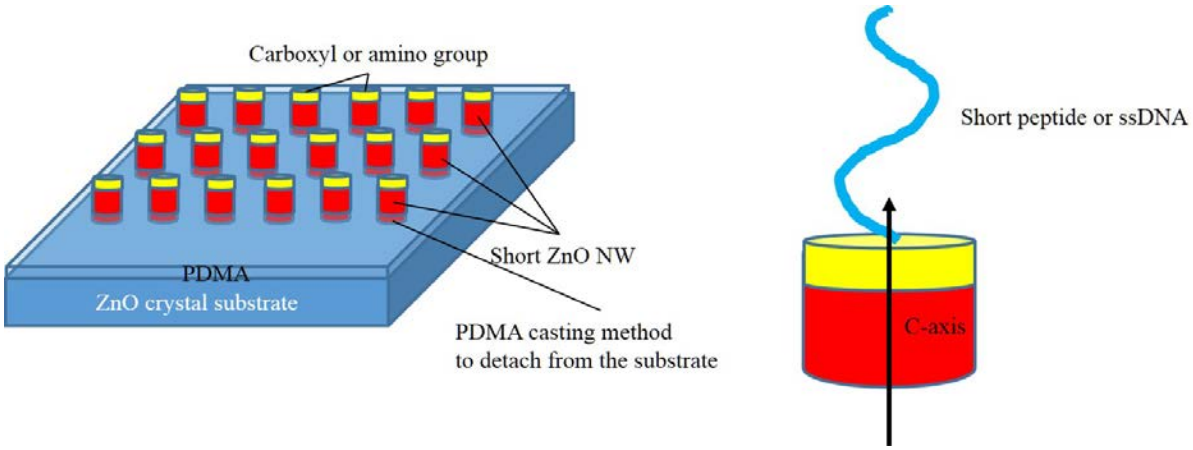

Figure 33: Schematic diagram of a proposed method to bind QDs on an integrins of a cell.

studies in the normalization and better estimation method of plasmonic coupling efficiency, the quantitative comparison to the conventional second-order process for the quantum yield estimation can be achieved as well.

Secondly, research on ion channels presented in Chapter 4 can be improved by binding quantum dots on or near the ion channels of a cell. A possible method is to use a short peptide or single stranded DNA (ssDNA) to Carbolxyl or amino group treated quantum dots that are grown in the same direction using PDDA casting method. [105, 106] Then the QD compounds can be directly bound to integrins of a cell to be immobilized near the cell membrane for stability. [107]

CITED LITERATURE

1. Rakic, A. D., Djurisic, A. B., Elazar, J. M., and Majewski, M. L.: Optical properties of metallic films for vertical-cavity optoelectronic devices. Applied Optics, 37(22):5271, August 1 1998.

2. Lutgens, F. K. and Tarbuck, E. J.: Essentials of geology. Boston, Prentice Hall, 11 edition, 2012.

3. Schutt-Aine, J.: Interconnections and Signal Integrity: DAC Tutorial.

4. Cho, C., Aspetti, C. O., Park, J., and Agarwal, R.: Silicon coupled with plasmon nanocavities generates bright visible hot luminescence. Nature Photonics, 7(4):285, April 1 2013.

5. Chelikowsky, J. and Cohen, M.: Electronic structure of silicon. Phys. Rev. B., 10(12):5095, July 1974.

6. Kerker, M., Wang, D.-S., and Chew, H.: Surface enhanced raman scattering (sers) by molecules adsorbed at spherical particles. Applied Optics, 19(19):3373–3388, October 1 1980.

7. Ru, E. C. L. and Etchegoin, P. G.: Principles of surface-enhanced Raman spectroscopy. Amsterdam, Elsevier, 2009.

8. Trolle, M.: Microscopic theory of linear & nonlinear optical response: Zinc-blende semiconductors, 2011.

9. McMahon, J. M., Gray, S. K., and Schatz, G. C.: Nonlocal optical response of metal nanostructures with arbitrary shape. Physical review letters, 103(9):097403, August 28 2009.

10. Onida, G., Reining, L., and Rubio, A.: Electronic excitations: density-functional versus many-body green's-function approaches. Reviews of Modern Physics, 74(2):601, April 1 2002.

11. Kohn, W. and Sham, L. J.: Self-consistent equations including exchange and correlation effects. Physical Review, 140(4A):A1138, November 1965.

12. Winn, J. N., Johnson, S. G., Meade, R. D., and Joannopoulos, J. D.: Photonic Crystals: Molding the Flow of Light. Princeton University Press, 2nd edition, 2008.

13. Choi, M. S., Dutta, M., and Stroscio, M. A.: Numerial analysis of local density of states of plasmons in si-sio$_2$-silver nanocavity system. Piscataway, June 1, 2014. The Institute of Electrical and Electronics Engineers, Inc. (IEEE).

14. Mishchenko, E. G.: Dipole-induced localized plasmon modes and resonant surface plasmon scattering. Physical Review B, 88(11), September 2013.

15. Xu, Y., Lee, R. K., and Yariv, A.: Quantum analysis and the classical analysis of spontaneous emission in a microcavity. Physical Review A, 61(3):033807, February 2000.

16. Oskooi, A. F., Roundy, D., Ibanescu, M., Bermel, P., Joannopoulos, J. D., and Johnson, S. G.: Meep: A flexible free-software package for electromagnetic simulations by the fdtd method. Computer Physics Communications, 181(3):687–702, 2010.

17. Burke, J. J., Stegeman, G. I., and Tamir, T.: Surface-polariton-like waves guided by thin, lossy metal films. Physical Review B, 33(8):5186–5201, April 1986.

18. Prade, B., Vinet, J., and Mysyrowicz, A.: Guided optical waves in planar heterostructures with negative dielectric constant. Physical Review B, 44(24):13556–13572, December 1991.

19. Trolle, M. L. and Pedersen, T. G.: Indirect optical absorption in silicon via thin-film surface plasmon. Journal of Applied Physics, 112(4):043103, August 15 2012.

20. Balanis, C. A.: Advanced engineering electromagnetics. Hoboken, NJ, Wiley, 2. ed. edition, 2012.

21. Cho, C.-H., Aspetti, C. O., Turk, M. E., Kikkawa, J. M., Nam, S.-W., and Agarwal, R.: Tailoring hot-exciton emission and lifetimes in semiconducting nanowires via whispering-gallery nanocavity plasmons. Nature materials, 10(9):669–675, September 2011.

22. Miles, J. W.: Integral Transforms in Applied Mathematics. Cambridge University Press, November 1 1971.

23. Butkov, E.: Mathematical Physics. Reading, MA, Addison-Wesley, 1968.

24. Weber, H. J. and Arfken, G. B.: Mathematical Methods for Physicists. Academic Press, October 22 2013.

25. Deen, M. J. and Basu, P. K.: Silicon photonics. Chichester, Wiley, 1 edition, 2012.

26. Leburton, J. P. and Dorda, G.: Remote polar phonon scattering for hot electrons in si-inversion layers. Solid State Communications, 40(11):1025–1026, 1981.

27. Hess, K. and Vogl, P.: Remote polar phonon scattering in silicon inversion layers. Solid State Communications, 30(12):797–799, 1979.

28. Kisin, M. V., Gorfinkel, V. B., Stroscio, M. A., Belenky, G., and Luryi, S.: Influence of complex phonon spectra on intersubband optical gain. Journal of Applied Physics, 82(5):2031, September 1 1997.

29. Choi, M. S., Zhang, N., Dutta, M., Stroscio, M. A., Aspetti, C. O., and Agarwal, R.: Plasmon excitation of coherent interface phonons in si-sio$_2$ systems. IEEE, 2014.

30. Gale, J. D. and Rohl, A. L.: The general utility lattice program (gulp). Molecular Simulation, 29(5):291–341, January 1 2003. and E.R. Cope and M.T. Dove. Pair distribution functions calculated from interatomic potential models using the general utility lattice program. J. Appl. Crystallogr., 40:589594, 2007.

31. Ashley, J. C., Ritchie, R. H., and Crawford, O. H.: Energy loss and scattering of subexcitation electrons in sio/sub 2, September 2 2008.

32. Temnov, V. V., Klieber, C., Nelson, K. A., Thomay, T., Knittel, V., Leitenstorfer, A., Makarov, D., Albrecht, M., and Bratschitsch, R.: Femtosecond nonlinear ultrasonics in gold probed with ultrashort surface plasmons. Nature communications, 4:1468, 2013.

33. Yan, Y.-X., Gamble, E. B., and Nelson, K. A.: Impulsive stimulated scattering: General importance in femtosecond laser pulse interactions with matter, and spectroscopic applications. The Journal of Chemical Physics, 83(11):5391, 1985.

34. Maier, S. A.: Plasmonics - Fundamentals and Applications. Springer, 2007.

35. Shen, Y. R. and Bloembergen, N.: Theory of stimulated brillouin and raman scattering. Physical Review, 137(6A):A1805, March 1965.

36. Ritchie, R. H.: Plasma losses by fast electrons in thin films. Physical Review, 106(5):874–881, June 1957.

37. Vo-Dinh, T.: Surface-enhanced raman spectroscopy using metallic nanostructures. TrAC Trends in Analytical Chemistry, 17(8-9):557–582, August 9 1998.

38. Li, W.-D., Ding, F., Hu, J., and Chou, S. Y.: Three-dimensional cavity nanoantenna coupled plasmonic nanodots for ultrahigh and uniform surface-enhanced raman scattering over large area. Optics express, 19(5):3925, February 28 2011.

39. Lin, X.-M., Cui, Y., Xu, Y.-H., Ren, B., and Tian, Z.-Q.: Surface-enhanced raman spectroscopy: substrate-related issues. Analytical and Bioanalytical Chemistry, 394(7):1729–1745, August 1 2009.

40. Mukherjee, S., Karmakar, R., and Deyasi, A.: Theoretical computation of transmission coefficient of double quantum well triple barrier structure in presence of electric field. Int. J. of Soft Computing. and Engineering (IJSCE), 1:41–44, 2011.

41. Karmakar, R., Mukherjee, S., and Deyasi, A.: Numerical analysis of transmission coefficient of double quantum well triple barrier structure for variable effective mass using transfer matrix. 2011.

42. Mukherjee, S., Farid, S., Stroscio, M. A., and Dutta, M.: Modeling polycrystalline effects on the device characteristics of cdte based solar cells. page 1, Piscataway, September 1, 2015. The Institute of Electrical and Electronics Engineers, Inc. (IEEE).

43. Alberts, B.: Essential cell biology. New York, NY, Garland Science, 4. ed. edition, 2014.

44. Traynelis, S. F., Wollmuth, L. P., McBain, C. J., Menniti, F. S., Vance, K. M., Ogden, K. K., Hansen, K. B., Yuan, H., Myers, S. J., and Dingledine, R.: Glutamate receptor ion channels: structure, regulation, and function. Pharmacological reviews, 62(3):405–496, September 2010.

45. Masland, R. H.: The fundamental plan of the retina. Nature Neuroscience, 4(9):877–886, September 2001.

46. Shingai, R. and Christensen, B. N.: Sodium and calcium currents measured in isolated catfish horizontal cells under voltage clamp. Neuroscience, 10(3):893–897, 1983.

47. Hodgkin, A. L., Huxley, A. F., and Katz, B.: Measurement of currentvoltage relations in the membrane of the giant axon of loligo. The Journal of Physiology, 116(4):424–448, April 28 1952.

48. Takahashi, K., Dixon, D. B., and Copenhagen, D. R.: Modulation of a sustained calcium current by intracellular ph in horizontal cells of fish retina. The Journal of general physiology, 101(5):695–714, May 1993.

49. Foa, P. P.: Ion channels and ion pumps, volume 6. New York u.a, Springer, 1994.

50. Marten, I. and Hoshi, T.: Voltage-dependent gating characteristics of the k1 channel kat1 depend on the n and c termini. page 34483453, 1997.

51. Jonz, M. G. and Barnes, S.: Proton modulation of ion channels in isolated horizontal cells of the goldfish retina. The Journal of Physiology, 581(2):529–541, June 1 2007.

52. Hirasawa, H. and Kaneko, A.: ph changes in the invaginating synaptic cleft mediate feedback from horizontal cells to cone photoreceptors by modulating ca^2+ channels. The Journal of general physiology, 122(6):657–671, December 2003.

53. Strege, P. R., Bernard, C. E., Kraichely, R. E., Mazzone, A., Sha, L., Beyder, A., Gibbons, S. J., Linden, D. R., Kendrick, M. L., Sarr, M. G., Szurszewski, J. H., and Farrugia, G.: Hydrogen sulfide is a partially redox-independent activator of the human jejunum na^+ channel, $na_v1.5$. American Journal of Physiology, 300(6):G1105, June 1 2011.

54. Hbner, C. A. and Jentsch, T. J.: Ion channel diseases. Human molecular genetics, 11(20):2435–2445, October 1 2002.

55. Alexson, D., Chen, H., Cho, M., Dutta, M., Li, Y., Shi, P., Raichura, A., Ramadurai, D., Parikh, S., Stroscio, M. A., and Vasudev, M.: Semiconductor nanostructures in biological applications. Journal of Physics: Condensed Matter, 17(26):R656, July 6 2005.

56. Stroscio, M. A., Dutta, M., Narwani, K., Shi, P., Ramadurai, D., and Rufo, S.: Biological Nanostructures and Applications of Nanostructures in Biology, volume 2. Kluwer Academic Publishers, August 1 2004.

57. Pappas, T. C., Wickramanyake, W. M. S., Jan, E., Motamedi, M., Brodwick, M., and Kotov, N. A.: Nanoscale engineering of a cellular interface with semiconductor nanoparticle films for photoelectric stimulation of neurons. Nano letters, 7(2):513–519, February 2007.

58. Winter, J. O., Gomez, N., Korgel, B. A., and Schmidt, C. E.: Quantum dots for electrical stimulation of neural cells. volume 5705, April 28, 2005.

59. Kreitzer, M. A., Collis, L. P., Molina, A. J. A., Smith, P. J. S., and Malchow, R. P.: Modulation of extracellular proton fluxes from retinal horizontal cells of the catfish by depolarization and glutamate. The Journal of general physiology, 130(2):169–182, August 2007.

60. Jacoby, J., Kreitzer, M. A., Alford, S., Qian, H., Tchernookova, B. K., Naylor, E. R., and Malchow, R. P.: Extracellular ph dynamics of retinal horizontal cells examined using electrochemical and fluorometric methods. Journal of Neurophysiology, 107(3):868–879, February 1 2012.

61. Reeke, G. N.: Modeling in the neurosciences. Boca Raton, Fla., Taylor & Francis, 2nd ed. edition, 2005.

62. Tachibana, M.: Ionic currents of solitary horizontal cells isolated from goldfish retina. The Journal of Physiology, 345(1):329–351, December 1 1983.

63. Usui, S., Kamiyama, Y., Ishii, H., and Ikeno, H.: Reconstruction of retinal horizontal cell responses by the ionic current model. Vision Research, 36(12):1711–1719, 1996.

64. Choi, M., Meshik, X., Dutta, M., and Stroscio, M.: Screening effect on electric field produced by spontaneous polarization in zno quantum dot in electrolyte. page 1, Piscataway, September 1, 2015. The Institute of Electrical and Electronics Engineers, Inc. (IEEE).

65. Bezanilla, F.: How membrane proteins sense voltage. Nature Reviews Molecular Cell Biology, 9(4):323–332, April 2008.

66. Tombaugh, G. C. and Somjen, G. G.: pH modulation of voltage-gated ion channels. In pH and Brain Function. New York, Wiley, 1998.

67. Molitor, S. C., Tong, M., and Vora, D.: Matlab-based simulation of whole-cell and single-channel currents. J Undergrad Neurosci Educ., 4(2):A74A82, 2006.

68. Kurachi, Y.: Voltage-dependent activation of the inward-rectifier potassium channel in the ventricular cell membrane of guinea-pig heart. The Journal of Physiology, 366(1):365–385, September 1 1985.

69. Choi, M. S., Meshik, X., Mukherjee, S., Farid, S., Doan, S., Covnot, L., Dutta, M., and Stroscio, M. A.: Electrostatic force analysis, optical measurements, and structural characterization of zinc oxide colloidal quantum dots synthesized by sol-gel method. Journal of Applied Physics, 118(19):194304, November 21 2015.

70. Kolodziejczak-Radzimska, A. and Jesionowski, T.: Zinc oxidefrom synthesis to application: A review. Materials, 7(4):2833–2881, April 1 2014.

71. Das, A., Wang, D.-Y., Leuteritz, A., Subramaniam, K., Greenwell, H. C., Wagenknecht, U., and Heinrich, G.: Preparation of zinc oxide free, transparent rubber nanocomposites using a layered double hydroxide filler. Journal of Materials Chemistry, 21(20):7194, 2011.

72. Becheri, A., Drr, M., Nostro, P. L., and Baglioni, P.: Synthesis and characterization of zinc oxide nanoparticles: application to textiles as uv-absorbers. Journal of Nanoparticle Research, 10(4):679–689, April 2008.

73. Kong, Y. C., Yu, D. P., Zhang, B., Fang, W., and Feng, S. Q.: Ultraviolet-emitting zno nanowires synthesized by a physical vapor deposition approach. Applied Physics Letters, 78(4):407, 2001.

74. Venkatesh, P. S. and Jeganathan, K.: Investigations on the growth and characterization of vertically aligned zinc oxide nanowires by radio frequency magnetronsputtering. Journal of Solid State Chemistry, 200:84–89, April 2013.

75. Mirhosseini, M. and Firouzabadi, F. B.: Antibacterial activity of zinc oxide nanoparticle suspensions on foodborne pathogens. International Journal of Dairy Technology, 66(2):291–295, May 2013.

76. Xu, K., Purahmad, M., Brenneman, K., Meshik, X., Farid, S., Poduri, S., Pratap, P., Abell, J., Zhao, Y., Nichols, B., Zakar, E., Stroscio, M., and Dutta, M.: Design and Applications of Nanomaterials for Sensors. Dordrecht, Springer Netherlands, 2014.

77. Yamanaka, T., Dutta, M., and Stroscio, M.: Spontaneous polarization effects in nanoscale wurtzite structures. Journal of Computational Electronics, 6(1):313–316, September 2007.

78. Farid, S., Purahmad, M., Stroscio, M. A., and Dutta, M.: Computational analysis on the emission of zno nanowires and coreshell cdse/zns quantum dots deposited on different substrates. pages 1–3. IEEE, 2012.

79. Kirat, K. E., Burton, I., Dupres, V., and Dufrene, Y. F.: Sample preparation procedures for biological atomic force microscopy. Journal of Microscopy, 218(3):199–207, June 2005.

80. Shao, Z. and Zhang, Y.: Biological cryo atomic force microscopy: a brief review. Ultramicroscopy, 66(3):141–152, 1996.

81. Allison, D. P., Sullivan, C. J., Mortensen, N. P., Retterer, S. T., and Doktycz, M.: Bacterial immobilization for imaging by atomic force microscopy. Journal of visualized experiments : JoVE, (54), 2011.

82. eds. J. P. Sauvage and M. W. Hosseini Comprehensive supramolecular chemistry, volume 9 of Templating, Self-Assembly and Self-Organization.. OXford, Pergamon, 1996.

83. Decher, G.: Fuzzy nanoassemblies: Toward layered polymeric multicomposites. Science, 277(5330):1232–1237, August 29 1997.

84. Picart, C., Caruso, F., and Voegel, J.-C.: Layer-by-Layer Films for Biomedical Applications. Germany, Wiley-VCH, 1 edition, 2015.

85. Kotov, N. A., Dekany, I., and Fendler, J. H.: Layer-by-layer self-assembly of polyelectrolyte-semiconductor nanoparticle composite films. The Journal of Physical Chemistry, 99(35):13065–13069, August 1995.

86. Farid, S., Mukherjee, S., Jung, H., Stroscio, M., and Dutta, M.: Analysis on the structural, vibrational and defect states of chlorine treated polycrystalline cadmium telluride structures grown by e-beam evaporation. Mater. Res. Express, 2(2):025007, 2015.

87. Wu, L. Y. L., Tok, A. I. Y., Boey, F. Y. C., Zeng, X. T., and Zhang, X. H.: Chemical synthesis of zno nanocrystals. IEEE Transactions on Nanotechnology, 6(5):497–503, 2007.

88. Patra, M. K., Manoth, M., Singh, V. K., Gowd, G. S., Choudhry, V. S., Vadera, S. R., and Kumar, N.: Synthesis of stable dispersion of zno quantum dots in aqueous medium showing visible emission from bluish green to yellow. Journal of Luminescence, 129(3):320–324, 2009.

89. Yu, J., Baek, M., Chung, H. E., and Choi, S. J.: Effects of physicochemical properties of zinc oxide nanoparticles on cellular uptake. Journal of Physics: Conference Series, 304:012007, July 6 2011.

90. Cao, B., Cai, W., and Zeng, H.: Temperature-dependent shifts of three emission bands for zno nanoneedle arrays. Applied Physics Letters, 88(16):161101, 2006.

91. Sinani, V. A., Koktysh, D. S., Yun, B.-G., Matts, R. L., Pappas, T. C., Motamedi, M., Thomas, S. N., and Kotov, N. A.: Collagen coating promotes biocompatibility of semiconductor nanoparticles in stratified lbl films. Nano Letters, 3(9):1177–1182, September 2003.

92. Farid, S., Stroscio, M., and Dutta, M.: Raman scattering investigations of cds thin films grown by thermal evaporation. pages 45–48, July 2012.

93. Balandin, A., Alim, K., and Fonoberov, V.: Origin of the optical phonon frequency shifts in zno quantum dots. Applied Physics Letters, 86(5):3, January 25 2005.

94. Klingshirn, C., Waag, A., Hoffmann, A., and Geurts, J.: Zinc Oxide: From Fundamental Properties towards Novel Applications, volume 120. Berlin, Springer, 2010.

95. Zhang, L., Yin, L., Wang, C., lun, N., Qi, Y., and Xiang, D.: Origin of visible photoluminescence of zno quantum dots: Defect-dependent and size-dependent. J. Phys. Chem. C, 114(21):96519658, 2010.

96. Rodnyi, P. and Khodyuk, I.: Optical and luminescence properties of zinc oxide (review). Optics and Spectroscopy, 111(5):776–785, November 2011.

97. Gupta, A., Pandey, S. S., Nayak, M., Maity, A., Majumder, S. B., and Bhattacharya, S.: Hydrogen sensing based on nanoporous silica-embedded ultra dense zno nanobundles. RSC Advances, 2014.

98. Djurii, A. B., Chan, Y., and Li, E. H.: The optical dielectric function of zno. Applied Physics A Materials Science & Processing, 76(1):37–43, January 2003.

99. Shan, F. K., Liu, G. X., Lee, W. J., Lee, G. H., Kim, I. S., and Shin, B. C.: Aging effect and origin of deep-level emission in zno thin film deposited by pulsed laser deposition. Applied Physics Letters, 86(22):221910, 2005.

100. Kohan, A. F., Van de Walle, C. G., and Morgan, D.: First-principles study of native point defects in zno. Physical Review. B, Condensed Matter and Materials Physics, page 15019, June 1 2000.

101. Chen, H., Gu, S., Tang, K., Zhu, S., Zhu, Z., Ye, J., Zhang, R., and Zheng, Y.: Origins of green band emission in high-temperature annealed n-doped zno. Journal of Luminescence, 131(6):1189–1192, 2011.

102. Serrano, J., Manjn, F. J., Romero, A. H., Widulle, F., Lauck, R., and Cardona, M.: Dispersive phonon linewidths: the e2 phonons of zno. Physical review letters, 90(5):055510, February 7 2003.

103. Jerphagnon, J.: Invariants of the third-rank cartesian tensor: Optical nonlinear susceptibilities. Physical Review B, 2(4):1091–1098, August 1970.

104. Larson, K., Clark, A., Appel, A., Dai, Q., He, H., and Zygmunt, S.: Surface-dependence of interfacial binding strength between zinc oxide and graphene. RSC Adv, 5(81), 2015.

105. Mandal, G., Bhattacharya, S., Chowdhury, J., and Ganguly, T.: Mode of anchoring of zno nanoparticles to molecules having both cooh and nh functionalities. Journal of Molecular Structure, 964(1):9–17, 2010.

106. Soman, P., Darnell, M., Feldman, M. D., and Chen, S.: Growth of high-aspect ratio horizontally-aligned zno nanowire arrays. Journal of nanoscience and nanotechnology, 11(8):6880, August 2011.

107. Shi, P., Chen, H., Cho, M. R., and Stroscio, M. A.: Peptide-directed binding of quantum dots to integrins in human fibroblast. IEEE Transactions on NanoBioscience, 5(1):15–19, 2006.

108. The elk fp-lapw code. <http://elk.sourceforge.net/>.

109. Phillip W. Gibson, P. D., Lee, P. D. C., Ko, P. D. F., and Reneker, P. D. D.: Application of nanofiber technology to nonwoven thermal insulation. Journal of Engineered Fibers and Fabrics, 2(2):32–40, July 1 2007.

110. Moore, B. T. and Ferry, D. K.: Remote polar phonon scattering in si inversion layers. Journal of Applied Physics, 51(5):2603, 1980.

111. Sharma, S. and Ambrosch-Draxl, C.: Second-harmonic optical response from first principles. Physica Scripta, 2004:128, January 1 2004.

112. Osgood, J. R. M., Panoiu, N. C., Dadap, J. I., Liu, X., Chen, X., Hsieh, I.-W., Dulkeith, E., Green, W. M., and Vlasov, Y. A.: Engineering nonlinearities in nanoscale optical systems: physics and applications in dispersion-engineered silicon nanophotonic wires. Advances in Optics and Photonics, 1(1):162–235, January 1 2009.

113. Boyd, R. W.: Nonlinear Optics. Amsterdam, Acad. Press, 2. ed. edition, 2003.

114. Morse, P. M. and Feshbach, H.: Methods of theoretical physics. New York, McGraw-Hill.

115. Hodgkin, A. L. and Huxley, A. F.: A quantitative description of membrane current and its application to conduction and excitation in nerve. The Journal of Physiology, 117(4):500–544, August 28 1952.

116. Auld, B. A.: Acoustic fields and waves in solids. United States, 1990.

117. Hansen, O., Lavrinenko, A. V., Moulin, G., Andersen, K. N., Zsigri, B., Borel, P. I., Fage-Pedersen, J., Kristensen, M., Ou, H., Jacobsen, R. S., Peucheret, C., Frandsen, L. H., and Bjarklev, A.: Strained silicon as a new electro-optic material. Nature, 441(7090):199–202, May 11 2006.

APPENDICES

Appendix A

HIGHER ORDER SUSCEPTIBILITY TENSOR

A.1 Second order susceptibility tensor

In silicon, the second order term of the susceptibility tensor is zero due to the symmetry in the crystal structure. [112] However, when the symmetry condition breaks, (e.g. apply strain or on a curve surface) [117] the second order term can be considerably large compared to the third order term. In other words,

$$P_i^{Si} = P_i^s + \sum_{j=1}^{3} \epsilon_0 \chi_{ij}^{(1)} \mathcal{E}_j + \sum_{j,k=1}^{3} \epsilon_0 \chi_{ijk}^{(2)} \mathcal{E}_j \mathcal{E}_k \tag{A.1}$$

Theoretical calculation of the second order susceptibility ($\chi_{ijk}^{(2)}$ in Equation A.1) can be performed using TDDFT. [111] An open source TDDFT code, the Elk code, is used to calculate the second order susceptibility of silicon. Figure 34 shows the imaginary part of the second order susceptibility of silicon using 9 bands in valence of conduction bands. 2ω transitions indicate the second harmonic contribution either interband or intraband transitions. Near 2.51 eV, silicon exhibits strong plasmonic behavior (negative imaginary part of the susceptibility) from the second harmonic intraband transition, indicating possibility of optical applications in visible range.

Appendix A (Continued)

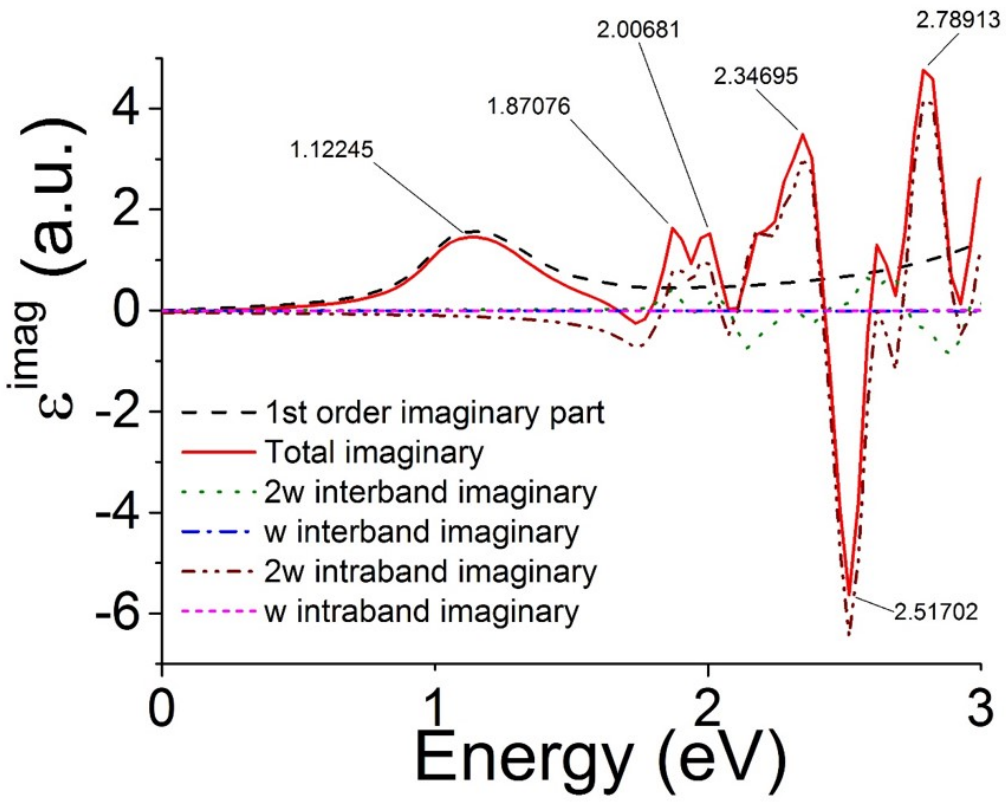

Figure 34: The imaginary part of second order susceptibility of silicon ω and 2ω represent single photon transition and second harmonic contribution, respectively.

Appendix A (Continued)

A.2 Third order susceptibility tensor

$$P_i = P_i^s + \sum_{j=1}^{3} \epsilon_0 \chi_{ij}^{(1)} \mathcal{E}_j + \sum_{j,k,l=1}^{3} \epsilon_0 \chi_{ijkl}^{(3)} \mathcal{E}_j \mathcal{E}_k \mathcal{E}_l \tag{A.2}$$

$$\begin{aligned}
P_x = P_x^s &+ \epsilon_0 \chi_{xx}^{(1)} \mathcal{E}_x && \text{(A.3)}\\
&+ \epsilon_0 \chi_{xxxx}^{(3)} \mathcal{E}_x \mathcal{E}_x \mathcal{E}_x + \epsilon_0 \chi_{xxxy}^{(3)} \mathcal{E}_x \mathcal{E}_x \mathcal{E}_y + \epsilon_0 \chi_{xxxz}^{(3)} \mathcal{E}_x \mathcal{E}_x \mathcal{E}_z && \text{(A.4)}\\
&+ \epsilon_0 \chi_{xxyx}^{(3)} \mathcal{E}_x \mathcal{E}_y \mathcal{E}_x + \epsilon_0 \chi_{xxyy}^{(3)} \mathcal{E}_x \mathcal{E}_y \mathcal{E}_y + \epsilon_0 \chi_{xxyz}^{(3)} \mathcal{E}_x \mathcal{E}_y \mathcal{E}_z && \text{(A.5)}\\
&+ \epsilon_0 \chi_{xxzx}^{(3)} \mathcal{E}_x \mathcal{E}_z \mathcal{E}_x + \epsilon_0 \chi_{xxzy}^{(3)} \mathcal{E}_x \mathcal{E}_z \mathcal{E}_y + \epsilon_0 \chi_{xxzz}^{(3)} \mathcal{E}_x \mathcal{E}_z \mathcal{E}_z && \text{(A.6)}\\
&+ \epsilon_0 \chi_{xyxx}^{(3)} \mathcal{E}_y \mathcal{E}_x \mathcal{E}_x + \epsilon_0 \chi_{xyxy}^{(3)} \mathcal{E}_y \mathcal{E}_x \mathcal{E}_y + \epsilon_0 \chi_{xyxz}^{(3)} \mathcal{E}_y \mathcal{E}_x \mathcal{E}_z && \text{(A.7)}\\
&+ \epsilon_0 \chi_{xyyx}^{(3)} \mathcal{E}_y \mathcal{E}_y \mathcal{E}_x + \epsilon_0 \chi_{xyyy}^{(3)} \mathcal{E}_y \mathcal{E}_y \mathcal{E}_y + \epsilon_0 \chi_{xyyz}^{(3)} \mathcal{E}_y \mathcal{E}_y \mathcal{E}_z && \text{(A.8)}\\
&+ \epsilon_0 \chi_{xyzx}^{(3)} \mathcal{E}_y \mathcal{E}_z \mathcal{E}_x + \epsilon_0 \chi_{xyzy}^{(3)} \mathcal{E}_y \mathcal{E}_z \mathcal{E}_y + \epsilon_0 \chi_{xyzz}^{(3)} \mathcal{E}_y \mathcal{E}_z \mathcal{E}_z && \text{(A.9)}\\
&+ \epsilon_0 \chi_{xzxx}^{(3)} \mathcal{E}_z \mathcal{E}_x \mathcal{E}_x + \epsilon_0 \chi_{xzxy}^{(3)} \mathcal{E}_z \mathcal{E}_x \mathcal{E}_y + \epsilon_0 \chi_{xzxz}^{(3)} \mathcal{E}_z \mathcal{E}_x \mathcal{E}_z && \text{(A.10)}\\
&+ \epsilon_0 \chi_{xzyx}^{(3)} \mathcal{E}_z \mathcal{E}_y \mathcal{E}_x + \epsilon_0 \chi_{xzyy}^{(3)} \mathcal{E}_z \mathcal{E}_y \mathcal{E}_y + \epsilon_0 \chi_{xzyz}^{(3)} \mathcal{E}_z \mathcal{E}_y \mathcal{E}_z && \text{(A.11)}\\
&+ \epsilon_0 \chi_{xzzx}^{(3)} \mathcal{E}_z \mathcal{E}_z \mathcal{E}_x + \epsilon_0 \chi_{xzzy}^{(3)} \mathcal{E}_z \mathcal{E}_z \mathcal{E}_y + \epsilon_0 \chi_{xzzz}^{(3)} \mathcal{E}_z \mathcal{E}_z \mathcal{E}_z && \text{(A.12)}\\
& && \text{(A.13)}
\end{aligned}$$

Appendix A (Continued)

$$
\begin{aligned}
P_y = P_y^s &+ \epsilon_0\chi_{yy}^{(1)}\mathcal{E}_y && \text{(A.14)}\\
&+ \epsilon_0\chi_{yxxx}^{(3)}\mathcal{E}_x\mathcal{E}_x\mathcal{E}_x + \epsilon_0\chi_{yxxy}^{(3)}\mathcal{E}_x\mathcal{E}_x\mathcal{E}_y + \epsilon_0\chi_{yxxz}^{(3)}\mathcal{E}_x\mathcal{E}_x\mathcal{E}_z && \text{(A.15)}\\
&+ \epsilon_0\chi_{yxyx}^{(3)}\mathcal{E}_x\mathcal{E}_y\mathcal{E}_x + \epsilon_0\chi_{yxyy}^{(3)}\mathcal{E}_x\mathcal{E}_y\mathcal{E}_y + \epsilon_0\chi_{yxyz}^{(3)}\mathcal{E}_x\mathcal{E}_y\mathcal{E}_z && \text{(A.16)}\\
&+ \epsilon_0\chi_{yxzx}^{(3)}\mathcal{E}_x\mathcal{E}_z\mathcal{E}_x + \epsilon_0\chi_{yxzy}^{(3)}\mathcal{E}_x\mathcal{E}_z\mathcal{E}_y + \epsilon_0\chi_{yxzz}^{(3)}\mathcal{E}_x\mathcal{E}_z\mathcal{E}_z && \text{(A.17)}\\
&+ \epsilon_0\chi_{yyxx}^{(3)}\mathcal{E}_y\mathcal{E}_x\mathcal{E}_x + \epsilon_0\chi_{yyxy}^{(3)}\mathcal{E}_y\mathcal{E}_x\mathcal{E}_y + \epsilon_0\chi_{yyxz}^{(3)}\mathcal{E}_y\mathcal{E}_x\mathcal{E}_z && \text{(A.18)}\\
&+ \epsilon_0\chi_{yyyx}^{(3)}\mathcal{E}_y\mathcal{E}_y\mathcal{E}_x + \epsilon_0\chi_{yyyy}^{(3)}\mathcal{E}_y\mathcal{E}_y\mathcal{E}_y + \epsilon_0\chi_{yyyz}^{(3)}\mathcal{E}_y\mathcal{E}_y\mathcal{E}_z && \text{(A.19)}\\
&+ \epsilon_0\chi_{yyzx}^{(3)}\mathcal{E}_y\mathcal{E}_z\mathcal{E}_x + \epsilon_0\chi_{yyzy}^{(3)}\mathcal{E}_y\mathcal{E}_z\mathcal{E}_y + \epsilon_0\chi_{yyzz}^{(3)}\mathcal{E}_y\mathcal{E}_z\mathcal{E}_z && \text{(A.20)}\\
&+ \epsilon_0\chi_{yzxx}^{(3)}\mathcal{E}_z\mathcal{E}_x\mathcal{E}_x + \epsilon_0\chi_{yzxy}^{(3)}\mathcal{E}_z\mathcal{E}_x\mathcal{E}_y + \epsilon_0\chi_{yzxz}^{(3)}\mathcal{E}_z\mathcal{E}_x\mathcal{E}_z && \text{(A.21)}\\
&+ \epsilon_0\chi_{yzyx}^{(3)}\mathcal{E}_z\mathcal{E}_y\mathcal{E}_x + \epsilon_0\chi_{yzyy}^{(3)}\mathcal{E}_z\mathcal{E}_y\mathcal{E}_y + \epsilon_0\chi_{yzyz}^{(3)}\mathcal{E}_z\mathcal{E}_y\mathcal{E}_z && \text{(A.22)}\\
&+ \epsilon_0\chi_{yzzx}^{(3)}\mathcal{E}_z\mathcal{E}_z\mathcal{E}_x + \epsilon_0\chi_{yzzy}^{(3)}\mathcal{E}_z\mathcal{E}_z\mathcal{E}_y + \epsilon_0\chi_{yzzz}^{(3)}\mathcal{E}_z\mathcal{E}_z\mathcal{E}_z && \text{(A.23)}\\
& && \text{(A.24)}
\end{aligned}
$$

Appendix A (Continued)

$$P_z = P_z^s + \epsilon_0\chi_{zz}^{(1)}\mathcal{E}_z \tag{A.25}$$

$$+ \epsilon_0\chi_{zxxx}^{(3)}\mathcal{E}_x\mathcal{E}_x\mathcal{E}_x + \epsilon_0\chi_{zxxy}^{(3)}\mathcal{E}_x\mathcal{E}_x\mathcal{E}_y + \epsilon_0\chi_{zxxz}^{(3)}\mathcal{E}_x\mathcal{E}_x\mathcal{E}_z \tag{A.26}$$

$$+ \epsilon_0\chi_{zxyx}^{(3)}\mathcal{E}_x\mathcal{E}_y\mathcal{E}_x + \epsilon_0\chi_{zxyy}^{(3)}\mathcal{E}_x\mathcal{E}_y\mathcal{E}_y + \epsilon_0\chi_{zxyz}^{(3)}\mathcal{E}_x\mathcal{E}_y\mathcal{E}_z \tag{A.27}$$

$$+ \epsilon_0\chi_{zxzx}^{(3)}\mathcal{E}_x\mathcal{E}_z\mathcal{E}_x + \epsilon_0\chi_{zxzy}^{(3)}\mathcal{E}_x\mathcal{E}_z\mathcal{E}_y + \epsilon_0\chi_{zxzz}^{(3)}\mathcal{E}_x\mathcal{E}_z\mathcal{E}_z \tag{A.28}$$

$$+ \epsilon_0\chi_{zyxx}^{(3)}\mathcal{E}_y\mathcal{E}_x\mathcal{E}_x + \epsilon_0\chi_{zyxy}^{(3)}\mathcal{E}_y\mathcal{E}_x\mathcal{E}_y + \epsilon_0\chi_{zyxz}^{(3)}\mathcal{E}_y\mathcal{E}_x\mathcal{E}_z \tag{A.29}$$

$$+ \epsilon_0\chi_{zyyx}^{(3)}\mathcal{E}_y\mathcal{E}_y\mathcal{E}_x + \epsilon_0\chi_{zyyy}^{(3)}\mathcal{E}_y\mathcal{E}_y\mathcal{E}_y + \epsilon_0\chi_{zyyz}^{(3)}\mathcal{E}_y\mathcal{E}_y\mathcal{E}_z \tag{A.30}$$

$$+ \epsilon_0\chi_{zyzx}^{(3)}\mathcal{E}_y\mathcal{E}_z\mathcal{E}_x + \epsilon_0\chi_{zyzy}^{(3)}\mathcal{E}_y\mathcal{E}_z\mathcal{E}_y + \epsilon_0\chi_{zyzz}^{(3)}\mathcal{E}_y\mathcal{E}_z\mathcal{E}_z \tag{A.31}$$

$$+ \epsilon_0\chi_{zzxx}^{(3)}\mathcal{E}_z\mathcal{E}_x\mathcal{E}_x + \epsilon_0\chi_{zzxy}^{(3)}\mathcal{E}_z\mathcal{E}_x\mathcal{E}_y + \epsilon_0\chi_{zzxz}^{(3)}\mathcal{E}_z\mathcal{E}_x\mathcal{E}_z \tag{A.32}$$

$$+ \epsilon_0\chi_{zzyx}^{(3)}\mathcal{E}_z\mathcal{E}_y\mathcal{E}_x + \epsilon_0\chi_{zzyy}^{(3)}\mathcal{E}_z\mathcal{E}_y\mathcal{E}_y + \epsilon_0\chi_{zzyz}^{(3)}\mathcal{E}_z\mathcal{E}_y\mathcal{E}_z \tag{A.33}$$

$$+ \epsilon_0\chi_{zzzx}^{(3)}\mathcal{E}_z\mathcal{E}_z\mathcal{E}_x + \epsilon_0\chi_{zzzy}^{(3)}\mathcal{E}_z\mathcal{E}_z\mathcal{E}_y + \epsilon_0\chi_{zzzz}^{(3)}\mathcal{E}_z\mathcal{E}_z\mathcal{E}_z \tag{A.34}$$

$$\tag{A.35}$$

For the m3m crystal class, there are 21 nonvanishing compoments: [113]

$$\chi_{xxxx}^{(3)} = \chi_{yyyy}^{(3)} = \chi_{zzzz}^{(3)}, \tag{A.36}$$

$$\chi_{yyzz}^{(3)} = \chi_{zzyy}^{(3)} = \chi_{zzxx}^{(3)} = \chi_{xxzz}^{(3)} = \chi_{xxyy}^{(3)} = \chi_{yyxx}^{(3)}, \tag{A.37}$$

$$\chi_{yzyz}^{(3)} = \chi_{zyzy}^{(3)} = \chi_{zxzx}^{(3)} = \chi_{xzxz}^{(3)} = \chi_{xyxy}^{(3)} = \chi_{yxyx}^{(3)}, \tag{A.38}$$

$$\chi_{yzzy}^{(3)} = \chi_{zyyz}^{(3)} = \chi_{zxxz}^{(3)} = \chi_{xzzx}^{(3)} = \chi_{xyyx}^{(3)} = \chi_{yxxy}^{(3)}. \tag{A.39}$$

Appendix A (Continued)

So,

$$P_x = P_x^s + \epsilon_0\chi_{xx}^{(1)}\mathcal{E}_x \tag{A.40}$$

$$+ \epsilon_0\chi_{xxxx}^{(3)}\mathcal{E}_x\mathcal{E}_x\mathcal{E}_x \tag{A.41}$$

$$+ \epsilon_0\chi_{xxyy}^{(3)}\mathcal{E}_x\mathcal{E}_y\mathcal{E}_y + \epsilon_0\chi_{xxzz}^{(3)}\mathcal{E}_x\mathcal{E}_z\mathcal{E}_z \tag{A.42}$$

$$+ \epsilon_0\chi_{xyxy}^{(3)}\mathcal{E}_y\mathcal{E}_x\mathcal{E}_y + \epsilon_0\chi_{xzxz}^{(3)}\mathcal{E}_z\mathcal{E}_x\mathcal{E}_z \tag{A.43}$$

$$+ \epsilon_0\chi_{xyyx}^{(3)}\mathcal{E}_y\mathcal{E}_y\mathcal{E}_x + \epsilon_0\chi_{xzzx}^{(3)}\mathcal{E}_z\mathcal{E}_z\mathcal{E}_x \tag{A.44}$$

$$P_y = P_y^s + \epsilon_0\chi_{yy}^{(1)}\mathcal{E}_y \tag{A.45}$$

$$+ \epsilon_0\chi_{yyyy}^{(3)}\mathcal{E}_y\mathcal{E}_y\mathcal{E}_y \tag{A.46}$$

$$+ \epsilon_0\chi_{yyxx}^{(3)}\mathcal{E}_y\mathcal{E}_x\mathcal{E}_x + \epsilon_0\chi_{yyzz}^{(3)}\mathcal{E}_y\mathcal{E}_z\mathcal{E}_z \tag{A.47}$$

$$+ \epsilon_0\chi_{yxyx}^{(3)}\mathcal{E}_x\mathcal{E}_y\mathcal{E}_x + \epsilon_0\chi_{yzyz}^{(3)}\mathcal{E}_z\mathcal{E}_y\mathcal{E}_z \tag{A.48}$$

$$+ \epsilon_0\chi_{yxxy}^{(3)}\mathcal{E}_x\mathcal{E}_x\mathcal{E}_y + \epsilon_0\chi_{yzzy}^{(3)}\mathcal{E}_z\mathcal{E}_z\mathcal{E}_y \tag{A.49}$$

$$\tag{A.50}$$

Appendix A (Continued)

$$
\begin{aligned}
P_z = P_z^s &+ \epsilon_0 \chi_{zz}^{(1)} \mathcal{E}_z && \text{(A.51)}\\
&+ \epsilon_0 \chi_{zzzz}^{(3)} \mathcal{E}_z \mathcal{E}_z \mathcal{E}_z && \text{(A.52)}\\
&+ \epsilon_0 \chi_{zzxx}^{(3)} \mathcal{E}_z \mathcal{E}_x \mathcal{E}_x + \epsilon_0 \chi_{zzyy}^{(3)} \mathcal{E}_z \mathcal{E}_y \mathcal{E}_y && \text{(A.53)}\\
&+ \epsilon_0 \chi_{zxzx}^{(3)} \mathcal{E}_x \mathcal{E}_z \mathcal{E}_x + \epsilon_0 \chi_{zyzy}^{(3)} \mathcal{E}_y \mathcal{E}_z \mathcal{E}_y && \text{(A.54)}\\
&+ \epsilon_0 \chi_{zxxz}^{(3)} \mathcal{E}_x \mathcal{E}_x \mathcal{E}_z + \epsilon_0 \chi_{zyyz}^{(3)} \mathcal{E}_y \mathcal{E}_y \mathcal{E}_z && \text{(A.55)}\\
& && \text{(A.56)}
\end{aligned}
$$

which can be reduced with 4 independent components, $\chi_{xxxx}^{(3)}, \chi_{xxyy}^{(3)}, \chi_{xyxy}^{(3)}, \chi_{xyyx}^{(3)}$. Further simplification can be achieved with symmetry conderations [112], $\chi_{xxyy}^{(3)} = \chi_{xyyx}^{(3)}$. Finally with Kleinman symmetry relations, $\chi_{xxyy}^{(3)} = \chi_{xyxy}^{(3)}$, the optical polarization can be described as follows

$$
\begin{aligned}
P_x &= P_x^s + \epsilon_0 \chi_{xx}^{(1)} \mathcal{E}_x + \epsilon_0 \chi_{xxxx}^{(3)} \mathcal{E}_x \mathcal{E}_x \mathcal{E}_x + 6\epsilon_0 \chi_{xxyy}^{(3)} \mathcal{E}_x \mathcal{E}_y \mathcal{E}_y && \text{(A.57)}\\
P_y &= P_y^s + \epsilon_0 \chi_{yy}^{(1)} \mathcal{E}_y + \epsilon_0 \chi_{xxxx}^{(3)} \mathcal{E}_y \mathcal{E}_y \mathcal{E}_y + 6\epsilon_0 \chi_{xxyy}^{(3)} \mathcal{E}_y \mathcal{E}_x \mathcal{E}_x && \text{(A.58)}\\
P_z &= P_z^s + \epsilon_0 \chi_{zz}^{(1)} \mathcal{E}_z + \epsilon_0 \chi_{xxxx}^{(3)} \mathcal{E}_z \mathcal{E}_z \mathcal{E}_z + 6\epsilon_0 \chi_{xxyy}^{(3)} \mathcal{E}_z \mathcal{E}_x \mathcal{E}_x && \text{(A.59)}
\end{aligned}
$$

Appendix A (Continued)

A.3 Tensor Transformation

Coordinate transformation matrix from Cartesian coordinates to cylindrical coordinates is given by [114, 116]

$$[a] = \begin{bmatrix} \cos(\phi) & \sin(\phi) & 0 \\ -\sin(\phi) & \cos(\phi) & 0 \\ 0 & 0 & 1 \end{bmatrix}. \tag{A.60}$$

And the transform can be done through the following relation [114, 116]

$$[\chi'] = [a][\chi][a]^{-1} \tag{A.61}$$

For a complete susceptibility tensor,

$$[\chi] = \begin{bmatrix} \chi_{xx} & \chi_{xy} & \chi_{xz} \\ \chi_{yx} & \chi_{yy} & \chi_{yz} \\ \chi_{zx} & \chi_{zy} & \chi_{zz} \end{bmatrix}, \tag{A.62}$$

Appendix A (Continued)

it can be described in cylindrical coordiantes by

$$[\chi_{cyl}] = \begin{bmatrix} \chi_{\rho\rho} & \chi_{\rho\phi} & \chi_{\rho z} \\ \chi_{\phi\rho} & \chi_{\phi\phi} & \chi_{\phi z} \\ \chi_{z\rho} & \chi_{z\phi} & \chi_{zz} \end{bmatrix} \tag{A.63}$$

$$= [a][\chi_{cartesian}][a]^{-1} \tag{A.64}$$

$$= \begin{bmatrix} \cos(\phi) & \sin(\phi) & 0 \\ -\sin(\phi) & \cos(\phi) & 0 \\ 0 & 0 & 1 \end{bmatrix} \begin{bmatrix} \chi_{xx} & \chi_{xy} & \chi_{xz} \\ \chi_{yx} & \chi_{yy} & \chi_{yz} \\ \chi_{zx} & \chi_{zy} & \chi_{zz} \end{bmatrix} \begin{bmatrix} \cos(\phi) & -\sin(\phi) & 0 \\ \sin(\phi) & \cos(\phi) & 0 \\ 0 & 0 & 1 \end{bmatrix} \tag{A.65}$$

$$= \begin{bmatrix} \cos(\phi)\left(\chi_{xx}\cos(\phi)+\chi_{yx}\sin(\phi)\right)+\sin(\phi)\left(\chi_{xy}\cos(\phi)+\chi_{yy}\sin(\phi)\right) & \cos(\phi)\left(\chi_{xy}\cos(\phi)+\chi_{yy}\sin(\phi)\right)-\sin(\phi)\left(\chi_{xx}\cos(\phi)+\chi_{yx}\sin(\phi)\right) & \chi_{xz}\cos(\phi)+\chi_{yz}\sin(\phi) \\ \cos(\phi)\left(\chi_{yx}\cos(\phi)-\chi_{xx}\sin(\phi)\right)+\sin(\phi)\left(\chi_{yy}\cos(\phi)-\chi_{xy}\sin(\phi)\right) & \cos(\phi)\left(\chi_{yy}\cos(\phi)-\chi_{xy}\sin(\phi)\right)-\sin(\phi)\left(\chi_{yx}\cos(\phi)-\chi_{xx}\sin(\phi)\right) & \chi_{yz}\cos(\phi)-\chi_{xz}\sin(\phi) \\ \chi_{zy}\sin(\phi)+\chi_{zx}\cos(\phi) & \chi_{zy}\cos(\phi)-\chi_{zx}\sin(\phi) & \chi_{zz} \end{bmatrix} \tag{A.66}$$

If off-diagonal components (e.g.χ_{xy}, χ_{zy} etc.) can be neglected, $[\chi_{cyl}]$ becomes

$$\begin{bmatrix} \chi_{xx}\cos^2(\phi)+\chi_{yy}\sin^2(\phi) & \cos(\phi)\chi_{yy}\sin(\phi)-\sin(\phi)\chi_{xx}\cos(\phi) & 0 \\ -\cos(\phi)\chi_{xx}\sin(\phi)+\sin(\phi)\chi_{yy}\cos(\phi) & \chi_{yy}\cos^2(\phi)+\chi_{xx}\sin^2(\phi) & 0 \\ 0 & 0 & \chi_{zz} \end{bmatrix} \tag{A.67}$$

Appendix A (Continued)

Also, when $\chi_{xx} = \chi_{yy} = \chi_{zz}$, which is usually the case for diamond crystals,

$$[\chi_{cyl}] = \begin{bmatrix} \chi_{xx} & 0 & 0 \\ 0 & \chi_{xx} & 0 \\ 0 & 0 & \chi_{xx} \end{bmatrix} \tag{A.68}$$

$$= \begin{bmatrix} \chi_{\rho\rho} & 0 & 0 \\ 0 & \chi_{\phi\phi} & 0 \\ 0 & 0 & \chi_{zz} \end{bmatrix}, \tag{A.69}$$

which lead to a conclusion: $\chi_{\rho\rho} = \chi_{\phi\phi} = \chi_{zz} = \chi_{xx}$

In the meanwhile, if $\chi_{xx} = \chi_{yy} = \chi_{zz} = \chi_{diag}$ and $\chi_{xy} = \chi_{yx} = \chi_{xz} = \chi_{zx} = \chi_{yz} = \chi_{zy} = \chi_{od}$,

$$[\chi_{cyl}] = \begin{bmatrix} \chi_{diag} + 2\chi_{od}\sin(\phi)\cos(\phi) & \chi_{od}\left[\cos^2(\phi) - \sin^2(\phi)\right] & \chi_{od}\left[\cos(\phi) + \sin(\phi)\right] \\ \chi_{od}\left[\cos^2(\phi) - \sin^2(\phi)\right] & \chi_{diag} - 2\chi_{od}\sin(\phi)\cos(\phi) & \chi_{od}\left[\cos(\phi) - \sin(\phi)\right] \\ \chi_{od}\left[\cos(\phi) + \sin(\phi)\right] & \chi_{od}\left[\cos(\phi) - \sin(\phi)\right] & \chi_{diag} \end{bmatrix} \tag{A.70}$$

Appendix B

COMPUTER CODES

B.1 MEEP

All simulations regarding electromagnetic enhancements, LDOS, SCS, and purcell factors were performed with the finite-difference time-domain (FDTD) method [12], using a freely available software package, MEEP. [16]

B.1.1 Typical input file used for LDOS calculation

```
; Calculating 2d ring-resonator modes using cylindrical coordinates,
; around silicon nanowire
; a=1e-8m or 10nm
; what this means is that all the dimensions should be multipled by a to get the real
    dimensions. The frequency can be converted to real wavelength: longer_lamda_in_nm=
    a_in_nm/fmin and shorter_lamda_in_nm=a_in_nm/fmax, where fmin=fcen-df/2 and fmax=
    fcen+df/2
; Modified by Min Choi
; 071313_1
; Original source is from Bala's Website (http://juluribk.com/tag/meep/)


(define-param nSi 3.45) ; index of silicon
(define-param nSiO2 1.46) ; index of SiO2
```

Appendix B (Continued)

```
(define-param wSiO2 0.5) ; width of SiO2

(define-param wAg 10) ; width of silver

(define-param rSi 3.5) ; inner radius of silver cavity (radius of silicon NW)

(define wglass (* 2 (+ rSi wSiO2 wAg)))

(define hglass (+ wSiO2 wAg))


(define-param pad 20) ; padding between waveguide and edge of PML

(define-param dpml 5) ; thickness of PML


(define sr (* 2 (+ rSi wSiO2 wAg pad dpml))) ; cell size

(define Si (make medium (index nSi))) ; define silicon

(define SiO2 (make medium (index nSiO2))) ; define silicon

(define Ag (make dielectric (epsilon 1.0001)

       (polarizations

       (make polarizability

       (omega 1e-20) (gamma 0.0038715) (sigma 4.4625e+39))

       (make polarizability

       (omega 0.065815) (gamma 0.31343) (sigma 7.9247))

       (make polarizability

       (omega 0.36142) (gamma 0.036456) (sigma 0.50133))

       (make polarizability

       (omega 0.66017) (gamma 0.0052426) (sigma 0.013329))

       (make polarizability
```

Appendix B (Continued)

```
       (omega 0.73259) (gamma 0.07388) (sigma 0.82655))
       (make polarizability
       (omega 1.6365) (gamma 0.19511) (sigma 1.1133)))))
(set! geometry-lattice (make lattice (size sr sr no-size)))

(set! geometry (list
               (make cylinder (center 0 0) (height infinity) (radius (+ rSi wSiO2 wAg)
                   ) (material Ag))
               (make cylinder (center 0 0) (height infinity) (radius (+ rSi wSiO2)) (
                   material SiO2))
               (make cylinder (center 0 0) (height infinity) (radius rSi) (material Si
                   ))
               (make block (center 0 (* -1 (+ rSi (/ hglass 2))) 0) (size wglass
                   hglass infinity) (material SiO2))))

(set! pml-layers (list (make pml (thickness dpml))))
(set-param! resolution 50)

; If we don't want to excite a specific mode symmetry, we can just
; put a single point source at some arbitrary place, pointing in some
; arbitrary direction. We will only look for TM modes (E out of the plane).
```

Appendix B (Continued)

```
;(define-param fcen 0.12815) ; pulse center frequency (8.43E14 Hz, 355.7nm Ti:Sapphire
    laser)
(define-param fcen 0.09949) ; pulse center frequency (6.55E14 Hz, 457.9nm Ar+ laser)
(define-param df 0.1) ; pulse width (in frequency)
(set! sources (list
              (make source
                (src (make gaussian-src (frequency fcen) (fwidth df)))
                (component Ez) (center 0 0))))

; exploit the mirror symmetry in structure+source:
(set! symmetries (list (make mirror-sym (direction Y))))

(define-param Th 750)
(define-param fmin 0.004744438) ;equivalant to 1.7 eV
(define-param fmax 0.002987239) ;equivalant to 2.7 eV
(run-sources+ Th
             (at-beginning output-epsilon)
             (after-sources (harminv Ez (vector3 0) fcen df))
             (dft-ldos fmin fmax 100))
;(define f (harminv-freq-re (car harminv-results)))
;(define Q (harminv-Q (car harminv-results)))
;(define Vmode (* 0.25 wAg wAg))
;(print "ldos0:, " (/ Q Vmode (* 2 pi f pi 0.5)))
```

Appendix B (Continued)

```
;(reset-meep)

;(define-param T (* 2 Q (/ f)))

;(run-sources+ Th (dft-ldos fmin fmax 50))
```

B.2 General Utility Lattice Program

Phonon dispersion relation of bulk silicon was calculated using free available code, General Utility Lattice Program (GULP). [30] The detailed description of the code can be found in

B.2.1 Typical input file used to calculate silicon phonon dispersion

```
opti conp dist full nosym prop phon noden defe

cutd 3.0

cell

5.4 5.4 5.4 90 90 90

frac

Si core 0.00 0.00 0.00

Si core 0.25 0.25 0.25

space

216

# NB The space group for Si is 227, but this group also works


centre 0.0 0.0 0.0

size 4.0 10.0

vaca Si 0.0 0.0 0.0
```

Appendix B (Continued)

```
botwobody
Si core Si core 1830.8 471.18 2.4799 1.7322 2.70 3.00
borepulsive
Si core Si core 0.0 3 0.78734 1.7322 2.70 3.00
boattractive theta
Si core Si core 0.0000010999 3 0.78734 1.7322 100390.0 16.218 -0.59826 2.70 3.00
dispersion
0.0 0.0 0.0 to 0.75 0.0 0.75
output phon gammatok
```

B.3 Elk FP-LAPW Code

The wavevector and wavelength depedent dielectric function of silicon and the nonlinear second order dielectric function of silicon were calculated using the Elk FP-LAPW Code. [108]

B.3.1 Input files

```
tasks
  0        ! ground-state calculation
  120
  125
  188


!  120      ! compute momentum matrix elements
!  121      ! compute RPA dielectric function with no local field contributions
```

Appendix B (Continued)

```
!  180      ! generate RPA dielectric function with local field contributions

!  185      ! write the BSE Hamiltonian matrix to file

!  186      ! diagonalise the BSE matrix

!  187      ! compute BSE dielectric function

! this should be small (but not so small that it affects the results!) for a

! fast calculation because the wavefunctions used in the construction of the BSE

! matrix elements are expanded to this angular momentum cut-off

lmaxvr

  4


! number of valence states to use in BSE Hamiltonian

nvbse

  3


! number of conduction states

ncbse

  4


! use smallest possible maximum |G|

gmaxvr

  0.0


! a scissor correction is required to match the gap to experiment
```

Appendix B (Continued)

```
scissor
  0.0331


swidth
  0.005


wplot
  800 100 0 : nwplot, ngrkf, nswplot
  0.0 1.0  : wplot


avec
  5.13 5.13 0.00
  5.13 0.00 5.13
  0.00 5.13 5.13


sppath
  '../../species/'


atoms
  1                              : nspecies
 'Si.in'                         : spfname
  2                              : natoms
  0.0 0.0 0.0    0.0 0.0 0.0     : atposl, bfcmt
```

Appendix B (Continued)

```
  0.25 0.25 0.25  0.0 0.0 0.0


ngridk
  16  16  16


vkloff
  0.25  0.5  0.625


vecql
  0.25 0.25 0.25
```

B.4 Power Absorption Rate in plasmonic Ag-SiO_2-Si nano-structure

```
clear all;
close all;


hbar=6.58211928*10^-16; % eV-s
eps0=8.854188*10^-12; % F/m
mu0=1.236637*10^-6; % m Kg S^-2 A^-2
au_to_si=5.8300348177*10^(-8)*4*pi/30000;
resl=1*10^3;


E0=zeros(1,resl);
for ii=1:resl
    if (ii==400)
```

Appendix B (Continued)

```
        E0(ii)=7.3998e03; % 250kW/cm^2=I=c*eps0*n*|E|^2/2
    end
end
h=2.5*10^-9; % m
dy=1*10^-4; % m
dx=1*10^-4; % m
qz=linspace(0,0.5,resl);

ph_energy_sample=linspace(0,27.211,800);
%Parse wavevector- and frequency-dependent dielectric function here

lambda=linspace(0.25*10^-6,1.45*10^-6,resl);
c=299792458; % speed of light (m/s)
eps_inf=3.56;
gamma=21*10^-3/hbar; %hbar*gamma = 21 meV
omega_p=9.15/hbar; %hbar*omega_p = 9.15 eV

omega=2*pi*c./fliplr(lambda);
ph_energy=hbar*omega;

%Green,  Self -consistent optical parameters of intrinsic silicon at 300 K including
    temperature coefficients silicon property Solar Energy Materials & Solar Cells 92
    (2008) 1305-1310
```

Appendix B (Continued)

```
sample_lambda=0.25*10^-6:0.01*10^-6:1.45*10^-6;
sample_energy=hbar*2*pi*c./fliplr(sample_lambda);
n=[1.665 1.757 2.068 2.959 4.356 4.976 5.121 5.112 5.195 5.301 5.494 6.026 6.891 6.616
     6.039 5.613 5.33 5.119 4.949 4.812 4.691 4.587 4.497 4.419 4.35 4.294 4.241 4.193
     4.151 4.112 4.077 4.045 4.015 3.988 3.963 3.94 3.918 3.898 3.879 3.861 3.844
    3.828 3.813 3.798 3.784 3.772 3.759 3.748 3.737 3.727 3.717 3.708 3.699 3.691
    3.683 3.675 3.668 3.661 3.654 3.647 3.641 3.635 3.63 3.624 3.619 3.614 3.609 3.604
     3.6 3.595 3.591 3.587 3.583 3.579 3.575 3.572 3.568 3.565 3.562 3.559 3.556 3.553
     3.55 3.547 3.545 3.542 3.54 3.537 3.535 3.532 3.53 3.528 3.526 3.524 3.522 3.52
    3.518 3.517 3.515 3.513 3.511 3.509 3.508 3.506 3.505 3.503 3.502 3.5 3.499 3.497
    3.496 3.495 3.494 3.492 3.491 3.49 3.489 3.488 3.487 3.486 3.485];
k=[3.665 4.084 4.68 5.287 5.286 4.234 3.598 3.303 3.1 2.977 2.938 2.966 2.171 0.946
    0.445 0.296 0.227 0.176 0.138 0.107 0.086 0.071 0.062 0.055 0.049 0.044 0.039
    0.036 0.033 0.03 0.028 0.026 0.024 0.023 0.021 0.02 0.018 0.017 0.016 0.015 0.014
    0.013 0.013 0.012 0.011 0.011 0.01 0.01 0.009 0.008 0.008 0.007 0.007 0.006 0.006
    0.005 0.005 0.005 0.004 0.004 0.004 0.003 0.003 0.003 0.002 0.002 0.002 0.002
    0.002 0.001 0.001 0.001 0.001 0.001 0.001 0.001 0 0 0 0 0 0 0 0 0 0 0 0 0 0 0 0 0
    0 0 0 0 0 0 0 0 0 0 0 0 0 0 0 0 0 0 0 0 0 0 0 0 0 0 0 0 0 0 0 0 0 0 0 0 0 0 0 0];

epsq1=interp1(ph_energy_sample(26:146),eps_DFTq1(26:146),linspace(ph_energy_sample(26)
    ,ph_energy_sample(146),resl),'PCHIP');
epsq2=interp1(ph_energy_sample(26:146),eps_DFTq2(26:146),linspace(ph_energy_sample(26)
    ,ph_energy_sample(146),resl),'PCHIP');
```

Appendix B (Continued)

```
epsq3=interp1(ph_energy_sample(26:146),eps_DFTq3(26:146),linspace(ph_energy_sample(26)
    ,ph_energy_sample(146),resl),'PCHIP');
epsq4=interp1(ph_energy_sample(26:146),eps_DFTq4(26:146),linspace(ph_energy_sample(26)
    ,ph_energy_sample(146),resl),'PCHIP');
epsq5=interp1(ph_energy_sample(26:146),eps_DFTq5(26:146),linspace(ph_energy_sample(26)
    ,ph_energy_sample(146),resl),'PCHIP');


epsq1_im=interp1(ph_energy_sample(26:146),eps_DFTq1_im(26:146),linspace(
    ph_energy_sample(26),ph_energy_sample(146),resl),'PCHIP');
epsq2_im=interp1(ph_energy_sample(26:146),eps_DFTq2_im(26:146),linspace(
    ph_energy_sample(26),ph_energy_sample(146),resl),'PCHIP');
epsq3_im=interp1(ph_energy_sample(26:146),eps_DFTq3_im(26:146),linspace(
    ph_energy_sample(26),ph_energy_sample(146),resl),'PCHIP');
epsq4_im=interp1(ph_energy_sample(26:146),eps_DFTq4_im(26:146),linspace(
    ph_energy_sample(26),ph_energy_sample(146),resl),'PCHIP');
epsq5_im=interp1(ph_energy_sample(26:146),eps_DFTq5_im(26:146),linspace(
    ph_energy_sample(26),ph_energy_sample(146),resl),'PCHIP');
clear eps_DFTq1 eps_DFTq2 eps_DFTq3 eps_DFTq4 eps_DFTq5 eps_DFTq1_im eps_DFTq2_im
    eps_DFTq3_im eps_DFTq4_im eps_DFTq5_im;


epsqw_re=([epsq1;epsq2;epsq3;epsq4;epsq5]);
epsqw_im=([epsq1_im;epsq2_im;epsq3_im;epsq4_im;epsq5_im]);
epsqw_re=interp1([0;0.125;0.25;0.375;0.5],epsqw_re,qz,'pchip');
```

Appendix B (Continued)

```
epsqw_im=interp1([0;0.125;0.25;0.375;0.5],epsqw_im,qz,'pchip');
clear epsq1 epsq2 epsq3 epsq4 epsq5 epsq1_im epsq2_im epsq3_im epsq4_im epsq5_im;


omega=2*pi*c./lambda;
ph_energy=hbar*omega;
eps3_re=epsqw_re(1,:);
eps3_im=epsqw_im(1,:);
eps3=(eps3_re+1j*eps3_im);


[epsilon_Ag_Re,epsilon_Ag_Im] = LD(lambda,'Ag','LD');
eps1=(fliplr(epsilon_Ag_Re)+1i*fliplr(epsilon_Ag_Im));
eps2=zeros(1,resl);
for i=1:resl
    eps2(i)=3.9;
end
k0=omega/c;


Sbeta=zeros(1,resl);
SbzAg=zeros(1,resl);
SbzSiO2=zeros(1,resl);
SbzSi=zeros(1,resl);
for i=1:resl
    clear betax bzSi bzSiO2 bzAg temp;
```

Appendix B (Continued)

```
    syms betax bzSi bzSiO2 bzAg;
    temp=vpasolve([eps1(i)*omega(i)^2*mu0*eps0-betax^2==bzAg^2, eps2(i)*omega(i)^2*mu0
        *eps0-betax^2==bzSiO2^2, eps3(i)*omega(i)^2*mu0*eps0-betax^2==bzSi^2, -1*(
        bzSiO2/eps2(i))*tan(bzSiO2*h)==(bzSi/eps3(i))], [betax bzSi bzSiO2 bzAg]);
    Sbeta(i)=temp.betax(1);
    SbzSi(i)=temp.bzSi(1);
    SbzAg(i)=temp.bzAg(1);
    SbzSiO2(i)=temp.bzSiO2(1);
end



% Electric field
zsi=linspace(h,10^(-7),resl);
zsio2=linspace(-h,h,resl);
zag=linspace(-10^(-7),-h,resl);

Ez_ag=zeros(resl,resl);
Ez_sio2=zeros(resl,resl);
Ez_si=zeros(resl,resl);
Ex_si=zeros(resl,resl);
Ex_sio2=zeros(resl,resl);
Ex_ag=zeros(resl,resl);
```

Appendix B (Continued)

```
E0_Ag=-E0.*SbzSi./SbzAg.*exp((SbzAg-SbzSi)*h);
E0_SiO2=E0.*SbzSi./SbzSiO2.*exp(-SbzSi*h).*(1./sin(SbzSiO2*h));


for ii=1:resl
    Ez_si(ii,:)=E0(ii)*(Sbeta(ii)*SbzSi(ii))/(omega(ii)*mu0*(eps3(ii))*eps0)*exp(-1*
        SbzSi(ii)*zsi);
    Ez_sio2(ii,:)=-1*E0_SiO2(ii)*(Sbeta(ii)*SbzSiO2(ii))/(omega(ii)*mu0*(eps2(ii))*
        eps0)*cos(SbzSiO2(ii)*zsi);
    Ez_ag(ii,:)=E0_Ag(ii)*(Sbeta(ii)*SbzAg(ii))/(omega(ii)*mu0*(eps1(ii))*eps0)*exp(
        SbzAg(ii)*zsi);


    Ex_si(ii,:)=-1i*E0(ii)*(SbzSi(ii)^2-Sbeta(ii)^2)/(omega(ii)*mu0*(eps3(ii))*eps0)*
        exp(-1*SbzSi(ii)*zsi);
    Ex_sio2(ii,:)=-1i*E0_SiO2(ii)*(SbzSiO2(ii)^2-Sbeta(ii)^2)/(omega(ii)*mu0*(eps2(ii)
        )*eps0)*cos(SbzSiO2(ii)*zsi);
    Ex_ag(ii,:)=-1i*E0_Ag(ii)*(SbzAg(ii)^2-Sbeta(ii)^2)/(omega(ii)*mu0*(eps1(ii))*eps0
        )*exp(SbzAg(ii)*zsi);
end
Ez_ft = fftshift(abs(ifft(abs(Ez_si))));
Ex_ft = fftshift(abs(ifft(abs(Ex_si))));


integrand_Exsi=zeros(resl,resl);
integrand_Ezsi=zeros(resl,resl);
```

Appendix B (Continued)

```
for i=1:resl

    temp=(1j*epsqw_im(:,i));

    integrand_Exsi(:,i)=(temp*Ex_ft(i)*conj(Ex_ft(i)));

    integrand_Ezsi(:,i)=(temp*Ez_ft(i)*conj(Ez_ft(i)));

end

integrand=(integrand_Exsi+integrand_Ezsi);


P_abs=omega*eps0./(4*pi.*imag(Sbeta)).*trapz(integrand);

P_abs(1442/2:resl)=0;
```

B.5 Scattering rate of LO and acoustic phonon and electrons

```
clear all;

% Define constants

e=1; % in atominc unit = 1.602176565E-19 C

k_b=8.6173324E-5; % in eV/K = 1.3806488E-23 J/K

h_bar=1; % in atominc unit = 1.054571726E-34 Js

m=1; % in atominc unit = 9.10938291E-31 kg

T=300; % K


% define parameters

V_p=762.3; % atomic unit. = 112.98 angstrom^3

k_BZ=(6*pi^2/V_p)^(1/3); % in atomic unit

omega_high=0.1534; % eV

omega_low=0.063; % eV
```

Appendix B (Continued)

```
str_high=0.1124; % for 0.1534 eV

str_low=0.08104; % for 0.063 eV

E_BZ=h_bar^2*k_BZ^2/2; % eV


E=[0.01:0.01:10];


%m_eff=m/2;

m_eff=zeros(1,1000);

for n=1:1000

if E(n)<E_BZ/2

    m_eff(n)=m/2;

elseif E(n)<E_BZ

    m_eff(n)=E(n)*m/E_BZ;

else

    m_eff(n)=m;

end

end

v=sqrt(2*m_eff.*E)./m_eff;


% For high energy mode

n_omega=1/(exp(h_bar*omega_high/(k_b*T))-1);

% define W_2

W_2_plus=E;
```

Appendix B (Continued)

```
W_2_minus=E;
for n=1:1000
    W_2_plus(n)=min(k_BZ,k_b*(1+sqrt(1-h_bar*omega_high./E(n))));
end
for n=1:1000
   W_2_minus(n)=min(k_BZ,k_b*(1+sqrt(1+h_bar*omega_high./E(n))));
end
% define W_1
W_1_plus=k_b*(1-sqrt(1-h_bar*omega_high./E));
W_1_minus=-k_b*(1-sqrt(1+h_bar*omega_high./E));

scat_rate_em_high=e^2*omega_high./(h_bar*v)*str_high.*((n_omega+1).*log(W_2_plus./
    W_1_plus));
scat_rate_abs_high=e^2*omega_high./(h_bar*v)*str_high.*((n_omega).*log(W_2_minus./
    W_1_minus));

% For low energy mode
n_omega=1/(exp(h_bar*omega_low/(k_b*T))-1);
% define W_2
for n=1:1000
    W_2_plus(n)=min(k_BZ,k_b*(1+sqrt(1-h_bar*omega_low./E(n))));
end
```

Appendix B (Continued)

```
for n=1:1000
    W_2_minus(n)=min(k_BZ,k_b*(1+sqrt(1+h_bar*omega_low./E(n))));
end
% define W_1
W_1_plus=k_b*(1-sqrt(1-h_bar*omega_low./E));
W_1_minus=-k_b*(1-sqrt(1+h_bar*omega_low./E));


scat_rate_em_low=e^2*omega_low./(h_bar*v)*str_low.*((n_omega+1).*log(W_2_plus./
    W_1_plus));
scat_rate_abs_low=e^2*omega_low./(h_bar*v)*str_low.*((n_omega).*log(W_2_minus./
    W_1_minus));


imfp_t_low_em=e.^2*omega_low.^2./v.^2.*str_low.*(n_omega+1).*((1-(1-omega_low./(2.*E))
    /(1-omega_low./(2.*E)).^(1/2))*log(W_2_plus./W_1_plus)+(W_2_plus.^2-W_1_plus.^2)
    ./(4*k_b^2*(1-omega_low./E).^(1/2)));
imfp_t_low_abs=e.^2*omega_low.^2./v.^2.*str_low.*(n_omega+1).*((1-(1+omega_high./(2.*E
    ))/(1+omega_high./(2.*E)).^(1/2))*log(W_2_minus./W_1_minus)+(W_2_minus.^2-
    W_1_minus.^2)./(4*k_b^2*(1-omega_low./E).^(1/2)));
imfp_t_high_em=e.^2*omega_low.^2./v.^2.*str_high.*(n_omega+1).*((1-(1-omega_low./(2.*E
    ))/(1-omega_low./(2.*E)).^(1/2))*log(W_2_plus./W_1_plus)+(W_2_plus.^2-W_1_plus.^2)
    ./(4*k_b^2*(1-omega_high./E).^(1/2)));
```

Appendix B (Continued)

```
imfp_t_high_abs=e.^2*omega_low.^2./v.^2.*str_high.*(n_omega+1).*((1-(1+omega_high
    ./(2.*E))/(1+omega_high./(2.*E)).^(1/2))*log(W_2_minus./W_1_minus)+(W_2_minus.^2-
    W_1_minus.^2)./(4*k_b^2*(1-omega_high./E).^(1/2)));


% Define constants
e=1; % in atominc unit = 1.602176565E-19 C
k_b=8.6173324E-5; % in eV/K = 1.3806488E-23 J/K
h_bar=1; % in atominc unit = 1.054571726E-34 Js
m=1; % in atominc unit = 9.10938291E-31 kg
m_SI=9.10938291E-31;
T=300; % K
molar_mass_silicon=28.0855; % 28.0855 grams per mole
N_A=6.02214129E23; % per mole


% define parameters
V_p=762.3; % atomic unit. = 112.98 angstrom^3
k_BZ=(6*pi^2/V_p)^(1/3); % in atomic unit
N_c=1/V_p; % in atomic unit
E_BZ=h_bar^2*k_BZ^2/2; % eV
C_s=1.79E-3; % in atomic unit
S=3.5; % eV
alpha=h_bar*C_s/(k_b*T);
C=6.256;
```

Appendix B (Continued)

```
M=3*molar_mass_silicon*1E-3/(N_A*m_SI); % mass of 3 silicon atoms in atomin unit


% define E

E=0.01:0.01:10;


q=E./(h_bar*C_s);


% define omega(q)

omega=zeros(1,1000);

for m=1:1000

    if q(m)<k_BZ

        omega(m)=C_s*q(m);

    else

        omega(m)=C_s*k_BZ;

    end

end




% define effective mass

m_eff=zeros(1,1000);

for m=1:1000

    if E(m)<E_BZ/2
```

Appendix B (Continued)

```
        m_eff(m)=m/2;
    elseif E(m)<E_BZ
        m_eff(m)=E(m)*m/E_BZ;
    else
        m_eff(m)=m;
    end
end
v=sqrt(2*m_eff.*E)./m_eff;


% define q_max
% define q+_max
q_plus_max=q;
for m=1:1000
    if q(m) < k_BZ
        q_plus_max(m)=2*k_b-2*m_eff(m)*C_s/h_bar;
    else
        q_plus_max(m)=k_b*(1+sqrt(1-h_bar*C_s*k_BZ/E(m)));
    end
end
q_minus_max=q;
for m=1:1000
    if q(m) < k_BZ
        q_minus_max(m)=2*k_b+2*m_eff(m)*C_s/h_bar;
```

Appendix B (Continued)

```
    else
        q_minus_max(m)=k_b*(1+sqrt(1+h_bar*C_s*k_BZ/E(m)));
    end
end

% define n
n=q;
for m=1:1000
    if q(m) < k_BZ
        n(m)=1/(exp(alpha*q(m))-1);
    else
        n(m)=1/(exp(alpha*k_BZ)-1);
    end
end

% define mass of 3 SiO2, M_p
M_p=q;
for m=1:1000
   M_p(m)=M*(1+C*q(m)^2);
end

% define f(q)
f=1+C*q.^2;
```

Appendix B (Continued)

```
% emission

scat_rate_em=q;

itmfp_to=q;

for m=1:1000

    scat_rate_em(m)=3*abs(S)^2/(4*pi*M_p(m)*N_c*h_bar*v(m))*integral(@(q) q.^3/omega(m
        )*(n(m)+1)*f(m),0,q_plus_max(m),'ArrayValued',true);

    itmfp_to(m)=3*abs(S)^2/(4*pi*M_p(m)*N_c*h_bar*v(m))*(integral(@(q) q.^3/omega(m)*(
        n(m)+1)*f(m)*(1-(1-q^2/(2*k_b^2)-omega(m)/(2*E(m))/sqrt(1-omega(m)/E(m)))),0,
        q_plus_max(m),'ArrayValued',true)+integral(@(q) q.^3/omega(m)*(n(m))*f(m)
        *(1-(1-q^2/(2*k_b^2)+omega(m)/(2*E(m))/sqrt(1+omega(m)/E(m)))),0,q_minus_max(m
        ),'ArrayValued',true));

end


% absorption

scat_rate_abs=q;

for m=1:1000

    scat_rate_abs(m)=3*abs(S)^2/(4*pi*M_p(m)*N_c*h_bar*v(m))*integral(@(q) q.^3/omega(
        m)*n(m)*f(m),0,q_minus_max(m),'ArrayValued',true);

end
```

Appendix C

PERMISSION OF REPRINT OF COPYRIGHTED MATERIALS FROM IEEE

A part of this work was reproduced from copyrighted materials from the following publishers: IEEE and AIP Publishing.

The following information regards the copyrighted materials from IEEE:

The IEEE does not require individuals working on a thesis to obtain a formal reuse license, however, you may print out this statement to be used as a permission grant:

Requirements to be followed when using any portion (e.g., figure, graph, table, or textual material) of an IEEE copyrighted paper in a thesis:

1) In the case of textual material (e.g., using short quotes or referring to the work within these papers) users must give full credit to the original source (author, paper, publication) followed by the IEEE copyright line 2011 IEEE.
2) In the case of illustrations or tabular material, we require that the copyright line [Year of original publication] IEEE appear prominently with each reprinted figure and/or table.
3) If a substantial portion of the original paper is to be used, and if you are not the senior author, also obtain the senior authors approval.

Appendix C (Continued)

Requirements to be followed when using an entire IEEE copyrighted paper in a thesis:

1) The following IEEE copyright/ credit notice should be placed prominently in the references: [year of original publication] IEEE. Reprinted, with permission, from [author names, paper title, IEEE publication title, and month/year of publication]
2) Only the accepted version of an IEEE copyrighted paper can be used when posting the paper or your thesis on-line.
3) In placing the thesis on the author's university website, please display the following message in a prominent place on the website: In reference to IEEE copyrighted material which is used with permission in this thesis, the IEEE does not endorse any of [university/educational entity's name goes here]'s products or services. Internal or personal use of this material is permitted. If interested in reprinting/republishing IEEE copyrighted material for advertising or promotional purposes or for creating new collective works for resale or redistribution, please go to http://www.ieee.org/publications_standards/publications/rights/rights_link.html to learn how to obtain a License from RightsLink.

If applicable, University Microfilms and/or ProQuest Library, or the Archives of Canada may supply single copies of the dissertation.

Appendix D

PERMISSION OF REPRINT OF COPYRIGHTED MATERIALS FROM AIP PUBLISHINGS

The permission to reproduce copyrighted materials from AIP publishing is granted with the following letter of permission: Material to be reproduced:

J. Appl. Phys. 118, 194304 (2015);

For use in the following manner:

Reproduced in your dissertation.

Permission is granted subject to these conditions:

1. AIP Publishing grants you non-exclusive world rights in all languages and media. This permission extends to all subsequent and future editions of the new work.

2. The following copyright notice must appear with the material (please fill in the information indicated by capital letters):

"Reproduced with permission from [FULL CITATION]. Copyright [PUBLICATION YEAR], AIP Publishing LLC.

When reusing a full article, the copyright notice must be printed on the first page of the reprinted article or book chapter. When reusing figures, photographs, covers, or tables, the notice may appear in the caption, in a footnote, or in the reference list.

In cases where the new publication is licensed under a Creative Commons license, the full copyright notice as stated above must appear with the reproduced material.

Appendix D (Continued)

3. If the material is published in electronic format, we ask that a link be created pointing back to the abstract of the article on the journal website. This can be accomplished through the use of the articles DOI. 4. This permission does not apply to any materials credited to another source.

VITA

NAME: Min Seok Choi

EDUCATION: B.A., Engineering Physics, University of Colorado at Boulder, Boulder, Colorado, 2010

B.A., Business Administration, University of Colorado at Boulder, Boulder, Colorado, 2010

Ph. D., Electrical and Computer Engineering, University of Illinois at Chicago, Chicago, Illinois, 2016

HONORS: Graduate Student Council Travel Award, University of Illinois at Chicago, 2015.

Student Presenter Awards, University of Illinois at Chicago, 2015.

University of Colorado at Boulder Grant Scholarship, University of Colorado at Boulder, 2008 - 2010.

PUBLICATIONS: Min Choi*, Xenia Meshik*, Souvik Mukherjee, Sidra Farid, Sam Doan, Leigha Covnot, Mitra Dutta, and Michael A. Stroscio, Optical, structural, and electrostatic properties of zinc oxide quantum dot, Journal of Applied Physics, Volume 118, 20, 2015.

S. Farid, Min Choi, D. Datta, M. A. Stroscio, and M. Dutta, Spontaneous Polarization Induced Electric Field in Zinc Oxide Nanowires and Nanostars, accepted, 2016.

Souvik Mukherjee, Xenia Meshik, Min Choi, Sidra Farid, Debopam Datta, Yi Lan, Shripriya Poduri, Ketaki Sarkar, Undarmaa Baterdene, Ching-En Huang, Yung Yu Wang, Peter Burke Mitra Dutta, and Michael A. Stroscio, A graphene and aptamer based liquid gated FET-like electrochemical biosensor to detect adenosine triphosphate, IEEE Trans. on Nanobioscience, in press, 2015.

VITA (Continued)

PUBLICATIONS:

Xenia Meshik, Sidra Farid, Min Choi, Yi Lan, Souvik Mukherjee, Debopam Datta, Mitra Dutta, and Michael A. Stroscio, Biomedical Applications of Quantum Dots, Nucleic-acid-based Aptamers, and Nanostructures for Biosensors, Critical Reviews in Biomedical Engineering, 2015.

Sidra Farid, Xenia Meshik, Min Choi, Yi Lan, Souvik Mukherjee, Devanshi Parikh, Shripriya Poduri, Undarmaa Baterdene, Ching-En Huang, Yung Yu Wang, Peter Burke, Mitra Dutta, and Michael A Stroscio, Detection of Interferon Gamma using graphene and aptamer based FET-like electrochemical biosensor, Biosensors and Bioelectronics, Vol. 71, 294299, 2015.